Controlling and probing molecular motion with optical lattices

Alexandros Gerakis

A thesis submitted to University College London
in partial fulfilment of the requirements for the
degree of Doctor of Philosophy

Department of Physics and Astronomy
University College London
March 2014

I, Alexandros Gerakis, confirm that the work presented in this thesis is my own. Where information has been derived from other sources, I confirm that this has been indicated in the thesis.

Signed ..... Date .....

Abstract

This thesis describes the further improvement of an already developed by our group laser system capable of delivering high energy, frequency agile, flat-top pulses and its uses in non-resonant molecular scattering diagnostics in the form of coherent Rayleigh-Brillouin scattering, as well as for optical Stark deceleration of neutral H_2 molecules. This laser system is capable of delivering two computer controlled flat-top pulses of variable duration $(20 - 1000$ ns) with energies up to 700 mJ per pulse and with linearly chirped frequencies up to 1.5 GHz.

With the use of constant velocity lattices driven by this system we were able to accurately obtain coherent Brillouin scattering spectra of purified air in the hydrodynamic regime where, for the first time, we observed additional spectral peaks to the main Brillouin peak, as well as up to 40% reduction of the peak due to the interaction of the laser driven electrostrictive grating with the acoustic which was launched in the gas due to its thermalisation by the optical field.

Furthermore, by utilising chirped frequency optical lattices, we were able to obtain accurate coherent Rayleigh-Brillouin spectra with signal-to-noise ratios in excess of 100, in a single laser shot ($\sim$140ns) thus reducing the acquisition times needed for such spectra by ten orders of magnitude, rendering the technique ideal for combustion and transient flow diagnostics.

Finally, we report on the use of this laser system as a tool for optical Stark deceleration of neutral H_2 molecules, where through a Raman tagging scheme of the interacting molecules we are proposing an efficient way to monitor the interactions occurring within the decelerating optical lattice. We hope that this technique will pave the way for the production of narrow velocity spread molecular ensembles to be used in cold collisional studies as well as sympathetic cooling.

Contents

To Lena & Pavlos

Acknowledgments

I would like to initially thank my supervisor Professor Peter Barker for a very fruitful and enoyable collaboration during the course of my PhD. His guidance, support and physical insight during experiments have had a significant and positive effect on my studies. I would like to thank Dr. Mikhail Shneider for our collaboration in the CRBS experiments as well as Dr Jonathan Underwood for the very useful discussions relating to the OSD experiment. I would like also to thank them both for their overall support. I owe a massive thank you Dr Nicholas Coppendale, Dr Peter Douglas and Dr Conor Maher-McWilliams which were already members of our group when I first started my PhD, and made me feel UCL like home. A special thanks should go to Dr Nicholas Coppendale whose experiment I took over and without him showing me how it works, I would still be looking for the mains plug :P. Massive gratitude is owed to current members of our group as well, for their patience while using shared equipment and especially for tolerating me during my most stressful days! Pete Edmunds, Ilhan Candan, Lia Han, Manish Trivedi...thank you! And most of all a special thank you to Dr. James Millen who has had the patience to proofread this thesis! Finally, a special mention must also go to Dr Arne Wickenbrock who has always kept things at UCL interesting.

Outside of UCL I want to thank all of my friends here in London, as well as back home, for their constant support thoughout my studies. You're way to many to name all of you here but...you know who you are ;). I wouldn't have got here without out you! Last, and most certainly not least, a HUGE thank you must go to my parents, who have always been there for me, no matter where I was in the world. I hope I'll be able to repay you somehow someday although your love and support all these years has been really invaluable!

Ας υποθέσουμε πως δεν έχουμε φτάσει
στο μαύρο αδιέξοδο, στην άβυσσο του νου.
Ας υποθέσουμε πως ήρθανε τα δάση
μ'αυτοκρατορική εξάρτηση πρωινού
θριάμβου, με πουλιά, με το φως τ'ουρανού,
και με τον ήλιο όπου θα τα διαπεράσει.

Ας υποθέσουμε πως είμαστε κει πέρα,
σε χώρες άγνωστες, της δύσης, του βορρά,
ενώ πετούμε το παλτό μας στον αέρα,
οι ξένοι βλέπουνε περίεργα, σοβαρά.
Για να μας δεχθεί κάποια λαίδη τρυφερά,
έδιωξε τους υπηρέτες της ολημέρα.

Ας υποθέσουμε πως του καπέλου ο γύρος,
άξαφνα εφάρδυνε, μα εστένεψαν, κολλούν,
τα παντελόνια μας και, με του πτερνιστήρος
το πρόσταγμα, χιλιάδες άλογα κινούν.
Πηγαίνουμε - σημαίες στον άνεμο χτυπουν -
ήρωες σταυροφόροι, σωτήρες του Σωτήρος.

Ας υποθέσουμε πως δεν έχουμε φτάσει
από εκατό δρόμους, στα όρια της σιγής,
κι ας τραγουδήσουμε, - το τραγούδι να μοιάσει
νικητήριο σάλπισμα, ξέσπασμα κραυγής -
τους πυρρούς δαίμονες, στα έγκατα της γης,
και, ψηλά, τους ανθρώπους να διασκεδάσει.

Κ. Καρυωτάκης, "*Αισιοδοξία*"
K. Karyotakis, "Optimism"

Publications

1. A. Gerakis, M. N. Shneider and P. F. Barker, *Coherent Brillouin scattering*, Optics Express **19**, 24, (2011)

2. A. Gerakis, M. N. Shneider and P. F. Barker, *Single−shot coherent Rayleigh−Brillouin scattering using a chirped optical lattice*, Optics Letters **38**, 21 (2013)

Chapter 1

Introduction

Light has been perhaps the most useful probe for the study of inherent atomic and molecular properties, as well as a useful tool to control the motion of these particles. For the work presented in this thesis, intense light fields produced by a laser system developed in our experimental group are used for gas diagnostics through scattering as well as for controlling the translational motion of molecules through the optical dipole force. It is possible to achieve these through the interaction of the particles with the light field, which induces a dipole moment on the particles and the further interaction of the induced dipole moment with the field that created it.

In this chapter, after a short historical review of light-matter interactions, I will present the physics of the interaction between the light field and the particle, termed the *polarisability*, and show how we exploit two manifestations of polarisability in scattering and molecular motion control. Finally, I will present the motivation for the work carried out for this thesis and provide an outline of it.

1.1 Light-matter interaction: A short historical review

Light and its interaction with matter can be traced back to the ancient Greeks as early as 424 BC, with the first mention of positive lenses in Aristophanes' play *The Clouds* [1]. It was around that time that Leucippus along with his student Democritus were developing in Miletus the theory of *atomism*[1] "in which the universe is composed of immutable, indestructible atoms, and the space through which they move, the *void*" [2]. In the atomists' view of the world, natural phenomena were attributed "to the motion of atoms and the

[1]The word *atom* in Greek is derived from *a*+*tomi*(=section), meaning something that can't be further fragmented

diversity of material objects to their shapes and interlocking structures".

During the same period, Empedocles in the Greek city of Akragas in Sicily proposed his famous theory of the four classical elements[2] as well as the first known theory of light. According to Empedocles, light particles flow as a stream from the eyes and shine on material objects. Some $100 - 150$ years after Empedocles, Euclid took this flux idea and assumed that it followed straight lines in order to explain reflection in his book of *Optics*, which is the first mathematical treatise on optics. Based on Euclid's work, Claudius Ptolemy, a Greco-Roman philosopher and mathematician of Alexandria, treated reflection, refraction[3] and colour in his own *Optics*, which was the main book on optics[4] in Europe for the next millennium. In the time between Ptolemy and the European Renaissance, the only influential treatise on optics was by Alhazen[5], an Arab scientist in Cairo, who by experimenting with mirrors and magnifying lenses laid the foundation for catoptrics and also studied luminance, the rainbow and atmospheric refraction, among other topics. Alhazen is also attributed with the discovery of the *camera obscura*, the forefather of the imaging camera.

Copernicus with his heliocentric view of the world in 1543, ignited what we now refer to as the European Renaissance[6], where the original ideas and thoughts posed by the ancient Greeks were revisited and questioned after a gap of nearly fifteen centuries. Copernicus's claim was experimentally proven by Galileo Galilei in 1610[7], when he observed the moons of Jupiter to be orbiting around Jupiter and not the Earth. The biggest breakthrough though in the view of the world came from René Descartes[8] who, by refusing the authority of previous philosophers as well as refusing to accept the obviousness of his own senses, overcame Empedocles' four element system by suggesting that the universe consisted only of matter and motion[9]. In Descartes' universe, forces from a distance were not existent as these could only act by actual contact between the interacting bodies, while he filled the Leucippus-Democritus *void* "with a kind of very-fine-grained material medium or plenum"[2]. It is due to this idea that the *aether* was introduced in the physical thought[10].

[2]Fire, air, water and earth which interacted through two forces, a repulsive and an attractive one, called *strife* and *love*, respectively

[3]Containing the earliest surviving table of refraction from air to water

[4]Along with his geocentric astronomy in the *Almagest*

[5]1021, *Book of Optics*

[6]From the French word for rebirth

[7]Only two years after the invention of the telescope in the Netherlands by Hans Lippershey and Zacharias Janssen, who were spectacle makers in Middelburg, and Jacob Metius of Alkmaar.

[8]Or Renatus Cartesius as he liked to sign his manuscripts

[9]1644, *Principia philosophiae*

[10]The word *aether* stands for fresh, pure air in ancient Greek and was proposed to be added as a fifth

Although Descartes defied Empedocles' view of the world, he kept his view of light as a flux of particles and used it to explain light emission, reflection, refraction and absorption.

Descartes' work on refraction was strongly opposed by Pierre de Fermat who introduced his famous *principle of least time* in 1662 to explain refraction. They both independently found what we now call "Snell's law"[11], but Fermat's solution assumed a finite speed for the light (contrary to Descartes' belief of its infinite speed) and, more importantly, Fermat's solution required a smaller speed for the light within the denser medium as opposed to a higher speed that Descartes' flux of light particles required within the dense medium. It was this idea of Fermat that paved the way for light to be considered different than matter. Robert Hooke in 1672 was the first to introduce a wave theory of light in order to explain diffraction and refraction. More importantly, Hooke attributed the production of light to be due to the rapid vibratory motion of the particles constituting ordinary matter, and that it propagated at right angles to these vibrating centres. Hooke also tried to explain colour through refraction, only to be corrected by Isaac Newton in 1666 who, with a use of a prism, proved that colour is an intrinsic property of light.

Nevertheless, Hooke's work on a wave theory of light led Christiaan Huygens to express in 1690 in his book *Traité de la lumière*[12] the principle now bearing his name and according to which *every point on a wave-front may be considered a source of secondary spherical wavelets which spread out in the forward direction at the speed of light. The new wave-front is the tangential surface to all of these secondary wavelets.* Based on this principle, Augustin-Jean Fresnel established modern wave optics over a century later, encouraged by Thomas Young's double slit experiment in 1803 which experimentally confirmed the wave theory of light. Fresnel also showed in 1821 that the polarisation of light[13] was consistent with the wave theory if the periodic vibration is transverse to the direction of light propagation.

Descartes' axiom that forces could not act from a distance was already overruled by Newton's work on gravity. In electromagnetism this was overruled by the work of Michael Faraday (1791-1867) who "pictured magnetic influences acting on bodies not in direct contact as *lines of force.* These lines, originating and terminating in closed loops, were the beginnings of force *fields* acting on bodies through space with no actual physical constant"[2].

element in Empedocles' four element system in Plato's *Timaeus*

[11]Discovered in 1621 by Willebrord Snellius but never published during his lifetime

[12]Treatise on light

[13]Initially discovered by Newton in 1704 based on the *ordinary* and the *extra-ordinary* light propagation Huygens had observed in Iceland Spar crystals

The over two millennia quest to determine the nature of light seemed to come to an end with James Clerk Maxwell's classic publication in 1865 of *A Dynamical Theory of the Electromagnetic Field* in which he proposed that light was in fact a transverse electromagnetic wave. Nowadays, the four Maxwell equations and the force law proposed by Hendrik Lorentz form a unified classical theory of electricity, magnetism and light. Nowadays, through quantum theory, we also know of the wave-particle duality nature of light.

Originally the studies of the properties of the basic constituents of matter were performed with static electric fields, such as the ones produced between the plates of a capacitor, or alternating (AC) electric fields. As soon though as it was realised that light itself constituted a high quality AC electric field of well-defined polarisation, energy and wavelength, it immediately replaced those conventional sources as a probe of the energy dependent atomic and molecular properties. This was immediately perceived by Joseph von Fraunhofer who, in 1814, invented the spectroscope where he used a diffraction grating rather than a prism as a dispersive element. By turning his spectroscope towards the Sun's light he observed dark bands in the Sun's spectrum which now bear his name as the Fraunhofer lines. Essentially then, scientists didn't have but to look for the absorption or emission spectra from various sources to determine the source's properties[14], while the discovery of the laser by Maiman [3, 4] in 1960 provided a coherent, high intensity, well defined light source. In all cases though, electric fields are used as a means to access perhaps the most important property of an atomic/molecular system, which is the *polarisability*.

1.2 Polarisability

Following IUPAC's[15] definition in the molecular case, the polarisability is defined as "the ease of distortion of the electron cloud of a molecular entity by an electric field [...]It is experimentally measured as the ratio of induced dipole moment $\boldsymbol{p}_{\text{ind}}$ to the field $\boldsymbol{E}$ which induces it"[5]

$$\alpha = \frac{\boldsymbol{p}_{\text{ind}}}{\boldsymbol{E}}. \tag{1.1}$$

This constant of proportionality α between the induced dipole moment and the field that caused it, is called polarisability. This definition is of course easily expandable to every particle with a charge distribution within it. Physically, "the polarisability is the *funda-*

[14] Jean Bernard Léon Foucault had already experimentally proved in 1849 that absorption and emission lines appearing at the same wavelength are both due to the same material

[15] International Union of Pure and Applied Chemistry

mental property that characterises the particle-field interaction. As such, the polarisability is measurable from an energy shift or a momentum shift in the particles *or* as a change in the energy of momentum of the field (as in the scattering and absorption of light)" [6]. The polarisability is a very important quantity in physics and chemistry since it determines the response of neutral particles to applied fields, as well as it determines the particles' behaviour in the interactions between them. It also gives useful insight of the physical size, structure, shape and electronic structure of the particle examined [6]. Finally, important physical properties of materials such as their dielectric constant and their refractive index are directly related to their polarisability.

The first mention of an effect that could be attributed to molecular polarisability was that of anomalous dispersion[16] by Fox Talbot in 1840. Sir George Stokes in 1852, in his paper on the change of wavelength of light where he was trying to describe fluorescence[17], proposed that molecules could be considered to have their own natural vibrational frequencies that result in observable effects when interacting with light of different frequency. August Kundt in 1871 first made the general observation that anomalous dispersion occurred whenever an absorption band was present in the spectrum. A theoretical treatment of the matter was presented by Maxwell in 1869 and Sellmeier in 1872 which supposed the existence of harmonic oscillators in the material that would be driven when the frequency of light approached their natural frequency. This was expressed in the famous Sellmeier formula, where the refractive index n of a material is expressed as a function of wavelength λ [6]

$$n^2 - 1 = \frac{e^2}{\pi m c^2} \sum_k N f_\mathrm{k} \lambda_\mathrm{k}^2 [1 + \frac{\lambda_\mathrm{k}^2}{\lambda^2 - \lambda_\mathrm{k}^2}], \tag{1.2}$$

where Nf_k is the number of electrons having a resonance at wavelength λ_k, c is the speed of light, e is the charge of an electron and m is the mass of the electron. A microscopic view of the response of atoms/molecules to electric fields first came from Woldemar Voigt in 1901 who predicted that an analogy to the Zeeman line splitting should exist in the case of electric fields. Experimental proof of this theoretical prediction came after 12 years when Antonino Lo Surdo in Italy and Johannes Stark in Germany, independently reported the observation of such line splittings caused by electric fields.

The polarisability shown in Eq. 1.1 assumes a relatively low field $\boldsymbol{E}$ and an isotropic response from the particle regardless of the direction of the field, hence it is represented

[16] In anomalous dispersion the refractive index of a material increases with increasing wavelength
[17] A term coined by Stokes

by a scalar quantity. That is a valid approximation for particles of spherical symmetry in homogeneous fields. However, this approximation does not hold in the case of non-symmetrical particles, such as even simple diatomic molecules like H_2, N_2 or O_2. Indeed in these cases, the charge distribution across the internuclear axis is much larger than that perpendicular to this axis. Is is apparent then that a more general form is needed to describe the polarisability response of the particle with respect to the direction of the field. Thus, the polarisability of Eq. 1.1 needs to be expressed as a tensor $\boldsymbol{a}$ so that Eq. 1.1 becomes

$$\boldsymbol{p}_{\text{ind}} = \boldsymbol{\alpha}\boldsymbol{E}, \tag{1.3}$$

which in matrix notation can be written as

$$\begin{pmatrix} p_{\text{x}} \\ p_{\text{y}} \\ p_{\text{z}} \end{pmatrix} = \begin{pmatrix} \alpha_{\text{xx}} & \alpha_{\text{xy}} & \alpha_{\text{xz}} \\ \alpha_{\text{yx}} & \alpha_{\text{yy}} & \alpha_{\text{yz}} \\ \alpha_{\text{zx}} & a_{\text{zy}} & \alpha_{\text{zz}} \end{pmatrix} \begin{pmatrix} E_{\text{x}} \\ E_{\text{y}} \\ E_{\text{z}} \end{pmatrix} \tag{1.4}$$

The polarisability expression shown in Eq. 1.3 is valid for molecules of all symmetries, but only holds for static electric fields. In time-varying electric fields (such as the ones in a light beam), the electronic response of the interacting particles is more complex. Hence, a more sophisticated description for their polarisability is needed. This should take into consideration the fact that the polarisability depends on the frequency of the light inducing the dipole moment, and also the fact that the interacting particle can absorb and emit photons; hence the polarisability tensor should consist of a *dispersive* and an *absorptive* part. The former would account for the absorption and instantaneous reemission of photons, thus it would correspond to light scattering, while the latter would account for light absorption by the particle with subsequent deexcitation. The result for the $\boldsymbol{\alpha}(\omega)$ tensor is thus in the form

$$\boldsymbol{\alpha}(\omega) = \boldsymbol{\alpha}'(\omega) + i\boldsymbol{\alpha}''(\omega), \tag{1.5}$$

where the real part $\boldsymbol{\alpha}'(\omega)$ is the dispersive part of the tensor whereas the imaginary $\boldsymbol{\alpha}''(\omega)$ part is the absorptive part of the tensor. These can be found analytically through the well-known Kramers-Kronig relations, which will not be derived here, but refer to [6] for an advanced treatment and subsequent physical analysis on them.

During the work carried out for the purposes of this thesis, frequency agile optical lat-

tices have been used in order to exploit the manifestation of molecular polarisability in the form of Rayleigh-Brillouin scattering as well as for coherently controlling the translational motion of H_2 molecules in these lattices due to the optical dipole force.

1.2.1 Manifestations of polarisability: light scattering

The polarisability as defined in Eq. 1.5 refers to the fundamental, electronic property of a *single* molecule to become polarisable in the presence of an electric field. The macroscopic equivalent of polarisability is the electric susceptibility χ. Equivalently to Eq. 1.3 we define the linear polarisation $\boldsymbol{P}(\boldsymbol{r},t)$ as the net dipole moment per unit volume of material due to the applied electric field $\boldsymbol{E}(\boldsymbol{r},t)$ through the electric susceptibility χ as

$$\boldsymbol{P}(\boldsymbol{r},t) = \epsilon_0 \chi \boldsymbol{E}(\boldsymbol{r},t), \tag{1.6}$$

where ϵ_0 is the vacuum electric permittivity. If we assume an electric field of amplitude E, frequency ω and wavevector $\boldsymbol{k}$ in the form

$$\boldsymbol{E}(\boldsymbol{r},t) = E[e^{i(\boldsymbol{k}\boldsymbol{r}-\omega t)} + \text{c.c.}], \tag{1.7}$$

to be propagating through a collection of particles, then the wave equation for the interaction between the electric field and the medium is given by

$$\nabla^2 \boldsymbol{E}(\boldsymbol{r},t) - \frac{1}{c^2}\frac{\partial^2}{\partial t^2}\boldsymbol{E}(\boldsymbol{r},t) = \frac{4\pi}{c^2}\frac{\partial^2}{\partial t^2}\boldsymbol{P}(\boldsymbol{r},t). \tag{1.8}$$

where c is the speed of light in vacuum. Substituting Eqs. 1.6 and 1.7 in Eq. 1.8 yields

$$\boldsymbol{k}^2 - \frac{\omega^2}{c^2} = \frac{4\pi\epsilon_0\omega^2}{c^2}\chi(\omega) \Leftrightarrow \frac{\boldsymbol{k}^2 c^2}{\omega^2} = 1 + 4\pi\epsilon_0\chi(\omega). \tag{1.9}$$

The frequency dependent electric susceptibility $\chi(\omega)$ is normally, as $\boldsymbol{\alpha}(\omega)$, a tensor. For simplicity, here we assume an isotropic response of the medium, hence the tensor simplifies to a scalar. Also, since $\chi(\omega)$ is the macroscopic analogue to the polarisability $\alpha(\omega)$, it has got to have a real and an imaginary part. Equivalently to Eq. 1.5, we can then write for χ

$$\chi(\omega) = \chi'(\omega) + \chi''(\omega). \tag{1.10}$$

If we define

$$\frac{\boldsymbol{k}c}{\omega} = n + i\kappa, \tag{1.11}$$

where n is the refractive index of the medium and κ is the extinction coefficient, then by substituting Eqs. 1.10 and 1.11 into Eq. 1.9, we obtain

$$1 + \chi'(\omega) = n^2 - \kappa^2, \tag{1.12a}$$

$$\chi''(\omega) = 2n\kappa. \tag{1.12b}$$

Equation 1.11 clearly shows how the electric field defined in Eq. 1.7 has its phase modified due to the interaction with the medium. Indeed, through Eq. 1.11 we can rewrite the phase of the electric field as

$$i(\boldsymbol{k}\boldsymbol{r} - \omega t) = i\left[\frac{\omega}{c}(n + i\kappa)\boldsymbol{r} - \omega t\right] = i\omega(n\frac{\boldsymbol{r}}{c} - t) - \frac{\omega}{c}\kappa\boldsymbol{r}. \tag{1.13}$$

Introducing the refractive index n in the space dependent part of the electric field phase clearly shows its modification due to the propagation through a medium of refractive index n. Simultaneously, the electric field amplitude is modified by a factor $e^{\omega\kappa\boldsymbol{r}/c}$, which suggests that its intensity can increase or decrease with increasing propagation distance, depending on the sign of κ. This result is summarised in the Beer-Lambert law which gives the intensity of a beam at a position z

$$I(z) = I(0)e^{-Kz}, \tag{1.14}$$

where $I(0)$ is the initial intensity of the beam and K is the attenuation coefficient defined as

$$K = \frac{2\omega\kappa}{c}. \tag{1.15}$$

From Eq. 1.12a it follows that if there is no absorption then $n^2 = \chi'(\omega) + 1$. Thus, the real part of the susceptibility (and hence the polarisability) is associated with the refractive index of the medium, while the imaginary part is associated with the absorption from the medium. Through Eq. 1.13 it follows that the scattering of light by particles, which is associated with the refractive index n, occurs in the forward direction to the light field propagation while in absorption light is ultimately scattered in all directions. If the frequency of the light field is chosen to match a resonant frequency of the particle then

absorption is maximum, $n = 1$ and ultimately $\chi'(\omega) = 0$. Also, since the refractive index n of a medium is related to its electric permittivity ϵ through the relation $n = \sqrt{\epsilon}$, it follows that the electric permittivity of a medium would also be related to its susceptibility

$$\epsilon = \chi'(\omega) + 1. \tag{1.16}$$

For completeness, we mention that for high values of the electric field, the linear polarisation of the medium as shown in Eq. 1.6 breaks down and instead the molecular response to the field is represented via a power series of the form

$$\boldsymbol{P}(\boldsymbol{r}, t) = \epsilon_0(\chi^{(1)}\boldsymbol{E}(\boldsymbol{r}, t) + \chi^{(2)}\boldsymbol{E}^2(\boldsymbol{r}, t) + \chi^{(3)}\boldsymbol{E}^3(\boldsymbol{r}, t) + ...), \tag{1.17}$$

where the $\chi^{(i)}$ are the i-th order susceptibilities of the medium and are being exploited in applications such as scattering ($\chi^{(1)}$), second harmonic generation ($\chi^{(2)}$), the optical Kerr effect ($\chi^{(3)}$) etc. In the work presented in this thesis, we exploit the $\chi^{(3)}$ susceptibility in order to study Rayleigh scattering and its Doppler shifted manifestation which is Brillouin scattering, in the form of coherent Rayleigh-Brillouin scattering.

1.2.2 Manifestations of polarisability: the optical dipole force

The analysis performed in Section 1.2.1 considered the effects of light-matter interaction through polarisability, on the incident light field. This interaction has an effect on the interacting particle as well, which manifests itself as the *optical dipole force*.

For the simple case of a particle in an inhomogeneous static field, as in Eq. 1.3, the potential seen by the particle with only an induced dipole is of the form

$$U = -\frac{1}{2}\epsilon_0 \boldsymbol{p}\boldsymbol{E} = -\frac{1}{2}\epsilon_0 \boldsymbol{a}\boldsymbol{E}^2, \tag{1.18}$$

while the force experienced by this particle is

$$\boldsymbol{F} = -\nabla U = \frac{1}{2}\epsilon_0 \boldsymbol{a}\nabla \boldsymbol{E}^2. \tag{1.19}$$

For the case when the particle interacts with a harmonic field, of amplitude $\boldsymbol{E}_0$ and frequency ω, of the form

$$\boldsymbol{E}(\boldsymbol{x}, t) = \boldsymbol{E}_0(\boldsymbol{x})e^{-i\omega t} + \text{c.c.}, \tag{1.20}$$

the particle will acquire a steady-state, oscillating dipole moment $\boldsymbol{p}$ that will also oscillate at frequency ω

$$\boldsymbol{p}(\boldsymbol{x},t) = \boldsymbol{p}_0(\boldsymbol{x})e^{-i\omega t} + \text{c.c.}, \tag{1.21}$$

where $\boldsymbol{p}_0 = \boldsymbol{\alpha}\boldsymbol{E}_0(\boldsymbol{x})$. If we follow the expression for α as given in Eq. 1.5 and consider the work W done on the particle by the field

$$W(\boldsymbol{x},t) = \boldsymbol{E}(\boldsymbol{x},t)\frac{\partial \boldsymbol{p}(\boldsymbol{x},t)}{\partial t}, \tag{1.22}$$

then the time averaged work done on the particle due to its induced dipole force will be [6]

$$\langle W \rangle = \frac{\omega}{2}\boldsymbol{E}_0^*\boldsymbol{\alpha}''\boldsymbol{E}_0. \tag{1.23}$$

Thus whilst in this harmonic field the particle dissipates energy. As was the case with the scattering mechanism discussed in Section 1.2.1 this dissipation due to photon absorption is associated with the imaginary part of the polarisability. The particle in this harmonic field experiences a time averaged force $\langle \boldsymbol{F} \rangle$ which will be the sum of a dissipative and a conservative force [6]

$$\langle \boldsymbol{F} \rangle = \langle \boldsymbol{F}_\text{c} \rangle + \langle \boldsymbol{F}_\text{d} \rangle . \tag{1.24}$$

The conservative force $\langle \boldsymbol{F}_\text{c} \rangle$ is known as the *dipole force*[18] and is the negative gradient of a time averaged potential $\langle U \rangle$ similar to the one shown in Eq. 1.18. The dipole force is thus given by

$$\langle \boldsymbol{F}_\text{c} \rangle = -\nabla \langle U \rangle = -\nabla \left(-\frac{1}{4}\boldsymbol{E}_0^*\alpha'\boldsymbol{E}_0 \right), \tag{1.25}$$

while the dissipative force[19] will be given by [6]

$$\langle \boldsymbol{F}_\text{d} \rangle = \frac{1}{4i}E_{0,k}^*\alpha_{kl}''\nabla E_{0,l} + \text{c.c.}, \tag{1.26}$$

where repeated indices are summed over. From the expressions for the dipole force and the dissipative force (Eqs. 1.25 and 1.26, respectively) and their respective relation to the real and imaginary parts of the polarisability, we can draw similar conclusions to the ones reached while discussing susceptibility in Section 1.2.1. When close to, or at, resonance the polarisability of the particle is dominated by the imaginary part and the dissipative force

[18] Also known as *electrostrictive* or *ponderomotive* force
[19] Also known as the *scattering* or *spontaneous* force

dominates, while when operating far from resonance then $\alpha' >> \alpha''$ and the dipole force dominates. The dissipative force is exploited in the optical cooling and trapping of atoms [7, 8, 9] while the optical dipole force finds many applications in optical tweezers [10] and many optomechanical systems. Due to their lack of closed cycling transitions, molecules cannot be trapped and cooled by means of the dissipative force, hence various schemes have been proposed over the years to provide an alternative which would allow for efficient molecular cooling and trapping. Our experimental group has proposed a method termed *optical Stark deceleration*, which exploits the optical dipole force to provide cold molecules in the range of $100 - 200$ mK. These molecules could then be further cooled via collisions with ultra-cold atoms, via a sympathetic cooling scheme.

Optical Stark deceleration

Optical Stark deceleration is a technique developed in our research group where by the use of intense, pulsed optical fields molecules are decelerated from a supersonic jet. In this scheme, dipole moments are induced in the interacting molecules by far red detuned optical fields; hence the dominant physical mechanism is the optical dipole force, as discussed in Section 1.2.2 [11, 12]. The interacting optical fields are formed by two nearly counter-propagating laser pulses with intensities exceeding 10^{11} Wcm^{-2}, which create an interference pattern to maximise the force on the interacting molecules (as a result of Eq. 1.25). This interference pattern creates a deep periodic optical lattice potential for molecules, moving at a velocity dependent on the frequency difference between the two interfering laser beams. Molecular deceleration with constant velocity lattices has been experimentally demonstrated [11] while one of the experiments described in this thesis is aiming at the experimental demonstration of the scheme with decelerating optical lattices.

The major advantage of this technique is its applicability to (in theory) decelerate any molecule, since it relies on the induced dipole moment and does not require the existence of a permanent electric or magnetic dipole moment, as is the case in Stark and Zeeman deceleration.

Sympathetic cooling of molecules with ultra-cold atoms

Sympathetic cooling is another technique aiming to produce molecules at temperatures below 1 mK. In this technique, cold molecules are co-trapped with ultra-cold atoms and

through subsequent thermalisation of the species via collisions a lower final temperature for the molecules is achieved. The underlying physics of this technique is no different to that exhibited in buffer gas cooling. Sympathetic cooling was originally demonstrated between the different spin substates of Rb atoms trapped in a magnetic trap [13] while it has also been demonstrated in the interaction between fermionic ^{6}Li atoms with bosonic ^{7}Li atoms [14]. The first interspecies demonstration of the technique was in a magnetic trap containing evaporatively cooled Rb which thermalized with co-trapped K atoms to produce the first K Bose-Einstein condensate (BEC) [15].

In order to achieve sympathetic cooling of H_2 molecules with rare gas atoms, a sympathetic cooling technique has been proposed by our experimental group [16, 17, 18]. This scheme relies on co-trapping H_2 molecules initially decelerated via optical Stark deceleration in an optical trap along with ultra-cold ground state argon atoms, quenched to their ground state from an Ar* magneto-optical trap (MOT). H_2 was chosen mainly due to its role as a prototypical molecule as well as because of the great interest to the astronomy and chemistry communities. Rare gases such as argon are preferable since they are unreactive in their ground state and hence provide a favourable ratio of elastic to inelastic collisions. Optical traps are more attractive than magnetic and electrostatic traps since they are not quantum state specific and can also trap species which could not be trapped in another way, thus improving the generality of the scheme. Also, trap losses due to state changing collisions are minimised in an optical trap.

Theoretical calculations were performed on the elastic scattering cross sections between H_2 and the rare gas species that can be laser cooled (helium, neon, argon, krypton and xenon) [16, 18]. The largest elastic scattering cross-sections were found for the He-H_2 and Ar-H_2 ensembles. Preparing ultra-cold rare gas atoms in their ground state is a two-step process as rare gas atoms cannot be laser cooled in this state. They first need to be laser cooled in their excited state, and subsequently quenched to their ground state, before being loaded in the optical trap. Argon was thus preferred to He due to the recoil effect in the latter which heats it by over 1 mK and renders it unsuitable for this experiment. Through these simulations, final temperatures of 330 ± 30 μK were predicted for H_2, which would be observable within 10 seconds after the two species are loaded in the trap.

This sympathetic cooling scheme is currently being developed in our research group, and comprises of three distinct elements. (1) The development of a source of ultra-cold

ground state argon atoms, (2) the production of stationary H_2 molecules through chirped optical Stark deceleration and (3) the construction of a high finesse cavity to co-trap the two species. Part of the work presented in this thesis focuses on the experimental implementation of the production of stationary H_2 molecules through chirped optical Stark deceleration.

Since a source of cold and ultra-cold molecules is of great scientific interest, many schemes have been proposed to achieve this goal. In the following sections I present an overview of these schemes.

Association of ultracold atoms

Perhaps the most successful of the techniques used to produce ultra-cold molecules, this scheme relies on the association of ultra-cold atoms in bound molecular states either by the absorption of a photon (photoassociation) [19] or through Feshbach resonances [20]. In photoassociation, the interacting ultra-cold atoms are resonantly pumped to a weakly bound excited molecular state. The first molecules produced using this scheme were Na_2 molecules [21]. Initially, the major drawback of this technique was that the lifetime of the produced molecules was very short (ns timescales). To overcome this, the weakly bound molecules were further optically pumped to deeply bound ro-vibrational states in the electronic molecular ground state. This method was used to produce K_2 [22] and RbCs [23] molecules in the μK temperature regime. Similarly, the same scheme can work by exploiting magnetically controlled scattering resonances, which occur when the total energy of the interacting atoms equals that of a bound molecular state. These resonances are known as Feshbach resonances. As was the case with photoassociation, the first molecules produced through Feshbach resonances were short-lived [20], however with subsequent adiabatic transfer to the molecular ground state via two or more optical transitions, this method has led to the production of deeply bound Cs_2 [24], KRb [25] and Rb_2 [26] molecules.

The major drawback of these techniques is that they are limited to the number of atomic species that can be laser cooled. However, since the produced molecules inherit the temperature of the individual atoms forming it, they present the major advantage of producing the cold molecules in the μK regime and have even lead to the production of the first molecular BEC [27].

Stark and Zeeman deceleration

Stark deceleration is perhaps the most widely used technique for slowing molecules from a molecular beam. In Stark deceleration, the interaction of the permanent dipole moment of a molecule with the applied electric field is exploited. Mainly limited by the fact that an electrostatic maximum in free space cannot be created [28], in this technique molecules are initially optically pumped to a low-field seeking state, since all molecules are high-field seeking in their absolute ground state. As a low-field seeking molecule approaches the electrodes of the decelerator, the Stark shift in its energy levels causes a gain in its potential energy and thus a subsequent loss in its kinetic energy. If the field was to be kept on, upon exit from the field created by the electrodes the molecule would experience a loss in its potential energy and subsequent regain in its kinetic energy. Instead, the field is switched off at the maximum of the kinetic energy loss and the process is repeated on several following electrode stages of the Stark decelerator. In its first experimental demonstration, through this scheme a beam of metastable CO was decelerated from 225 ms^{-1} to 98 ms^{-1} [29]. Subsequently, the method has been successfully applied to a variety of molecules such as NH_3 [30], OH [31, 32], H_2CO [33] and SO_2 [34]. The fundamental limitation of this technique lies in the fact that it can only be applied to molecules which possess a permanent dipole moment.

Zeeman deceleration operates in a similar way to Stark deceleration, by exploiting the Zeeman rather than the Stark effect, where magnetic fields are used to decelerate paramagnetic molecules. The technique was initially demonstrated in H [35] and O [36] atoms, while O_2 molecules where also decelerated from 389 ms^{-1} to 83 ms^{-1} [37].

Buffer gas cooling

As the name suggests, in the buffer gas technique dissipative cooling of atoms and molecules is achieved through elastic collisions of the species with a cold buffer gas [38]. The first species to be cooled using this scheme were CaH molecules which were laser ablated from a solid CaH_2 target and then cooled through their collisional interaction with the ^{3}He molecules of the buffer gas, which was maintained at a temperature of $\sim$ 300 mK [39]. Another demonstration of this technique was with the cooling of NH molecules, inserting the buffer gas cell from a room temperature beam [40]. This technique although successful, is fundamentally limited by the temperature of the buffer gas ($>$100 mK).

Cavity cooling

It has been proposed that molecules could be cooled to the mK regime while trapped in high-finesse optical cavities [41]. Here, the molecular kinetic energy is dissipated via a frictional force due to the coupled molecule-field dynamics. The energy is dissipated via loss from the cavity field and thus no closed cycling transitions are required rendering the technique ideal for molecules. Cavity cooling has already been demonstrated in a single Rb atom [42] and a gas of Cs atoms [43], but the applicability of the technique for molecules remains to be demonstrated.

Photodissociation

A technique also nicknamed "Photostop", photodissociation uses the recoil velocity of NO when dissociated from NO_2 to cancel out the molecular beam velocity [44] while the same principle has been used to produce ultra-cold Br atoms dissociated from Br_2 [45].

1.3 Motivation

The work presented in this thesis covers two different areas, as this was also outlined in Section 1.2. That of gas diagnostics in the form of coherent Rayleigh-Brillouin scattering and that of optical Stark deceleration, which aims to produce cold molecules. In the following sections I am outlining the motivation behind the on-going research in these areas.

1.3.1 Coherent Rayleigh-Brillouin scattering

Coherent Rayleigh-Brillouin scattering (CRBS) is a relatively new technique used for measuring the temperature, shear and bulk viscosity, rotational and vibrational relaxational rates of the gas in question. It is a non-resonant $\chi^{(3)}$ process where, through the electrostrictive force induced by two crossed laser beams, gratings moving at a velocity defined by the frequency difference of the two beams are formed in the gaseous medium while a third beam, incident at the Bragg-angle, is scattered from them. Measuring the intensity of the Bragg scattered beam with respect to the velocity of the grating, results in the CRBS spectra from which information about the gas is derived.

CRBS has already been successfully used as a probe for combustion and flow velocimetry [46] as well as for measuring the temperature of a flame [47], while its use has already

been proposed for nanoparticle detection [48]. There exists good theoretical background and understanding of the technique [49, 50, 51, 52, 53, 54], however the experimental aspect of the technique has still got distance to cover. Although coherent Brillouin scattering (hydrodynamic regime of CRBS) had been experimentally demonstrated in the liquid [55, 56, 57] and solid [58, 59, 60] phases, it had not been demonstrated and studied in the gas phase. More importantly, the technique had limited applicability in fast changing environments, such as combustion and transient flow, due to the slow acquisition times.

1.3.2 Production of cold and ultra-cold molecules

Cooling techniques such as the ones applied to atoms cannot be used in the case of molecules, due to their lack of closed cycling transitions, attributed to their complex energy level structure. Cold (<1 K) and ultra-cold (<1 mK) molecules have the potential to make substantial contribution to fields such as cold and ultra-cold chemistry, high precision spectroscopy and many-body physics. Here I am only going to outline the most important applications of cold and ultra-cold molecules; refer to [61, 62, 63] for a more detailed discussion.

Cold chemistry

At ultra-cold temperatures, chemical reactions between molecules become quantum in nature. At these temperatures complete control over the chemical reactions is possible [64, 65], through the control of the quantum state via e.g. the spin state, thus allowing or preventing a reaction from taking place [66]. This is different in nature to chemistry occurring at "normal" temperatures where reactions are simply the average of many particle interactions. Also, although the chemical reaction rate is expected to decrease with lower interaction energies, at ultra-cold temperatures this rate is actually enhanced due to quantum tunnelling overcoming the repulsive barrier [67]. Precise control over the velocity of the reacting molecules also allows for detailed experimental investigation of both elastic and inelastic collisional cross-sections. This was initially demonstrated through the interaction of Stark decelerated OH molecules with Xe [68], He and D_2 [69] while more recently inelastic collisions of NO radicals with He, Ne and Ar were studied [70]. These are only some of the potential applications of cold molecules in chemistry. Wider availability of cold molecules will allow this relatively experimentally unexplored area to be further

studied as well as will allow the control of chemical reactions.

High resolution spectroscopy

High resolution spectroscopy of atoms, ions and molecules has been an important tool for metrology, the measurement of fundamental constants and the test of proposed fundamental theories. The main limitation in achieving high resolution spectroscopy is the interaction time between the involved particle and the field used to study it. In the case of ions, this can easily be overcome by trapping the ions in electrostatic traps almost indefinitely, thus allowing for long measurement times. This arrangement has allowed for high precision measurement of the electron magnetic moment [71] as well as the fine structure constant α [72]. In the case of atoms, this was overcome with the introduction of laser cooling techniques which allow very long interaction times since effectively the atoms can be held at a standstill. These spectroscopic techniques have led to the development of atomic clocks which now provide the world's standard for time [73].

In the case of molecules where laser cooling cannot be applied, there is currently a large experimental effort to produce slow molecular beams which could thus enhance the interaction times. A beam of cold $^{15}ND_3$ propagating at a velocity of 50 ms^{-1} has been used to measure the molecular hyperfine structure [74]. There is also intense on-going research about the determination of the electron's permanent electric dipole moment (EDM), as its existence would imply physics beyond the standard model since it requires both parity (P) and time-reversal (T) invariance violation [75]. The electron's EDM d_e can be measured by applying an external electric field to an atom/molecule and measuring changes in its energy. This energy change is given by $d_e P(E) E_{int}$, where $P(E)$ is the degree of polarisation of the atom/molecule in the applied field and where E_{int} is the effective electric field from the atom/molecule which is proportional to the cube of the nuclear charge and hence heavy particles are preferred for such measurements since they offer the highest sensitivity. Such measurements have been performed with ^{205}Tl atoms [76], YbF molecules [77, 78] and more recently ThO molecules [79]. By producing even colder samples of heavy polar molecules, even larger interaction times should be achievable allowing for a more precise measurement of the electron's EDM.

1.4 Outline of this thesis

I will begin by describing in Chapter 2 the laser system that was used in all of the experiments described in this thesis. I will also report on the development of a new laser source for producing frequency agile laser pulses, offering frequency excursions of up to 1.5 GHz.

Following the manifestations of molecular polarisability as presented in Section 1.2, I will continue by presenting in Chapter 3 the history and theory of CRBS. In Chapter 4, I will present the first measurement of coherent Brillouin scattering in the gas phase using constant velocity lattices, while in Chapter 5 I will present a method by which we have reduced the acquisition times for CRBS by ten orders of magnitude by using chirped optical lattices.

In Chapter 6 I will present the theory of optical Stark deceleration (OSD) and provide a comparison between constant velocity and chirped lattice OSD, while in Chapter 7 I will present the progress in experimental implementation of chirped optical lattice OSD incorporating a Raman tagging scheme to differentiate from the molecular gas background, the molecules that have been decelerated.

Conclusions, final remarks and suggestions for future experiments will be presented in Chapter 8.

Chapter 2

Laser development

2.1 Introduction

Optical Stark deceleration and coherent Rayleigh-Brillouin scattering require a laser system capable of delivering high energy, flat top pulses of controllable frequency and duration. Such laser systems are not commercially available and our research group has developed an experimental setup designed to meet these specifications. This system has already been successfully used in our group for laser driven acceleration of Ar^* atoms [80], coherent Brillouin scattering [81] and single shot coherent Rayleigh-Brillouin scattering [82] in gases. Nevertheless there were issues with its thermal stability and pulse shaping efficiency. In this chapter, I will describe the construction of a new microchip laser as well as modifications made to the laser system.

2.2 The laser system

The laser system developed by our group is shown in Fig. 2.1. This laser system is capable of producing laser pulses with energies up to 700 mJ per pulse, with variable pulse durations between $10 - 1000$ ns, while producing linearly chirped pulses with frequencies up to 1.5 GHz.

A continuous wave (CW) Nd:YVO_4 microchip laser provides the two frequencies required for chirping. The frequency is modulated via application of voltage to an intracavity electro-optic modulator (EOM). Frequency excursions of up to 1.5 GHz with tuning rates of 15.4 ± 0.3 $MHzV^{-1}$ were achieved with this microchip laser, whilst it was operating in single mode with an output power of $\sim$ 10 mW [62]. This seed laser (called the *master*

laser) is injection seeded into a second laser diode (called the *diode laser*) emitting at ~ 1064 nm in a master-slave configuration. This arrangement is used to suppress intensity modulation introduced by relaxation oscillations in the master laser, which could result in a modulation of up to 30% in the intensity output of the system. By using the master-slave configuration we are forcing the slave diode laser to emit at the frequency of the master oscillator, without it being affected by the variations in its output intensity.

The output of the slave laser diode is input into a commercial 1 W fibre amplifier[1]. The output of this Ytterbium based amplifier goes through a Pockel's cell which is driven by a pulse shaper made by Kentech, which "chops" the CW beam into two individual pulses with a set time difference between them. The reason for having two pulses is that, as soon as the first pulse has been let through the Pockel's cell, a voltage signal is sent to the master laser's intracavity EOM so that the second pulse has a desired frequency difference with respect to the first pulse. The operation of the pulse shaper will be discussed in more detail in section 2.4. Finally, these two pulses are injected into two optical fibres of 10 and 65 m length, which introduce a 275 ns delay, setting a time difference between the two laser pulses.

The last stage of amplification comes from a custom made, commercial, flash lamp pumped, triple stage Nd:YAG amplifier[2]. This amplifier has two identical arms, one for the amplification of each of the two pulses that are delivered by the two fibres. Each arm is comprised of three 10 cm long Nd:YAG rods, each pumped by its own flash lamps. Between the second and the third rod, there is a Pockel's cell, which allows for the switching of the arm. This way, we can control in which of the two incoming pulses most of the arm's energy will go to. Therefore, in the arm which is seeded by the 65 m long fibre the switch will allow for both pulses to pass, with most of the energy being coupled to the first (unchirped) pulse, whilst on the arm that is seeded by the 10 m long fibre, the switch will open right in time for only the second (chirped) pulse to pass. Thus, when the two resulting pulses are interfered on the output of the custom made amplifier, they will create an interference pattern defined by the voltage signal initially applied to the EOM.

[1] IPG YAR-1K-LP-SF

[2] designed and constructed by Continuum

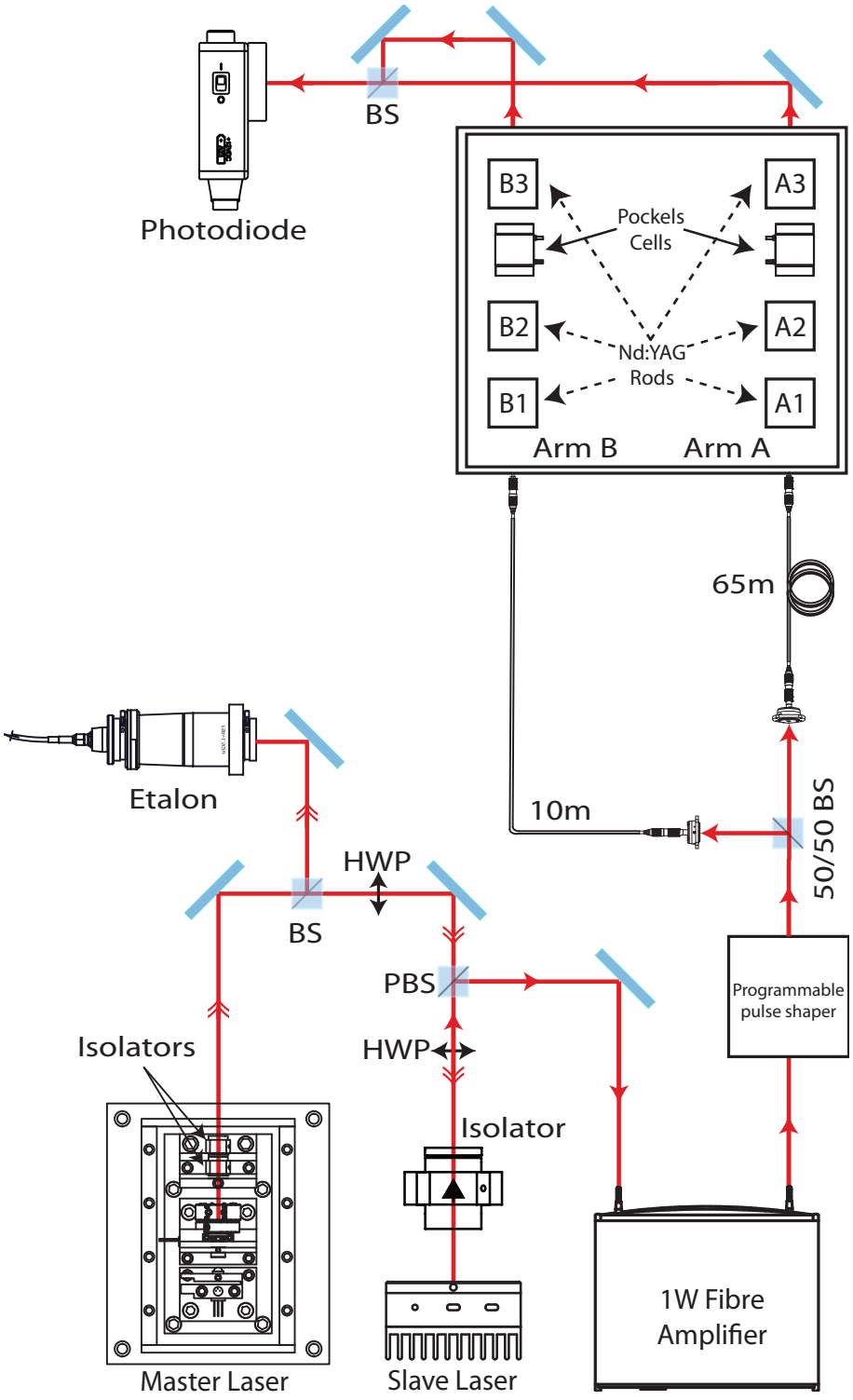

Figure 2.1: Schematic of the laser system that was developed by our group for particle deceleration/acceleration and gas scattering diagnostics. The master oscillator is injection locked to the slave laser diode, whose output seeds the fibre amplifier. The amplified CW beam goes through a Pockel's cell that "chops" the beam into two pulses, which are injected through two fibres in the two arms of a custom made, pulsed amplifier.

2.3 A new microchip laser

The laser system presented in section 2.2 was used for all of the work presented in this thesis. However, the microchip laser suffered from thermal stability due to its open construction; it was exposed to air current and temperature drifts in the lab, causing frequency and output intensity variation on a daily basis. Also, its output power of $10-15$ mW was only just sufficient to force the slave to lock to its frequency. These two issues would cause the laser to regularly come out of lock. This section presents the design of a new laser which addresses these problems.

Although we could have used a laser diode as a master laser in our system and tuned its frequency by changing the temperature and/or current, a neodymium (Nd) based diode-pumped solid state (DPSS) laser is preferable in order to match the emission spectrum of the amplifier. A microchip laser configuration for our DPSS laser was chosen since, the shorter the laser cavity, the larger the free spectral range (FSR) of the laser. The prerequisite for the shortest cavity length possible also dictates the dimensions of the crystals to be used.

In order to match the emission spectrum of the Nd rods of the amplifier, we chose an Nd based crystal. Nd:YVO_4 is preferred to Nd:YAG since it exhibits five times higher stimulated emission cross section than Nd:YAG and a strong broadband absorption at 809 nm, which means that it can easily be diode pumped, about seven times higher than that of Nd:YAG along the π direction [83, 84]. Finally, Nd:YVO_4 exhibits natural birefringence producing a laser output that is linearly polarized along the extraordinary π direction.

The high gain achievable in Nd:YVO_4 and its high absorption coefficient, allows for lasing from crystals of minimal lengths, which is what is required for our application. The only drawbacks exhibited by Nd:YVO_4 crystals are low thermal conductivity (about one-third that of Nd:YAG [84]) and a shorter upper state lifetime than Nd:YAG (100 μs compared to 230 μs). For these reasons, the crystal that was chosen was a commercially available[3] YVO_4 crystal with dimensions of $3 \times 3 \times 0.5$ mm, 3% doped with Nd, with its sides coated as shown in Fig. 2.2.

For our intracavity EOM, a $LiTaO_3$ crystal was chosen because of its high electro-optic coefficient which results in a relatively low half-wave voltage. The crystal had dimensions $1 \times 3 \times 5$ mm with a half-wave voltage of 140 V and both sides anti-reflection (AR) coated

[3] Casix

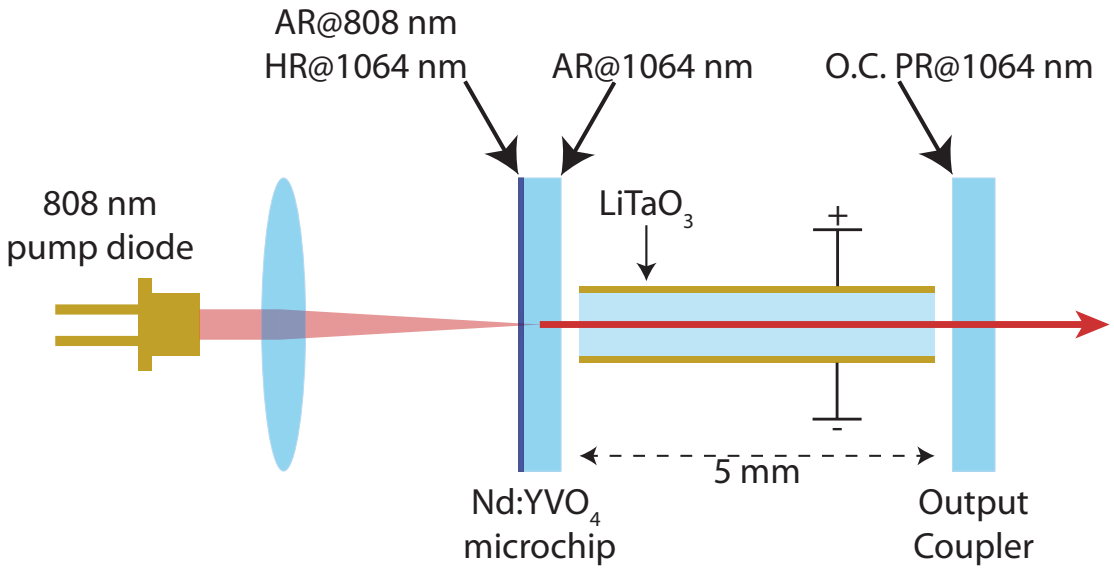

Figure 2.2: Schematic of the microchip laser. Voltage is applied on the two gold plated sides of the $LiTaO_3$ crystal, in order to change its refractive index and hence the frequency of the laser output. HR refers to highly reflective coating, AR to anti-reflective coating and PR to partially reflecting coating on the repsective optical elements.

for 1064 nm.

Furthermore, in contrast to the plane-plane cavity configuration that was used in the previous implementation, a plane-concave configuration was chosen in this new setup, by using a 100 mm R.O.C. concave output coupler. With the use of a concave output coupler (OC), the cavity's stability would fall within the stability diagram, removing the necessity of thermal lensing in order for lasing to occur. This way, greater optical power is expected as well. Since practice has shown that there is no accurate way to simulate the performance of a solid state laser depending on the partial reflectance of the output coupler, two mirrors of 95% and 98% were ordered to be used in the laser. Figure 2.2 presents a schematic of the laser cavity that was designed for the new DPSS microchip laser.

It is important that most of the cavity length be filled by the EOM since the frequency change δf of the laser, with applied voltage δV, is given by [85]:

$$\delta f = \frac{\eta n_1^2 r_{33} f_{\text{opt}}}{2d} \frac{n_1 l_1}{n_1 l_1 + n_2 l_2 + n_3 l_3} \delta V \tag{2.1}$$

where l_1, l_2 and l_3 are the lengths of the $LiTaO_3$ crystal, the $Nd:YVO_4$ crystal and the air gaps, respectively, with n_1, n_2 and n_3 their respective refractive indices. The coupling efficiency between the applied electric field and the laser cavity mode is given by η, d is the thickness of the EOM crystal and r_{33} its electro-optic coefficient, while f_{opt} is the

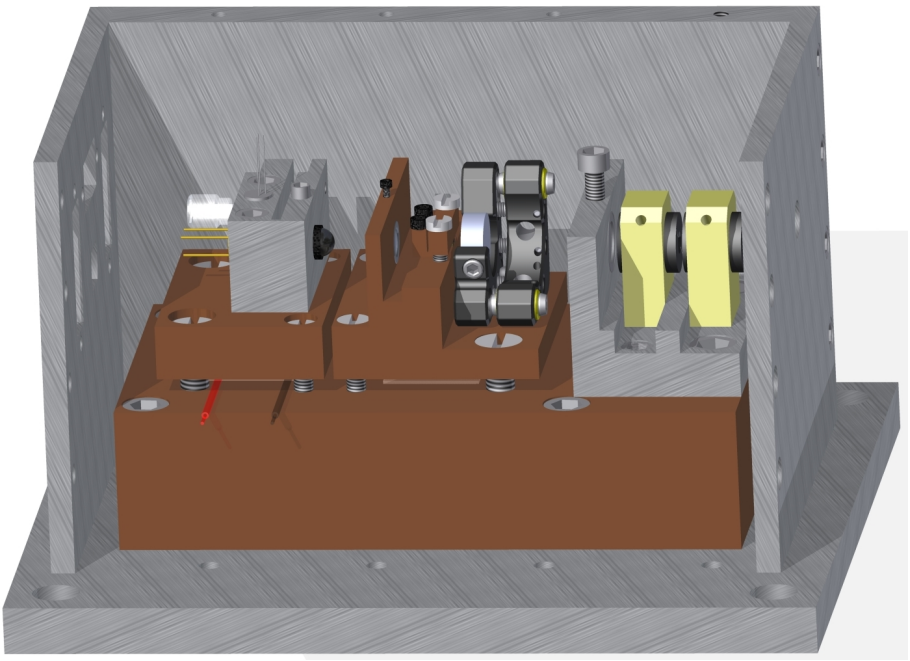

Figure 2.3: Rendered image of the final laser design. On top of the main copper block one can observe, from left to right: a copper block which houses the pump diode and a collimator, a copper block in the middle which houses the focussing lens and the main optical cavity, and an aluminum block which houses a laser line filter for 1064nm and two isolators. The design was made using Autodesk Inventor.

main optical frequency within the cavity. It is apparent from Eq. 2.1 that the smaller the product $n_3 l_3$, the larger the frequency of the laser can be tuned. However, although ideally the air gap should be zero, in practice some distance between the crystals is desired in order to eliminate the possibility of one of the crystals breaking due to mechanical pressure.

In order to improve thermal stability, the pump laser and the optical cavity need to be thermally isolated from the environment and any temperature regulation should be stable. The solution chosen was for the laser components to be mounted on copper blocks, which sit on Peltier elements, mounted to a large copper block (see Fig. 2.3) which, through the casing of the laser would also be in thermal contact to the optical bench. This provides a large thermal sink for the Peltier elements. It is also noteworthy that both the block that houses the pump diode and the block that houses the Nd:YVO_4 crystal have their respective temperatures individually controlled through separate Peltier elements whilst sitting on the same copper block (Fig. 2.3).

Finally, the whole system is mounted in the same aluminium box, which improves mechanical stability. Figure 2.3 is a rendered image of the new monolithic microchip laser.

2.3.1 From design to realisation

In order to initially align the laser cavity, we followed the standard procedure using a HeNe laser. With the output coupler removed, we aligned the back reflected light from the crystal beam to the forward propagating one. We then installed the output coupler and moved it in such a way so that its back reflected beam would also propagate along the forward propagating beam path. It is noteworthy that we opted for a rear loading mirror mount for the output coupler so that we could follow this alignment procedure.

With the cavity aligned, the only thing left to be done was to focus the pump beam on the crystal. The optimum point (or close to it) was easily determined by naked eye, since the Nd:YVO_4 was fluorescing. So at the point of maximum fluorescence, there should be enough absorption to allow for initial lasing. By setting the pump laser's current at maximum, and small adjustment of the output coupler's mount, lasing was easily achieved.

2.3.2 Characterising the new laser

Finding the pump laser's optimum operating point

Before starting to characterise the Nd:YVO_4 laser itself, we had to characterise the 808 nm pump laser first. The diode that was used to pump the Nd:YVO_4 crystal had a maximum optical power of 1 W at 2.5 A driving current [4]. Pump current versus optical power curves (I-P curves) were obtained for various temperatures of the diode (Fig. 2.4). From these curves one can obtain the threshold current of the laser (the current at which lasing starts occuring) as well as the slope efficiency of the laser. The smaller the threshold current, the larger the slope efficiency and the more linear the I-P curve is, the better the laser diode in examination since it delivers the maximum power for minimum current.

In order for these measurements to be taken, a LabVIEW program was written. This controlled the DC offset of the output of an arbitrary waveform generator [5] which modulated the current output of a current driver [6]. The driver provided current to the laser diode at the output of which we had placed a silicon photodiode [7], which was connected to a digital power meter console [8]. The temperature of the diode was controlled by a

[4] L808P1WJ multimode diode by Thorlabs
[5] Thurlby-Thandar 12100
[6] Thorlabs LDC220C
[7] S121C by Thorlabs
[8] PM100D by Thorlabs

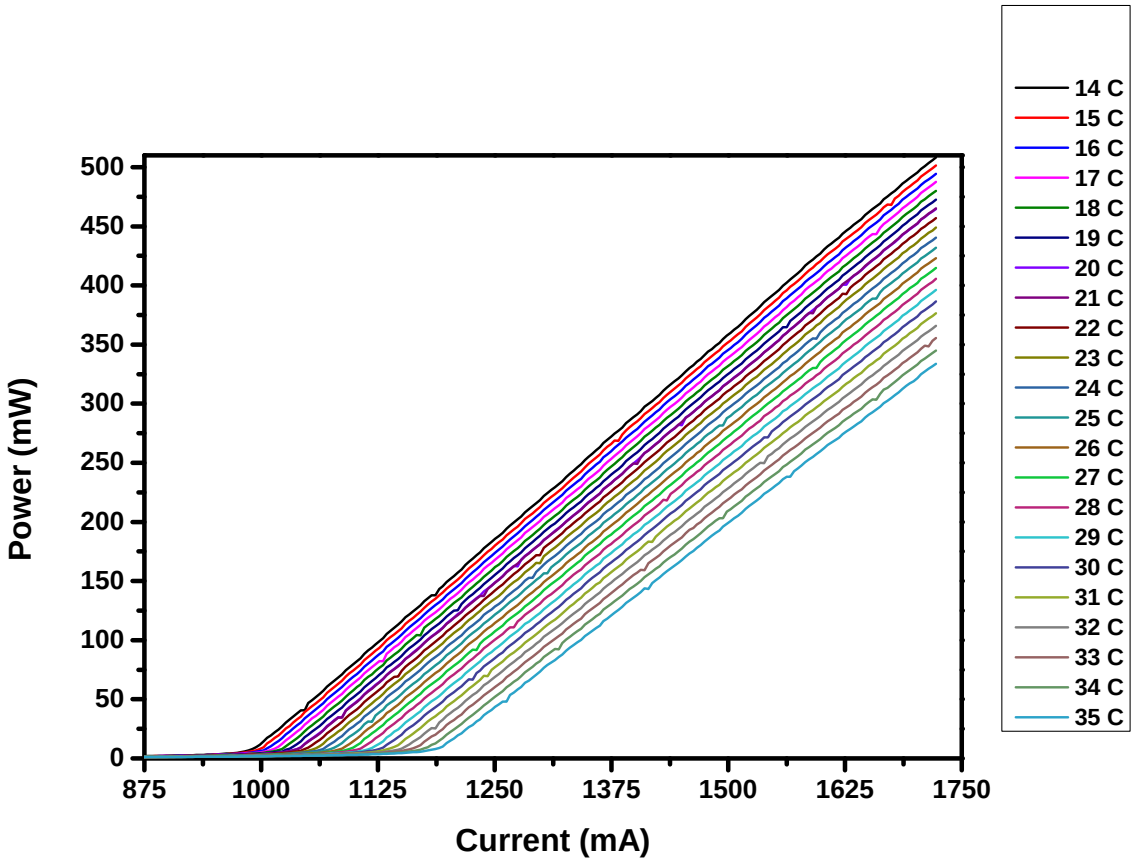

Figure 2.4: Characteristic I-P curves of the laser diode used for the laser, for different temperatures. The measurements were taken up to an optical power of 500mW so that we wouldn't exceed the photodiode's power limit.

TEC controller [9]. By changing the DC offset of the waveform generator, and logging the measured power as this was measured on the photodiode, we obtained the characteristic I-P curves for different temperatures of the photodiode. These are shown in Fig. 2.4.

From Fig. 2.4 we observe that for the 21 ^{o}C temperature range over which these measurements were performed, there is a $\sim$ 200 mA change in the threshold point as well as a $\sim$ 175 mW difference in the output optical power. From the graph presented in Fig. 2.4 we can also obtain the characteristic temperature of the laser diode. The characteristic temperature is an inherent property of each laser diode and shows the temperature sensitivity of the threshold point on a laser diode. It is given by:

$$I_{\mathrm{Th}} = I_0 e^{\frac{T_1}{T_0}} \tag{2.2}$$

where I_{Th} is the pump current at threshold for a temperature T_1, and I_0 is the pump current at threshold for the characteristic temperature T_0. The less the threshold current of

[9] Thorlabs TED200C

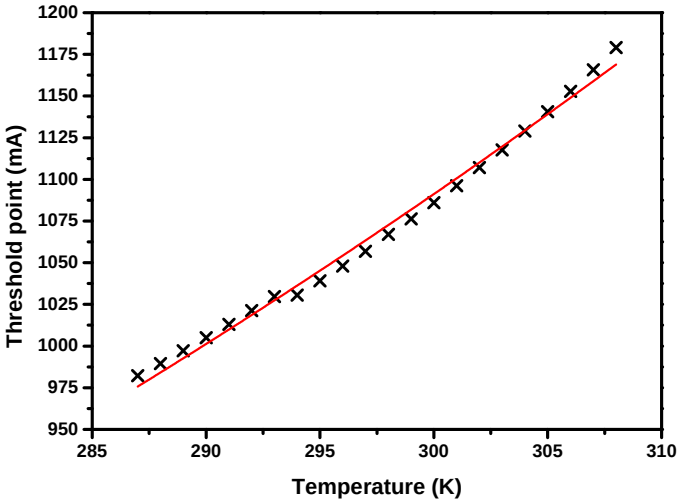

Figure 2.5: Pump current at threshold versus temperature (black trace). The red trace if the fitted exponential by which we can obtain the value for the characteristic temperature of the laser diode.

the laser diode increases with increasing temperatures, the higher the characteristic temperature T_0 is [86]. This translates into the laser being more thermally stable. By plotting the pump current at threshold for various temperatures and fitting an exponential curve to these data as shown in Fig. 2.5, we obtain a value for the characteristic temperature of the laser diode of 116 ± 21 K, which is a typical value for this type of diodes.

It is clear from the data obtained that to maximise power output, the diode should be operated at the lowest possible temperature. One must avoid condensation though, which occurs around 14^oC hence an operating point of 16^oC was chosen.

For completeness, one has also got to do an absorption measurement on the active medium with respect to the pump diode's temperature, since the diode's emitting wavelength changes with respect to the temperature. Due to the dimensions of the copper block housing the crystal it wasn't physically possible to place the photodiode right after the crystal. Also, because the pumping diode's beam was highly diverging, that measurement could not be performed away from the crystal housing block. Though, since the Nd:YVO_4 crystal's absorption curve shows a very good linearity in the $807-813$ nm region [87], that step was safely decided to be skipped.

Choosing the best output coupler.

The next step in configuring the laser was to choose the output coupler with which we would obtain a higher and more stable laser output power. For that reason, we took an I-P curve for each of the two output couplers we had. Now the efficiency of the laser could

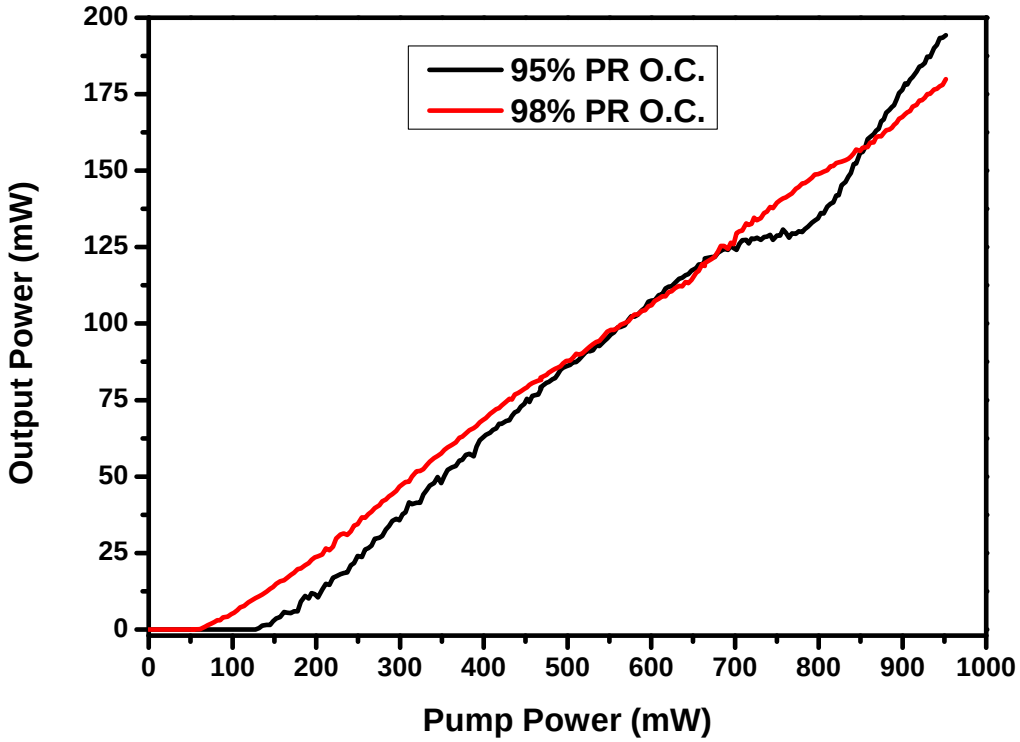

Figure 2.6: I-P curves for the Nd:YVO_4 laser, for two O.C. with 100 mm radius of curvature, and 95% and 98% partial reflectivity (PR).

be determined, since we had already obtained the current to optical power calibration for the laser diode. Figure 2.6 shows the I-P curves obtained for the two output couplers.

If it had been maximum optical power we were aiming for, the clear choice according to the graphs presented in Fig. 2.6, would have been to use the 95% O.C. However, we require maximum power while operating at single mode and given the fact that in theory this cannot happen for values above five times the threshold value [88], the use of the 98% output coupler seemed the better choice for our laser. Besides, with the use of the former, the laser also had a smaller threshold point as well as a more linear and stable behaviour. With the use of the 98% output coupler, the threshold point for the laser was found to be 72.8 ± 1.1 mW (corresponding to 1075 ± 4 mA of pump current), whilst having a 20.36 ± 0.04% optical to optical slope efficiency.

Installing the EOM in place.

An EOM is added to the cavity to allow frequency chirping. Adding an extra element in the cavity imposes an extra loss mechanism, hence a poorer performance of the end laser is expected after installation. For the purposes of our laser characterisation this extra loss mechanism was considered to have the same effect for both output couplers used in the

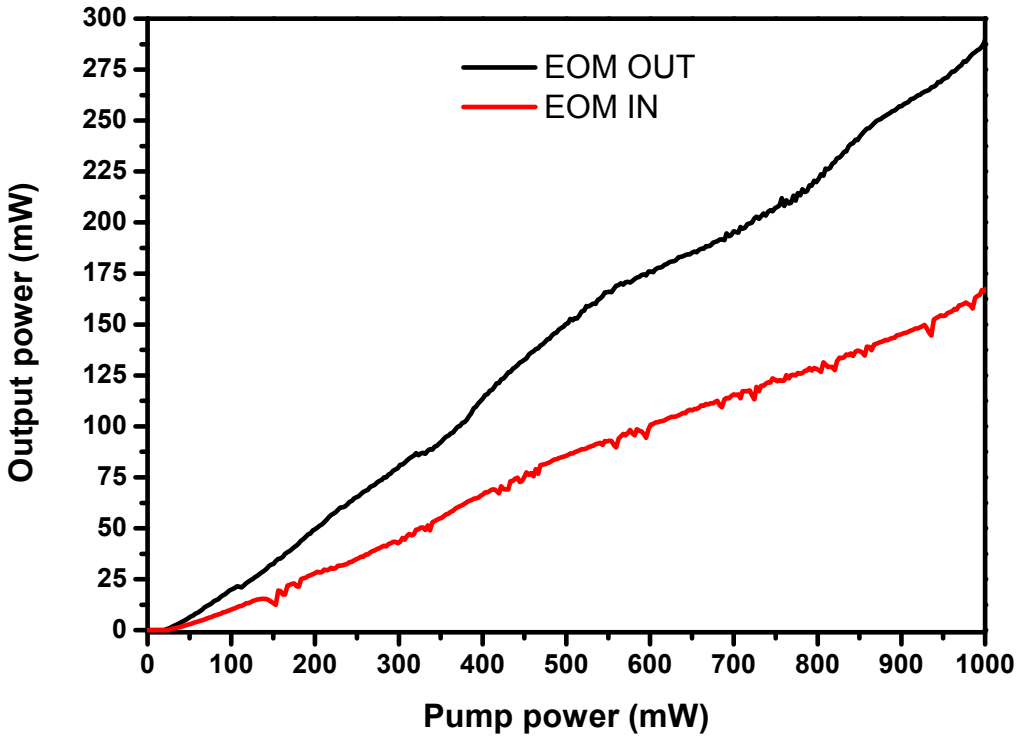

Figure 2.7: I-P curves for the laser without (black) and with (red) the EOM placed in the laser cavity.

laser cavity and cause an equal shift in performance for both values of partial reflectivity of the output couplers that we used. For completeness, one would have to accomodate for the extra loss mechanism by adjusting the partial reflectivity of the output coupler. Once the EOM was installed, another I-P curve was obtained and both these final I-P curves are presented in Fig. 2.7.

As expected, the performance of the laser in terms of output power drops with the EOM inside the cavity. However, the overall performance of the laser remains good, exhibiting a linear behaviour with respect to input power. Table 2.1 summarises the slope efficiencies and threshold points for the cavity with and without the intracavity EOM. The slope efficiency for the cavity without the EOM in place is comparable with what has been reported in the literature about lasers of this type which range from 28.1% to 58.6% [89, 90, 91, 92].

Table 2.1: Slope efficiency and threshold point for the cavity

	Threshold point (mW)	**Slope efficiency (%)**
EOM Out	24.5 ± 1.8	29.49 ± 0.09
EOM In	29.7 ± 1.9	17.02 ± 0.05

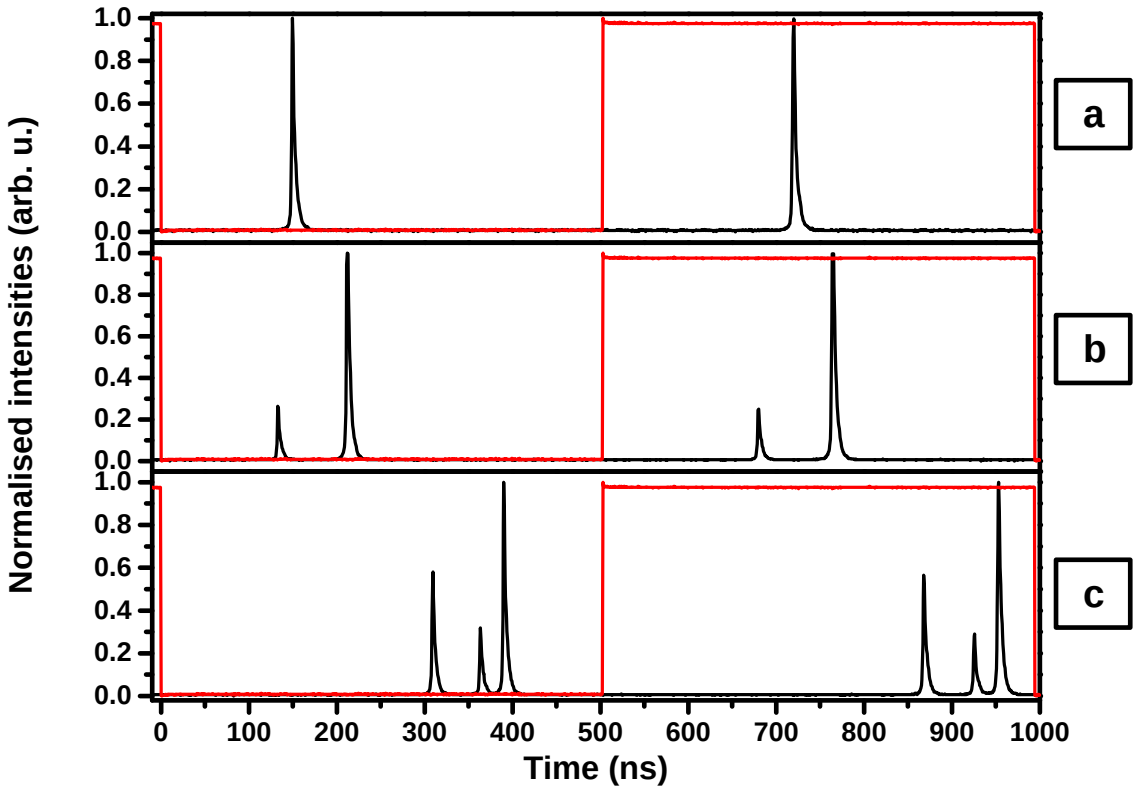

Figure 2.8: Single (a), dual (b) and multi (c) mode operation of the new laser is shown in the black trace. The red trace is the scanning window of the etalon.

Measuring the induced chirp.

The main aim in building such a laser is to be able to chirp the frequency of the laser output. In order to measure the induced frequency detuning, we monitor the frequency of the laser output with a scanning Fabry-Perot etalon[10]. Using this we can determine whether we are operating in a single-mode regime and the range over which we can tune the laser. Although we have measured up to 150 mW of optical power output with the EOM installed, this was not in single mode operation, as the extra pump power increases the gain of extra, unwanted laser modes. We do not expect that the laser will remain in single longitudinal mode at powers that are four to five times greater than the threshold power before other modes reach threshold [88, 93]. We thus have to decrease the pump power to a maximum measured value of 50 mW in order to achieve single mode operation. Figure 2.8 shows single and multi-mode operation of the laser.

In order to achieve the rapid and precise chirps that are required, we have to apply fast and precisely controlled voltages to the EOM. Ideally, one would wish to connect the EOM directly to the output of a waveform generator with a low jitter, high voltage, fast,

[10] SA200 – 8B by Thorlabs

gated electrical output. The voltage amplitude that is required for a big enough chirp, is proportional to the half-wave voltage, which is a figure of merit showing what voltage is required for the EOM to shift the phase of the input light by π, which represents a 90^o change in the polarisation of the input light.

In our configuration, a low voltage signal comes from a waveform generator [11], which is then further amplified by a voltage amplifier[12]. With this configuration we can get all desired waveforms (sinusoidal, ramp, etc.) up to 200 Volts in amplitude with a bandwidth up to 1.2 MHz. Although the chirp for deceleration only requires one linearly ramped electrical pulse per cycle, in order to characterise the frequency detuning performance of the laser we send continuous sinusoidal pulses to observe how the single mode laser peak is expanded to the familiar "bat-wing" shape from previous studies [94]. This "bat-wing" is caused by the Fabry-Perot interferometer scanning at a constant rate, while the frequency of the laser output is changing at a sinusoidal rate. Such a characteristic "bat-wing" obtained from our laser is presented in Fig. 2.9. By comparison between the 1.5 GHz window provided by the Fabry-Perot etalon (shown in red in figures 2.8 and 2.9) and the width of the bat-wing, we can get a rough estimate of the induced chirp.

The "bat-wing" presented in Fig. 2.9 is created by a continuous sinusoidal wave of 20 V amplitude and corresponds to a chirp of 297.4 ± 5.2 MHz. This yields a chirp rate of 14.9 ± 0.3 MHz/V which is almost the same as what was achieved in the laser system described in section 2.2 [95, 62].

2.3.3 A laser source for a variety of applications

The newly built laser did indeed meet the specifications as these were set in section 2.3. It is able to deliver the same chirp rate in single mode but with more than three times the output power. It has proven to be much more thermally stable than its predecessor and it achieves far better optical-to-optical slope efficiencies (17.02% compared to 2.5%) while being more robust and of smaller construction. Having both heat-producing copper blocks "sitting" on the same thermal bath was a risky approach, which isn't usually followed in laser designs as it can be the source of great thermal instability; it though did work as intended. Finally, it is constructed in such a way that, once enclosed, it is easy to move and to integrate into any optics laboratory with its mounting threads matching the standard

[11] Hewlett-Packard 3314A
[12] A.A. Lab Systems A303

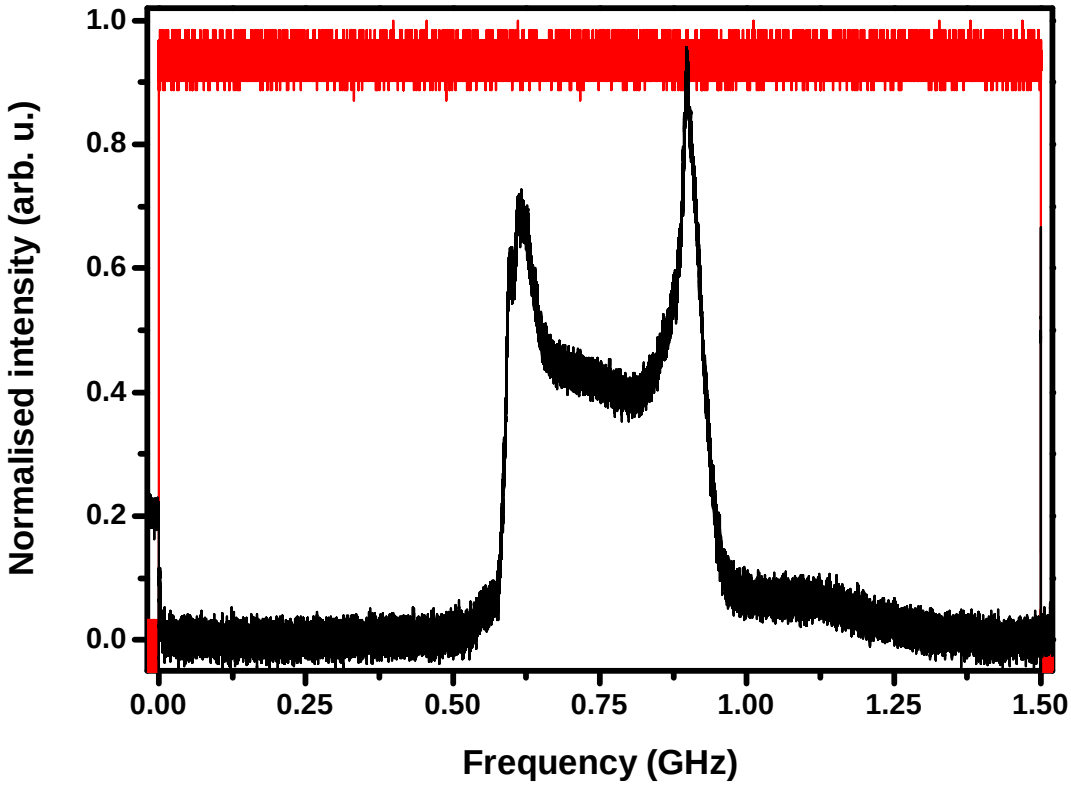

Figure 2.9: The characteristic "bat-wing" as obtained by our laser system (in black). In red is shown the scanning window of the Fabry-Perot interferometer, whose width corresponds to 1.5 GHz.

25.4 mm spacing and its electrical connections being connection ready for the industry standard current drivers, without having to interfere with the interior of the construction.

This laser was finished when the third of the three main experiments which will be presented in this thesis was about to start. Overall the whole of the laser system as it was presented in the beginning of this chapter was successfully used for some years by our group, especially after some modifications were made to it which improved its performance and stability. Although there is no reason why the newly built laser wouldn't be a good replacement to the old one, it was decided that since the whole system was performing as it should do, we shouldn't alter it; one simply doesn't change a winning team.

Instead, the new laser was decided to be used in another experiment carried out in our group, as a tuneable laser source to probe whispering gallery mode resonances in silica spheres. The laser has proven to be particularly stable in output intensity and temperature showing very little frequency hysteresis when probing for whispering gallery modes around the sphere. Finally, its frequency has been locked to a chosen resonant whispering gallery mode through an implementation of the Pound-Drever-Hall method by tuning through a feedback circuit the applied voltage on the intracavity EOM.

2.4 Pulse shaping

2.4.1 The theory

The Nd:YAG rods in the custom made amplifier would present a time dependent gain $G(t)$ during amplification [96]. This means that we need to correctly shape the input pulses $I_{\text{in}}(t)$ via the Pockel's cell driven by the Kentech pulse shaper in order for us to get the desired flat top output pulses $I_{\text{out}}(t)$. The relation between the input and output temporal profiles is given by [96]

$$I_{\text{out}}(t) = I_{\text{in}}(t) \times G(t), \tag{2.3}$$

where the time dependent gain is given by

$$G(t) = \frac{G_0}{G_0 - (G_0 - 1)e^{-U_{\text{in}}(t)/U_{\text{sat}}}}, \tag{2.4}$$

where $U_{\text{in/out}}(t) = \int_{t_0}^{t} I_{\text{in/out}}(t)dt$ and G_0 and U_{sat} are constants representing the initial gain and the saturation intensity, respectively. As we mentioned earlier, we require a flat-top intensity profile on the output, where I_{out} is a constant k and thus $U_{\text{out}} = kt$. We can hence specify the required gain profile $G(t)$ for a given output pulse shape in the presence of saturation as [96]

$$G(t) = 1 + (G_0 - 1)e^{-U_{\text{out}}/U_{\text{in}}}. \tag{2.5}$$

Since we have redefined U_{out}, Eq. 2.5 can thus be written as

$$G(t) = 1 + (G_0 - 1)e^{-kt/U_{\text{in}}}. \tag{2.6}$$

Therefore, the gain presents a maximum at $t = 0$ when $G(t) = G_0$. Substituting Eq. 2.6 into Eq. 2.3, yields that in order to obtain a constant intensity profile I_{out} in the output, we need to feed the laser amplifier with an exponentially increasing intensity $I_{\text{in}}(t)$ so that we compensate for the exponentially decreasing gain. However, the gain does not always show an exact exponential decay, while it also depends on input wavelengths, ageing and pumping conditions. For these reasons we require a precise and fast way of changing the input light's intensity profile to accommodate these effects.

2.4.2 Practical pulse shaping

The input light intensity to the custom amplifier is controlled by a Pockel's cell right before a polarising beam-splitter. Through an applied voltage, the Pockel's cell changes the polarisation of the incoming light and hence controls the intensity passed through the polariser. This operation is computer controlled by the pulse shaper.

The Pockel's cell driver[13] was supplied with software which communicated to the driver via an RS-232 port. The user has to alter an ASCII text file which is comprised of 1500 lines, each representing a 7 ns time bin. By changing the value of each time bin with a value between 0 and 3000, one could change the voltage applied to the Pockel's cell for that time bin, and consequently the polarisation shift for that time bin, with the arbitrary 3000 value representing the maximum shift (i.e. voltage) that could be applied. Once the text file had been changed to the desired values, it was converted by the software to the format that could be understood by the instrument and was uploaded to it.

It is easily understood that getting a flat intensity profile in the output of the amplifier, by having to manually insert exponentially increasing values on a text editor, was not an easy or time effective task for one to perform. Also, with time passing the gain of the rods of the pulsed amplifier would be altered, meaning that the process would have to be done multiple times. This had often taken us up to five hours to get a desired profile using this software.

To optimise this process, I wrote a LabVIEW based software (Fig. 2.10), taking advantage of the fact that we would only need to change up to 23 time bins per pulse, since the difference between the two pulses was fixed by the length of the two fibres. Rather than having to manually change a text file, a graphical interface was made, where the user only has to change 23 slides on a graphic equaliser. By displaying the program on a touch-screen monitor, the necessity for any keyboard input is also removed. Additionally, the input intensity graphs are plotted in real time and extra functions such as save/recall, decrease/increase by a fixed amount or percentage etc. have been implemented. This interface massively simplifies and speeds-up the pulse shaping process, taking it down to just $5 - 10$ minutes.

[13] By Kentech

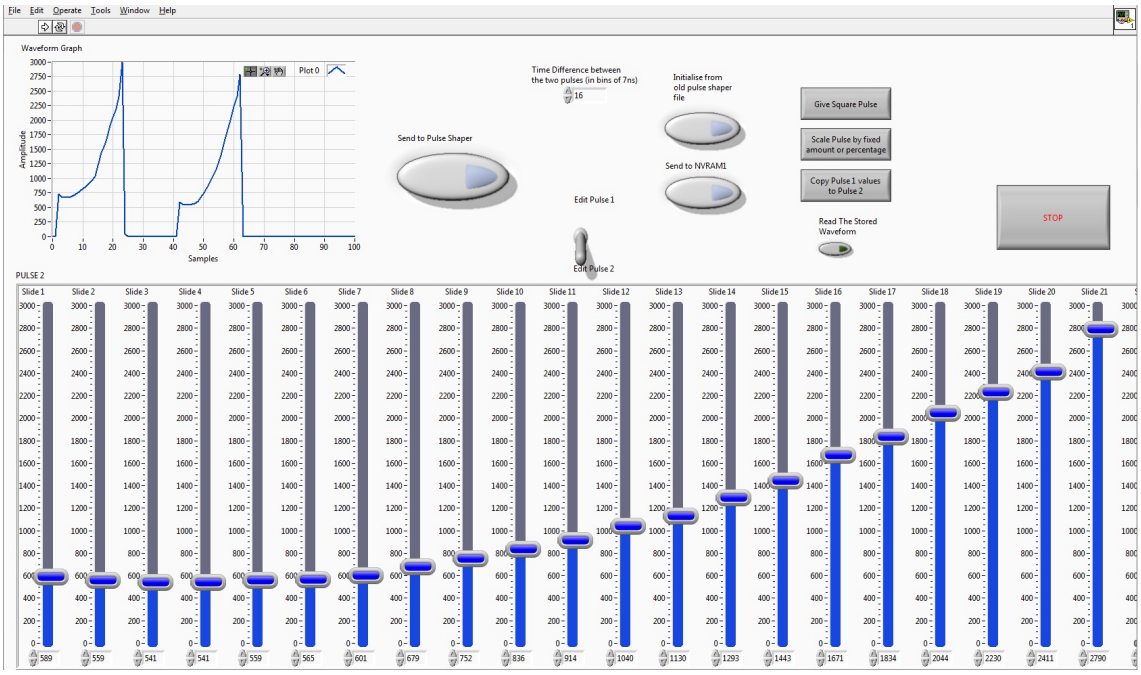

Figure 2.10: The graphical interface of the program that was written to control the pulse shaper. On the top left the real time plot of the input intensity profiles with the "Send to pulse shaper" button right next to it. The other buttons give access to extra functionality, while the switch changes which of the two pulses is being configured.

2.4.3 Analysing the pulsed frequency chirp

In order to characterise the chirping performance of the total laser system, it was necessary to measure and analyse the chirp after amplification, and not just the chirped output of the microchip laser. Apart from determining the chirp rate of the pulsed output, we are also interested in seeing whether extra chirp is induced due to temperature and gain fluctuations in the Nd:YAG rods of the pulsed amplifier, as was the case in [97]. In order for the chirping rate after amplification to be measured, the outputs of both arms of the amplifier were combined on a 50/50 beamsplitter and were aligned so that they were copropagating for a great distance before being heterodyned (beat) on a fast InGaAs photodiode[14] with a bandwidth of 2 GHz. In order for the contrast of the beating to be maximised, neutral density filters were used on both beam paths. The signal from the photodiode was measured by an oscilloscope[15] of bandwidth of 3 GHz.

Consider two waves of the same amplitude travelling in the same direction with electric

[14] Hamamatsu Photonics G6854-01
[15] LeCroy WavePro 7300

fields E_1 and E_2 given by [98]

$$E_1 = E_{01}\cos(k_1 x - \omega_1 t), \tag{2.7a}$$

$$E_2 = E_{01}\cos(k_2 x - \omega_2 t), \tag{2.7b}$$

where E_{01} is their maximum amplitude, $k_1 > k_2$ and $\omega_1 > \omega_2$. The combined field would then be given by

$$E = E_1 + E_2 = E_{01}[\cos(k_1 x - \omega_1 t) + \cos(k_2 x - \omega_2 t)], \tag{2.8}$$

which can be reformulated as:

$$E = 2E_{01}\cos\frac{1}{2}[(k_1 + k_2)x - (\omega_1 + \omega_2)t] \times \cos\frac{1}{2}[(k_1 - k_2)x - (\omega_1 - \omega_2)t]. \tag{2.9}$$

If we define $\omega_m \equiv \frac{1}{2}(\omega_1 - \omega_2)$ and $k_m \equiv \frac{1}{2}(k_1 - k_2)$, where ω_m is the modulation frequency and k_m is the modulation propagation number, then through analysis, it follows for the intensity ($I \propto E_0^2$) which is what can be measured by the photodiode [98]

$$E_0^2(x,t) = 4E_{01}^2\cos^2(k_m x - \omega_m t) = 2E_{01}^2[1 + \cos(2k_m x - 2\omega_m t)]. \tag{2.10}$$

It is apparent from eq. 2.10 that $E_0^2(x,t)$ oscillates about a value of $2E_{01}^2$ with an angular frequency of $(\omega_1 - \omega_2)$ which is known as the *beat frequency*. If the two overlapping waves had different intensities, they would still produce beating, but the cancellation would be incomplete. Hence it is necessary to equalise the intensities of the two output beams. In our case, with the chirped frequency output, the beat frequency is given by $(\omega(t) - \omega_0)$, where $\omega(t)$ would be the time varying frequency of the chirped pulse, defined by the voltage signal applied to the intracavity EOM and ω_0 the initial frequency of the microchip laser's output.

In order for the instantaneous frequency $f(t)$ of the beat signal to be determined across the pulse duration, we use the analysis technique of Fee *et al* [99]. In this technique the two output beams creating the lattice are heterodyned on a photodiode and their relative chirped frequency components are extracted from this beat signal. In Eq. 2.10 the term in the cosine is the time dependent phase of the combined disturbance, the derivative of

which gives the instantaneous frequency $f(t)$. If we rearrange Eq. 2.10 we obtain

$$E_0^2(x,t) = 2E_{01}^2 + 2E_{01}^2 \cos(2k_m x - 2\omega_m t), \tag{2.11}$$

where the argument in the cosine is the instantaneous phase $\phi(t) = 2k_m x - 2\omega_m t$. We see that for the determination of the instantaneous frequency we need to separate the oscillating term in Eq. 2.11 from the first intensity term and measure how the phase changes with time on top of its oscillation every 2π. Since in most cases the cosine term in Eq. 2.11 oscillates at a higher frequency than the intensity term, we can initially perform a Fourier transform on the beat signal and then apply a band pass filter to isolate the higher frequency oscillating term. Then we can apply an inverse Fourier transform on the filtered frequency data to go back to the time domain and get the instantaneous phase $\phi(t)$ through a phase unwrapping algorithm. Finally, in order to get the instantaneous frequency $f(t)$ we only need to differentiate the phase with respect to time, $f(t) = \frac{1}{2\pi} d\phi(t)/dt$.

This analysis was carried out in MATLAB by previous members of our group [62, 61]. For the purposes of the work presented in this thesis, this code was incorporated in LabVIEW, allowing us to monitor in real-time the resulting chirp.

2.5 Conclusions

The laser system that was presented in this chapter has indeed worked and served our group for several years now. Depending on where we operate on the gain profile of the Nd:YAG rods in both arms, we have measured up to 700 mJ of output energy per arm, and linear chirps of up to 1.5 GHz. The system creates chirped interference patterns starting from a single laser beam. This removes the complexity of having to couple the frequency of one laser to another, and then having to change the frequency of one with respect to the other. Most of the experimental work presented in this thesis will be based on the chirped interference patterns that can be created by the laser system described in this chapter.

Chapter 3

Scattering of light by molecules

3.1 Introduction

Scattering of light from particles over the past century has been an invaluable tool for the determination of inherent particle properties with unprecedented accuracy and relative ease. In this chapter I will outline how light scattering has become such an important field of study in science and engineering. As we are mainly going to explore in the following chapters the scattering of light by gas molecules, this is going to be our main approach throughout the present chapter, unless specifically specified.

Scattering of light by particles can be categorised in two main categories, which arise from how the energy is conserved. *Elastic scattering*, where the energy of the scattered photon has got the same frequency as the incident ones and *inelastic scattering*, where the energy of the scattered photon is higher or lower frequency. The former are anti-Stokes photons, whereas the latter are Stokes photons.

Scattering was not always thought to be the mechanism by which photons were deflected by gaseous (mostly) matter. One of the main questions that had for a long time troubled physicists, and which mostly drove the scattering study, was why the sky appeared blue. Indeed, since earlier natural philosophers didn't know about the existence of molecules, they thought that the sun's light was reflected and refracted somehow on something, making the sky appear blue.

It was Leonardo Da Vinci, who observed that thin smoke when illuminated by sun light, appeared to have a "beautiful blue colour" against a dark background [100, 101]. Comparing this observation to the blueness of the sky, he came to the conclusion that sun light was reflected by small particles in the atmosphere. Isaac Newton on the other

hand, despite the fact that he proved the composition of "white" light to be the sum of all the colours, attributed the blue sky to first-order interference in water droplets in the sky, whereas Rudolf Clausius suggested that these droplets should be hollow in order to refract blue light [101].

This was soon over-ruled by Arago's finding in 1809 that the light in the sky is polarised by 90° instead of 76°, which would be the case if light was indeed refracted by water bubbles. The situation was troublesome for the physicists of the time, as depicted by Sir John Herschel [102]: *"The cause of the polarisation is evidently a reflection of the sun's light upon something. The question is on what?"*. The penultimate step in understanding the colour of the sky came from Tyndall in 1868 who, by noticing sky-blue colour in a beam of light in photochemical smog, realised that he saw the same colour independent of the refractive index of the aerosols he used (hence reflection could not have been the mechanism) and believed that the smog clouds contained particles "*whose diameters constitute but a very small fraction of the length of a wave of violet light*" [101].

3.2 So why is the sky blue?

The answer to these troublesome questions came with the works of John Strutt, 3^{rd} Baron of Rayleigh, who with his first papers on the matter [103, 104] pointed out that the word *reflection* had been largely misused all these years unless, for reflection to be occurring, "*the surface of the disturbing body is larger than many square wavelengths*". Instead he proposed, following Tyndall's thought, that light was scattering rather than being reflected, from dielectric particles of diameters smaller than the light's wavelength. He was then able to show by using dimensional analysis that "*the ratio of the amplitudes of the vibrations of the scattered and incident light varies inversely as the square of the wavelength, and the intensity of the lights themselves as the inverse fourth power*" - Rayleigh's famous λ^{-4} relation. Ten years later, he was able to reach the same result by using Maxwell's electromagnetic theory which had been published in 1864 [105]. Finally, Rayleigh's main contribution to the matter concludes in 1899 when he was able to show that the sky would be blue even in the absence of any aerosol scatterers in the atmosphere, hence implying that scattering was occurring by air molecules themselves [106]. Rayleigh was awarded the Nobel Prize in Physics in 1904, not though for his contribution to the phenomenon that now bears his name, but for the discovery of argon along with William Ramsay in the

chemistry labs of University College London.

As light propagates through a medium, its intensity drops due to absorption and scattering following the equation [107]

$$I = I_0 e^{-\beta x}, \tag{3.1}$$

where β is called the *attenuation coefficient*. In order to reach his now famous λ^{-4} relation, Rayleigh related β to the refractive index of a gas n, in the relation

$$\beta = N\sigma = \frac{2k^4}{3\pi N} |n-1|^2, \tag{3.2}$$

where $k = 2\pi/\lambda$ is the wavenumber of the light, N is the gas particle number density and σ is the scattering cross-section. Through Eq. 3.2 Rayleigh essentially proved that the shorter wavelengths of the optical spectrum do experience a much larger scattering from the molecules in the atmosphere than the ones of larger wavelength, hence making the sky appear its familiar blue colour. He also provided through this equation a means to accurately estimate for the first time Avogadro's number [101]. Through his work Rayleigh also explained why light from the sky is polarised, since light scattering from a dielectric sphere is a polarisation dependent process. Although Lord Rayleigh certainly laid the stepping stone of this new field, his solution was only exact for dilute ideal gases.

Einstein approached the matter more generally in 1910, when after following Smoluchowski's proof that light scattering in homogeneous media such as gases and liquids arises from the spontaneous thermal fluctuations of their density, he related the scattered light to the refractive index fluctuations in the scattering media [108, 109, 110]. He recalculated the attenuation coefficient, now known as the Einstein-Smoluchowski formula, to be

$$\beta = \frac{1}{6\pi N} k^4 \left[\frac{(\epsilon_\mathrm{r}-1)(\epsilon_\mathrm{r}+2)}{3}\right]^2 N k_\mathrm{b} T \beta_\mathrm{T}, \tag{3.3}$$

where k_b is Boltzmann's constant, ϵ_r is the dielectric constant and $\beta_\mathrm{T} = -(1/V)(\partial V/\partial P)_T$ is the medium's isothermal compressibility with V, P and T being the gas' volume, pressure and temperature, respectively. In dilute gases where $e_\mathrm{r} = n^2 \approx 1$ and $N k_\mathrm{b} T \beta_\mathrm{T} = 1$, Eq. 3.3 reduces to Rayleigh's formula (Eq. 3.2). Following Smoluchowski's argument, Eq. 3.3 leads to scattering intensities proportional to the square of dielectric constant fluctuations $(\delta\epsilon)^2$. In gases, the refractive index depends mainly on the gas density, ρ, hence the

scattering intensity can be shown to be [107]

$$I_{\mathrm{sc}} \propto (\delta\rho)^2. \tag{3.4}$$

In summary, Rayleigh scattering is an elastic scattering process, involving scatterers of diameters much smaller than the wavelength of the illuminating photon. When referring to gases, it is often called a *coherent* process since "the motion of the molecules leads to microscopic density fluctuations that randomize the phases and cause the scattering to be incoherent in all but the forward direction. Away from the forward direction, very rapidly changing interferences occur which average to remove coherent effects and make the scattering intensity just proportional to the number of scatterers. In the forward direction, coherence is maintained since there is no momentum transfer"[111]. Its spectral lineshape would be calculated by Eq. 3.4 and its variants, but adjacent to this line peak one would have to add the symmetrical Brillouin peaks due to the bulk motion of the medium.

3.3 Brillouin scattering

In 1922, L*é*on Brillouin studied the propagation of light and x-rays through a transparent, homogeneous body, and the influence of thermal excitation on this propagation [112]. Although not explicitly referred to as such in his publication, he found that the frequency of the incident light could be Doppler shifted due to acoustic (pressure) waves in the medium. These pressure waves would form a periodic density grating inside the medium, so that when light was shone at the medium at a particular angle, a Bragg reflection condition (for light and not x-rays this time) could occur, resulting in two additional spectral lines adjacent to the central Rayleigh peak. Since these pressure waves propagate in the medium at a velocity equal to the speed of sound in the medium, the position of the peaks relative to the centre would correspond spectrally to that speed. Mandelstam independently reached the same conclusions by studying light propagation in inhomogeneous media. Although it is believed that he reached these results as early as 1918, he published them in 1926 [113].

Since the frequency/energy of the scattered photons is shifted, Brillouin scattering is an inelastic process. Let us consider an acoustic wave of wavelength Λ which propagates in a liquid or gaseous medium, whose frequency Ω and wavevector $\mathbf{q}$ are related according to $\Omega = |\mathbf{q}|\, v$, where v is its speed. This perturbation would create density fluctuations

of period Λ, which would act equivalently on the phonons in a crystal lattice. If this perturbation is illuminated by light of wavelength λ at an angle θ which satisfies the Bragg condition [114]

$$n\lambda = 2\Lambda sin\theta, \tag{3.5}$$

where n denotes the order of diffraction, then this incident light is scattered from the periodic density perturbation exactly in the way x-rays are scattered from the planes of a crystal lattice. Now, if the illuminating light encounters a counter-propagating perturbation (Fig. 3.1(a)), the photons will gain energy from the phonons. If the illuminating light confronts a co-propagating perturbation (Fig. 3.1(b)), the scattered photons will have a final energy equal to their initial value minus the one taken away from them by the perturbation. The former will result in the anti-Stokes Brillouin peak whereas the latter will give the Stokes Brillouin peak.

Brillouin scattering was demonstrated experimentally in 1930 by Gross [115] in liquids and has since been exploited in many practical applications, such as acousto-optic modulators [116], temperature and pressure sensing in optical fibres [117].

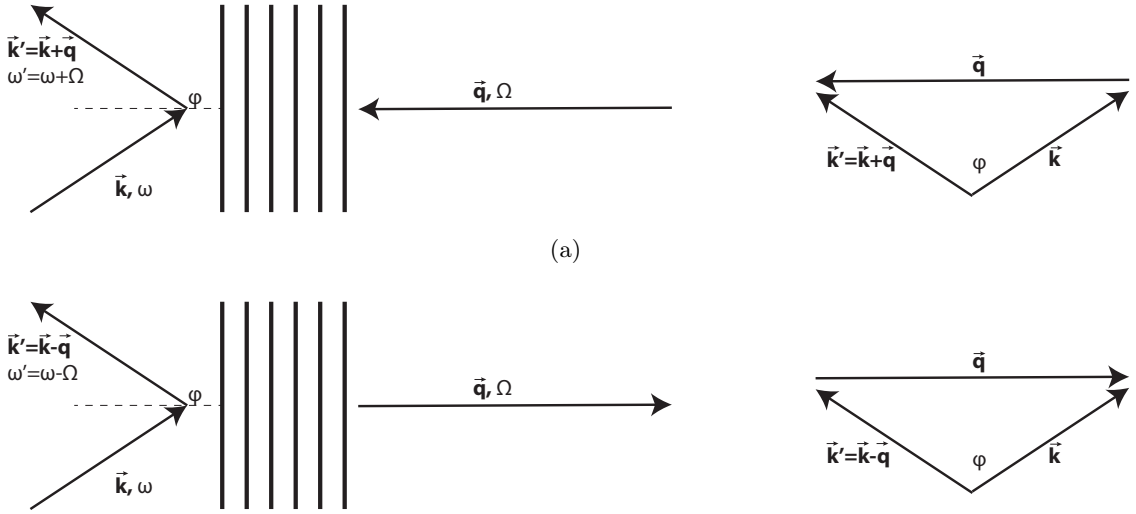

Figure 3.1: Illustration of anti-Stokes (a) and Stokes (b) Brillouin scattering. A light beam of frequency ω and wavevector $\boldsymbol{k}$ is incident at an angle ϕ fulfilling the Bragg relation, at a density perturbation of frequency Ω and wavevector $\boldsymbol{q}$. In the case when the perturbation counter-propagates to the incident light beam (a), the scattered beam will be of frequency $\omega' = \omega + \Omega$ and wavevector $\boldsymbol{k}' = \boldsymbol{k} + \boldsymbol{q}$. In the case when the perturbation co-propagates to the incident light beam (b), the scattered beam will be of frequency $\omega' = \omega - \Omega$ and wavevector $\boldsymbol{k}' = \boldsymbol{k} - \boldsymbol{q}$. The wavevectors are shown here to be of equal length for simplicity.

3.4 Rayleigh-Brillouin scattering

Because the frequency shift induced by Brillouin scattering is in general quite small compared to the optical frequencies, Rayleigh and Brillouin scattering are usually observed together, in the so-called Rayleigh-Brillouin scattering spectra. In fact, the Brillouin peaks were initially studied as extra spectral structure of the Rayleigh peak, and are still considered as such by Raman spectroscopists (who would refer to the whole triplet as "the Rayleigh peak"). Landau and Placzek showed, by only using thermodynamic arguments, that the ratio of the peaks in the Rayleigh-Brillouin spectrum is given by [118, 119]

$$\frac{I_{\mathrm{R}}}{2I_{\mathrm{B}}} = \frac{c_{\mathrm{P}} - c_{\mathrm{V}}}{c_{\mathrm{V}}} = \gamma - 1, \tag{3.6}$$

where I_{R} and I_{B} denote the integrated intensities of the Rayleigh and Brillouin peaks, respectively, while c_{P} and c_{V} are the gas' specific heat capacities under constant pressure and volume, respectively and γ is the heat capacity ratio. They also pointed out that their widths are determined by viscosity and heat conductivity, thus rendering these spectra ideal diagnostic tools for the determination of important characteristic properties of any medium, especially in the gas and liquid phases.

In order to theoretically study the Rayleigh-Brillouin line shape, there are two regimes one needs to examine: the kinetic regime and the hydrodynamic regime. These two regimes are usually distinguished via the *y-parameter* which is proportional to the ratio of the scattering wavelength to the mean free path of the particles under examination, and is defined as

$$y = \frac{N_0 k_{\mathrm{B}} T}{k \eta \nu_0} \propto \frac{\lambda}{\Lambda}, \tag{3.7}$$

where η is the dynamic viscosity, N_0 is the average number density, T is the gas' temperature, k is the light's wavevector, k_{B} is Boltzmann's constant, ν_0 is the most probable velocity of the particles, λ is the wavelength of the interference pattern formed by the incident and the scattered light, given by $\lambda = \frac{2\pi}{|\boldsymbol{k}_i - \boldsymbol{k}_s|}$, where $\boldsymbol{k}_i$ and $\boldsymbol{k}_s$ are the respective wavevectors of the incident and scattered light, and Λ is the mean free path of the particles in the periodic density perturbation [120, 49].

When $y >> 1$, then the scattering wavelength is much larger than the mean free path of the individual molecules, and the medium behaves as a continuum; this is the hydrodynamic regime. The Rayleigh-Brillouin spectra observed in this regime are comprised of

three distinct peaks: the central Rayleigh peak, which is unshifted in frequency and is due to entropy fluctuations, and two peaks symmetrically equishifted from the Rayleigh peak, which are the Brillouin peaks, due to scattering from acoustic waves. The gas density fluctuations in this regime can accurately be described by Navier-Stokes equations, as was shown by Kadanoff and Martin who first obtained an approximate theoretical solution for the Rayleigh-Brillouin line shape [121].

Things are more complex for $0 < y < 5$ when "*the 3 components flow into one another and the structure of the line ultimately attains the Gaussian form, with angle-dependent width, as required by the Doppler effect*" [118, 101]: this is the kinetic regime. As a general approach, one simply needs to derive the gas density perturbation by solving Boltzmann's kinetic equation for gas particles in this regime and then obtain the Rayleigh-Brillouin scattering spectrum from the density perturbation power spectrum. The difficulty in this approach lies with the difficulty in solving the collision integral in Boltzmann's equation, which is given by [107]

$$-\left[\frac{\delta f}{\delta t}\right]_{\text{coll}} = \int\int |\boldsymbol{v} - \boldsymbol{v_1}|\, \sigma(f_1' f' - f_1 f) d\Omega d^3 u_1, \tag{3.8}$$

where $f_1 = f(\boldsymbol{v_1}, \boldsymbol{r}, t)$, $\boldsymbol{v}$ and $\boldsymbol{v_1}$ are the respective final and initial particle velocities, f' and f_1' are the distribution functions after the collision, σ is the collision cross section and $\sigma d\Omega$ is proportional to the number of particles scattered into the solid angle element $d\Omega$ around Ω. This is not a big issue in the collisionless limit of the kinetic regime, i.e. when the scattering wavelength is much less than the mean free path and $y \to 0$. Since there is no correlation in the motion of the particles, one simply needs to sum up the intensity of light scattered by each individual particle for each frequency, to obtain a Gaussian curve (as predicted by Landau and Placzek) corresponding to the Maxwellian velocity distribution of the gas particles [107].

In the collision limit of the kinetic regime, Yip and Nelkin [120] were among the firsts who tried to obtain a theoretical solution for the Rayleigh-Brillouin scattering spectrum, and also suggested that it could be used as a test for Boltzmann's equation [122]. They identified that the power spectrum $I(\mathbf{k}, \omega)$ of the scattered light is related to the time-displaced, density-density correlation function $G(r, t)$ by [107]

$$I(\mathbf{k}, \omega) \propto \int_{-\infty}^{+\infty} dt \int d^3 r G(r, t) exp[i(\mathbf{k}r - \omega t)]. \tag{3.9}$$

In order to obtain the $G(r,t)$ term and consequently the scattered intensity spectrum, they solved Boltzmann's equation to which they introduced a δ-function perturbation on the gas density, using the Bhatnagar-Gross-Krook's (BGK) approximation [123]. Their model was put to the test by Greytak and Benedek [124] who measured the light scattered from Ar, Xe, N_2, CO_2 and CH_4, for a range of y-parameter values. This lead to a correction to their initial model [125, 126] in order to better match the experimental data, which was then indepedently verified by Clark [127].

Although Yip and Nelkin's model gives good results for atomic gases, such as Ar and Xe, this doesn't prove to be the case for molecular gases, such as CO_2, where at room temperature their translational energy can be coupled with their rotational and vibrational energies. To address the case of molecular gases, a model was proposed by Boley *et al.* [128] and Tenti *et al.* [129], based on the Wang-Chang-Uhlenbeck equation [130]. The 6-moment model proposed by Tenti *et al.*, is generally called the $s6$ model, and is considered to better match the experimentally obtained spectra. It can also easily be used in the case of atomic gases, simply by suppressing the internal degrees of freedom.

Concluding this overview on Rayleigh-Brillouin scattering, it is worthwhile mentioning its applications in probing the speed of sound [131, 132], gas temperature and vibrational and relaxational rates [133, 134]. For a more detailed review on the history of Rayleigh scattering we refer to [101, 135] and Fabilinskii [136], and for a more detailed analysis on theoretical Rayleigh-Brillouin models, to [107].

3.5 The physics of coherent Rayleigh-Brillouin scattering

Coherent Rayleigh-Brillouin scattering (CRBS) is a non-resonant, $\chi^{(3)}$ four-wave mixing process, where two pump beams interfere to create a periodic density grating from which a third probe beam, incident at an angle fulfilling the Bragg condition, is scattered forming a fourth, signal beam, as shown in Fig. 3.2. Measuring the intensity of the signal beam with respect to the grating's velocity yields the coherent Rayleigh-Brillouin spectra.

3.5.1 Electrostriction

A periodic density variation can be caused by the dipole force induced by the interference of two beams. This dipole moment interacts with the field that created it to produce an optical potential, the gradient of which has sufficient force to control the species' motion.

A ground state molecule in an optical field that is far red-detuned from any molecular resonances experiences a negative Stark shift [137]. This time averaged potential in a single laser beam field is given by [119, 138]

$$U = -\frac{1}{4}\alpha_{\text{eff}}E^2, \tag{3.10}$$

where α_{eff} is the effective polarisability of the molecule and E is the amplitude of the electric field. For molecular species, the effective polarisability is given by [139]

$$\alpha_{\text{eff}} = [(\alpha_{\parallel} - \alpha_{\perp})cos^2\theta + \alpha_{\perp}], \tag{3.11}$$

where $\alpha_{\parallel}$ and $\alpha_{\perp}$ are the polarisability components parallel and perpendicular to the molecular axis and θ is the angle between the molecular axis and the laser polarization. The resultant force experienced by a molecule in an optical potential is

$$F = -\nabla U = \frac{1}{2}\epsilon_0\alpha_{\text{eff}}\nabla(E^2). \tag{3.12}$$

The sign of the force is determined ultimately by the sign of α_{eff}. Molecules with a positive α_{eff} feel an attraction towards high electric field strengths, hence they are called "high field seekers". If α_{eff} is negative, molecules are repelled from high electric field strengths, hence labelled "low field seekers". In very large fields, all molecular states become high-field seeking [63] while the absolute ground-state of any molecule is always high-field seeking [140]. The tendency of polarizable molecules to move towards regions of high optical electric field intensities is referred to as *electrostriction* or the *dipole force* [119].

From Eq. 3.12 it is apparent that the force experienced by a molecule is proportional

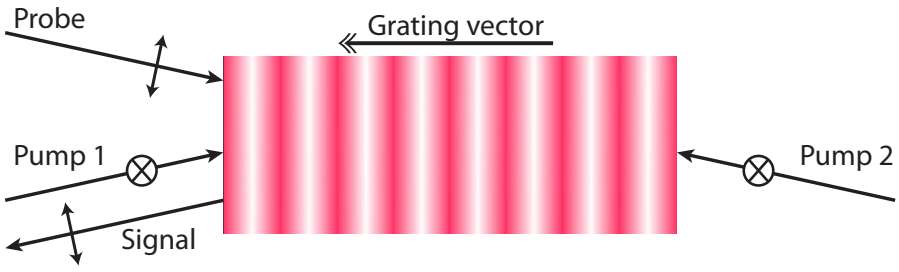

Figure 3.2: Schematic of the most common type of CRBS. Two almost counter-propagating beams cross to form an optical lattice while a third, orthogonally polarised probe beam is Bragg scattered from the lattice to form the signal beam.

to the intensity gradient of the field, such as in a tightly focussed laser beam [141]. By tailoring the field's intensity gradient we may maximize the force acting on the molecules in this field. Steeper intensity gradients can be created by interfering two laser beams in a nearly counter-propagating geometry. The resultant interference pattern, when interacting with a polarisable molecule, creates a periodic potential called an *optical lattice*.

We now consider two almost counterpropagating optical fields, ϵ_1 and ϵ_2, that form the optical lattice

$$\epsilon_1 = E_1(r,t)\sin(k_1 r - \omega_1(t)t), \tag{3.13}$$

$$\epsilon_2 = E_2(r,t)\sin(k_2 r - \omega_2(t)t), \tag{3.14}$$

where E_1 and E_2 are the amplitudes of the electric fields, k_1 and k_2 are their respective wavevectors and $\omega_{1,2}(t)$ are the respective instantaneous frequencies of each beam at a time t. For optical fields far red detuned from any resonances in the molecular species, we can safely make the assumption that any interaction of the molecules with the fields are only due to the static polarisability of the species. For two fields ϵ_1 and ϵ_2 interacting with a molecule with polarisability α_{eff}, the optical lattice potential can be written as

$$U(r,t) = -\frac{\alpha_{\text{eff}}E^2}{2}\cos^2[(k_1 - k_2)r - (\omega_2(t) - \omega_1(t))t], \tag{3.15}$$

where $E^2 = (E_1 + E_2)^2$.

Assuming near counter-propagation of the lattice beams, we can write the resultant one dimensional optical potential as

$$U(x,t) = -\frac{\alpha_{\text{eff}}E^2}{2}\cos^2[(1/2)(qx - \Delta\omega(t)t)], \tag{3.16}$$

where q is the wavevector of the lattice given by $q = (\frac{2\pi}{\lambda})\sin\phi$, λ is the wavelength of the lattice beams, ϕ is the half-angle between the two lattice beams, and $\Delta\omega(t)$ is the frequency difference between the beams.

The force on a molecule in a potential as the one shown on Eq. 3.16 would then be given by

$$F = -\nabla U = -\frac{\alpha_{\text{eff}}qE^2}{2}\sin[qx - \Delta\omega(t)t]. \tag{3.17}$$

Considering that the relation between laser intensity and the amplitude of the electric field

is given by

$$I(t) = \frac{c_0 \epsilon_0 n}{2} E^2, \tag{3.18}$$

where c_0 is the vacuum velocity of light, ϵ_0 is the vacuum permittivity and n is the refractive index of the propagation medium, Eq. 3.17 can be rewritten in terms of the measurable lattice intensities $I_{1,2}(t)$, as

$$F = -\frac{\alpha_{\text{eff}} q}{c_0 \epsilon_0 n} \sqrt{I_1(t) I_2(t)} \sin[qx - \Delta\omega(t)t]. \tag{3.19}$$

3.5.2 Four-Wave Mixing & Bragg scattering

Four-Wave Mixing (FWM) describes a family of $\chi^{(3)}$ non-linear processes, which involve the change in the refractive index of a medium [10], induced by optical fields. Bragg scattering is perhaps the simplest of the FWM processes. The name is given by analogy to the diffraction of x-rays from the atomic planes in a crystal. Bragg scattering is exploited most commonly in acousto-optic devices, called acousto-optic modulators (AOMs), where an RF acoustic wave forms a refractive index modulation inside the acousto-optic crystal, which consequently causes an incident light wave to diffract. This refractive index modulation arises from the photoelastic effect.

Bragg scattering can also be achieved by optical means. If two laser beams (called the *pumps*) with a relative frequency difference, interfere to produce a moving optical lattice in some medium (e.g. air) then, due to electrostriction, a moving periodic density (and thus refractive index) modulation is created in the interaction region of the two beams. If a third beam (called the *probe*) is incident on the grating at an angle which fulfils the Bragg condition, significant light can be scattered by the grating, creating a fourth coherent beam (called the *signal*). The Bragg condition is given by

$$d = \frac{\lambda}{2 \sin\theta}, \tag{3.20}$$

where d is the grating spacing, λ is the probe wavelength and θ the crossing angle. The mathematical treatment of the process is the same as in the case of an AOM, where the period of the acoustic wave is replaced by the periodic refractive index perturbation with wavevector $\mathbf{q}$, caused by a modulation in the refractive index n of the medium, induced by the dipole force. Hence, it can be treated theoretically by considering the space and time

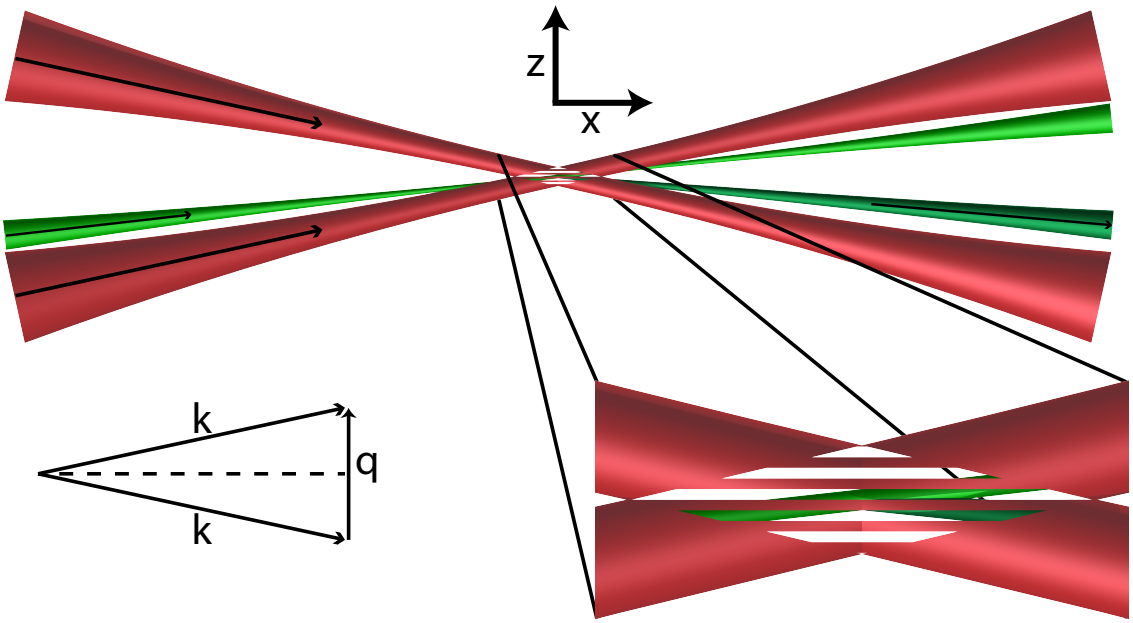

Figure 3.3: Schematic of a typical geometry used in CRBS. Two almost copropagating beams cross to form an optical lattice while a third, orthogonally polarised probe beam is Bragg scattered from the lattice to form the signal beam.

varying change in the dielectric constant $\Delta\tilde{\epsilon}$[1] induced by the density variation $\Delta\tilde{\rho}$, where $n = \sqrt{\epsilon_r}$. It is usually adequate to assume that $\Delta\tilde{\epsilon}$ scales linearly with $\Delta\tilde{\rho}$, so that

$$\Delta\tilde{\epsilon} = \frac{\partial\epsilon}{\partial\rho}\Delta\tilde{\rho} = \gamma_\epsilon \frac{\Delta\tilde{\rho}}{\rho_0}, \tag{3.21}$$

where ρ_0 denotes the mean density of the medium and γ_ϵ denotes the electrostrictive constant defined by $\gamma_\epsilon = (\rho\frac{\partial\epsilon}{\partial\rho})_{\rho=\rho_0}$.

In the geometry depicted in Fig. 3.3, we consider the interaction of the probe field of amplitude A_p

$$E_\mathrm{p} = A_\mathrm{p} e^{i(\boldsymbol{k}_\mathrm{p}\boldsymbol{r} - \omega_\mathrm{p} t)} + \text{c.c.}, \tag{3.22}$$

with the moving lattice of wavevector $\mathbf{q}$, which produces the diffracted signal wave of amplitude A_s, given by

$$E_\mathrm{s} = A_\mathrm{s} e^{i(\boldsymbol{k}_\mathrm{s}\boldsymbol{r} - \omega_\mathrm{s} t)} + \text{c.c.}, \tag{3.23}$$

with $\omega_\mathrm{s} = \omega_\mathrm{p} + \Omega$, where Ω is the frequency of the moving lattice. We assume the interaction to be nearly Bragg matched (i.e. phase-matched), so that

$$\boldsymbol{k}_\mathrm{s} \approx \boldsymbol{k}_\mathrm{p} + \boldsymbol{q}. \tag{3.24}$$

[1]Following Boyd's notation [119], the tilde is used to denote a quantity that varies rapidly in time

The variation of the dielectric constant induced by the lattice is represented by

$$\Delta\tilde{\epsilon} = \Delta\epsilon e^{i(\boldsymbol{q}\boldsymbol{r}-\Omega t)}, \tag{3.25}$$

where the complex amplitude $\Delta\epsilon$ is given by $\Delta\epsilon = \gamma_\epsilon \frac{\Delta\rho}{\Delta\rho_0}$. The total optical field $\tilde{E} = \tilde{E}_\mathrm{p} + \tilde{E}_\mathrm{s}$ is required to satisfy the wave equation

$$\nabla^2\tilde{E} - \frac{n^2 + \Delta\tilde{\epsilon}}{c^2}\frac{\partial^2\tilde{E}}{\partial t^2} = 0, \tag{3.26}$$

where n denotes the refractive index of the medium in the absence of any field. Since according to Eq. 3.25, $\Delta\tilde{\epsilon}$ oscillates at a frequency Ω, it couples the optical waves of frequencies ω_p and $\omega_\mathrm{s} = \omega_\mathrm{p} + \Omega$. We first consider the portion of Eq. 3.26 that oscillates at frequency ω_p. This part is given by

$$\frac{\partial^2 A_\mathrm{p}}{\partial x^2} + \frac{\partial^2 A_\mathrm{p}}{\partial z^2} + 2ik_\mathrm{px}\frac{\partial A_\mathrm{p}}{\partial x} + 2ik_\mathrm{pz}\frac{\partial A_\mathrm{p}}{\partial z} - \\ - (k_\mathrm{px}^2 + k_\mathrm{pz}^2)A_\mathrm{p} + \frac{n^2\omega_p^2}{c^2}A_\mathrm{p} + \frac{\omega_\mathrm{s}^2}{c^2}A_\mathrm{s}^2\Delta\epsilon^* e^{i(\boldsymbol{k}_\mathrm{s}-\boldsymbol{k}_\mathrm{p}-\boldsymbol{q})\boldsymbol{r}} = 0 \tag{3.27}$$

where $\Delta\epsilon^*$ is the complex conjugate of $\Delta\epsilon$. The ω_s and A_s terms in Eq. 3.27 have appeared by substitution from the fact that $\omega_\mathrm{s} = \omega_\mathrm{p} + \Omega$ and from Eqns. 3.23 and 3.24. Also, the terms oscillating at $2\omega_\mathrm{s}$, $2\omega_\mathrm{p}$, $2k_\mathrm{s}$ and $2k_\mathrm{p}$ have been neglected. This equation can be simplified by introducing the slowly varying amplitude approximation, which entails ignoring the second-order derivatives in Eq. 3.27. We also note that A_p depends only on z and not on x (see Fig. 3.3), since the interaction is invariant to a translation in the x direction ($x >>> z$), and so we set $\partial A_\mathrm{p}/\partial x$ equal to 0. Furthermore, we note that $(k_\mathrm{px}^2 + k_\mathrm{pz}^2) = \frac{n^2\omega_\mathrm{p}^2}{c^2}$. Finally, the propagation vector mismatch $\boldsymbol{k}_\mathrm{s} - \boldsymbol{k}_\mathrm{p} - \boldsymbol{q} \equiv -\Delta\boldsymbol{k}$ can have a non-zero component only in the z direction, because in the geometry we are considering, we are assuming it to have infinite extent in the x direction, and the x component of the $\boldsymbol{k}$ wavevector must vanish, hence $\boldsymbol{k}_\mathrm{s} - \boldsymbol{k}_\mathrm{p} - \boldsymbol{q} \equiv -\Delta\boldsymbol{k}_\mathrm{z}$.

Given these assumptions, Eq. 3.27 can now be simplified and written as

$$\frac{dA_\mathrm{p}}{dz} = \frac{i\omega_\mathrm{s}^2\Delta\epsilon^*}{2k_\mathrm{pz}c^2}A_\mathrm{s}e^{-i\Delta k_\mathrm{z}}. \tag{3.28}$$

By an analogous derivation, we find that the portion of the wave Eq. 3.26 that describes

a wave oscillating at frequency ω_s is given by

$$\frac{dA_s}{dz} = \frac{i\omega_p^2 \Delta\epsilon^*}{2k_{sz}c^2} A_p e^{-i\Delta k_z}. \tag{3.29}$$

Finally, we note that since $\omega_p \approx \omega_s = \omega$ and $k_{pz} \approx k_{sz} \equiv k_z$, the coupled Eqns. 3.28 and 3.29 can be written as

$$\frac{dA_p}{dz} = i\kappa A_s e^{-i\Delta k_z}, \tag{3.30a}$$

$$\frac{dA_s}{dz} = i\kappa^* A_p e^{-i\Delta k_z}, \tag{3.30b}$$

where we have introduced the coupling constant

$$\kappa = \frac{\omega^2 \Delta\epsilon^*}{2k_z c^2}. \tag{3.31}$$

The solution to the coupled amplitude equations 3.30 is particularly simple for the case in which E_p is incident at the Bragg angle. In this case, the interaction is perfectly phase-matched so that $\Delta k = 0$, and thus Eqns. 3.30a and 3.30b reduce to the set

$$\frac{dA_p}{dz} = i\kappa A_s, \tag{3.32a}$$

$$\frac{dA_s}{dz} = i\kappa^* A_p. \tag{3.32b}$$

The dependence of A_p and A_s on κ as shown in Eqns. 3.32a and 3.32b, reveal the strong dependence on the dielectric constant perturbation along the interaction path. If one wishes to get a more general solution to the Bragg scattering signal that could be observed from such perturbations, then one should take into account the changes to the density distribution within the medium due to the light fields interacting with it, instead of the simplified dielectric constant perturbation presented in Eq. 3.25.

When operating far from resonance, the refractive index (and hence the dielectric constant) can be related to the polarisability of the gas particles by [142]

$$n = \sqrt{1 + \frac{N\alpha}{\epsilon_0}} \approx n_0 + \Delta n(z,t), \tag{3.33}$$

where α is the static polarisability of each molecule and N is the number of molecules. Accordingly one can also use the α_{eff} for a more accurate solution. The perturbation of

the refractive index induced by the field is related to the change in density by

$$\Delta n(z,t) = \frac{\Delta N(z,t)\alpha}{2\epsilon_0}. \tag{3.34}$$

The gas density perturbation $\Delta N(z,t)$ can be found from the velocity distribution function as

$$\Delta N(z,t) = \int_{-\infty}^{+\infty} [f_0(z,\nu,t) - f_0(\nu,T)]d\nu, N_0 = \int_{-\infty}^{+\infty} f_0 d\nu, \tag{3.35}$$

where $f_0(\nu,T)$ is the local Maxwellian velocity distribution function and $f_0(z,\nu,t)$ is derived by the solution of the 1D Boltzmann equation along the lattice direction, z, given by

$$\frac{\partial f}{\partial t} + \nu\frac{\partial f}{\partial z} + \frac{F(z,t)}{m}\frac{\partial f}{\partial \nu} = \frac{f - f_0}{\tau_c}. \tag{3.36}$$

The term $\frac{f-f_0}{\tau_c}$ is the Bhatnagar-Gross-Krook (BGK) approximation[123], which assumes that over a relaxation time τ_c, the distribution function relaxes to the equilibrium value f_0. Of course, $F(z,t)$ is the force along the lattice, as this is given by Eq. 3.19. To conclude, in order for one to gain an accurate solution for the obtained signal through a Bragg scattering process, one has to solve the Eqns. 3.36 through 3.34 and then substitute the result for the perturbation in the refractive index along the interaction region into the wave Eq. 3.26.

3.6 The CRBS spectral profile

In summary, CRBS is the Bragg scattering of a probe beam from an optical lattice created in a medium due to electrostriction by two interfering pump beams. The intensity of the scattered signal beam with respect to the frequency difference of the two beams, and hence the velocity of the lattice, forms the CRBS spectral lineshape.

As is apparent from Eq. 3.35 this lineshape would be a function of the particle density distribution along the lattice, represented by the term $f_0(z,\nu,t)$. When working in the $0 < y < 5$ kinetic regime, the gas density perturbation can be obtained by solving Boltzman's kinetic equation, whereas in the $y > 5$ hydrodynamic regime, the gas density distribution can be found by solving the coupled Navier-Stokes equations, as the gas can then be treated as a continuum.

3.6.1 Brief history of CRBS

Although as mentioned earlier, spontaneous and stimulated flavours of Rayleigh and Brillouin scattering are well known and have been experimentally observed for more than 50 years, however their coherent versions are relatively new. It is interesting to note here that She *et al* had proposed the feasibility of CRBS in the eighties [143, 144] but they did not demonstrate it experimentally. Historically, coherent Rayleigh scattering (CRS) was the first such process to be experimentally demonstrated by Barker and Grinstead in 2000 [145].The full CRBS spectrum, where both Rayleigh and Brillouin features could be observed, was firstly reported by Pan *et al* in 2002 [49] where a theoretical model was also developed to simulate the CRBS signal, followed by more studies by the same group [146, 147, 148]. These two initial reports in CRS and CRBS ignited a range of studies on the matter, both theoretical [149, 139] and experimental [150, 151, 152, 153, 154, 155, 156, 157, 158], to cite just a few.

Although these were the first demonstrations of CRS and CRBS in any phase of matter, because of the limitations posed by the nature of Rayleigh scattering, coherent Brillouin scattering had been well studied and exploited in the liquid [55, 56, 57] and solid [58, 59, 60] phases and even used for the characterisation of biological specimens [159, 160]. In the liquid and solid phases, the method uses a pump beam to generate acoustic (pressure) waves due to thermalisation, which would then propagate along the surface of the medium and a second probe beam, incident at the Bragg angle, is used to map them out, revealing information about shear and bulk viscosity and even internal structure. This method is so successful that it has even been used in non-destructive inspection of Japanese tunnels, replacing the traditional approach of the workers inspecting the sites with the use of a hammer! [161]

In gases though, because of the relatively more complex setup needed to probe such effects, it hasn't been until the work performed for the purposes of this thesis that coherent Brillouin scattering (CBS) had been demonstrated in the gas phase [81]. The exact method used to achieve this, as well as detailed analysis will follow in the next chapter. In summary, CRS and CBS can be thought of as being subsets of CRBS which are observed at extreme values of the y-parameter (Fig. 3.4).

CRBS has definitely showed over the years its feasibility in atomic and molecular gas diagnostics as well as nanoparticle detection [162]. However, the acquisition time for a

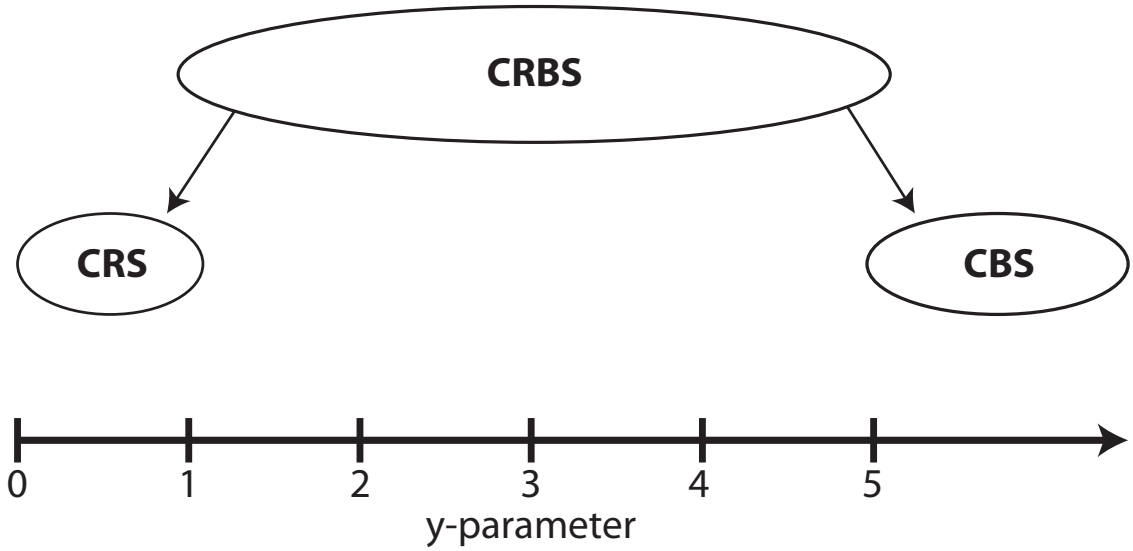

Figure 3.4: Schematic of the CRBS regimes. For $0 < y < 1$ coherent Rayleigh scattering (CRS) is oberved while for $y > 5$ coherent Brillouin scattering is observed. In the intermediate regime, we get the spectrum corresponding to coherent Rayleigh-Brillouin scattering.

complete CRBS spectrum to be obtained experimentally is long, in the order of an hour, requiring high levels of experimental stability. In order to overcome this limiting factor, we developed a technique which can be used in order to obtain complete CRBS spectra in durations equal to that of the laser pulse that is used. In the system we developed this translates to just 140 ns for a full CRBS spectrum to be acquired. The method will be presented in Chapter 5.

3.7 Comparison to other techniques

3.7.1 Laser Induced Thermal Acoustics (LITA)

LITA was initially proposed and investigated by Cummings as part of his PhD at CalTECH [163, 164]. The experimental setup consists of two nearly co-propagating beams which have got a fixed frequency difference and which interfere in the medium under investigation (air and mixtures with NO_2 in their case). The geometry used means this work is in the hydrodynamic regime and allows for efficient pressure wave propagation. Apart from the created electrostrictive gratings (called *phonons*), a second grating due to absorption and subsequent thermalisation is created in the medium as well (called *thermon*), which copropagates with the phonons. Both induced gratings would have the same wavelength, equal to that of the optical lattice. Cummings found that the thermalisation process

was much more effective in heating the medium than the electrostrictive one and thus in acoustic wave creation.

A third, CW probe beam was shone at the interaction region of the two pump beams, incident at the Bragg angle. The intensity of the Bragg scattered light would oscillate in time with a frequency equal to that of the acoustic wave, whereas its magnitude would decrease at the rate of heat diffusion in the medium. Should the dominant mechanism be the electrostrictive process, the decay rate would be determined by acoustic damping in the medium.

LITA has proven to be a successful technique in determining speed of sound and thus temperature in flow environments [165, 166, 167]. Physically, the signal observed in LITA is not different to that measured by CRBS. A main difference between the two lies in the fact that LITA operates in the time domain, as what is measured is the decay rate of the induced acoustic wave with respect to time. In CRBS, we operate in the frequency domain and what is measured is the intensity of the Bragg scattered signal with respect to the frequency of the electrostrictive grating. Another difference is that in order for LITA to be successful, a small crossing angle is required between the two pump beams, so that the induced grating would have a much larger wavelength than the mean free path of the scatterers in the medium. This prerequisite though, limits the technique in being able to detect Rayleigh scattering related quantities. On the other hand, one of the main advantages of the technique lies in the fact that since it's using a CW beam as the probe, single shot measurements can easily be obtained.

3.7.2 Laser Induced Gratings (LIGs)

LIGs (also met in the literature under the name *Laser Induced Electrostrictive Gratings*[168, 169])is similar to LITA in some ways. In LIGs again two pump beams cross creating an optical lattice in the medium, and a third beam is Bragg scattered from them to provide the signal beam. Although both LITA and LIGs look for a signal *after* the propagation of the two pumps, the difference between them lies in the fact that in LIGs it's the electrostrictive grating that provides the required density perturbation in the medium and not one due to thermalisation [170, 171].

Since it does not rely on the bulk motion of the scattering medium to obtain a signal, it can be seen both in co-propagating as well as counter-propagating geometries, and al-

though in its initial implementations a pulsed probe was used, it has been shown that a CW beam can be used as well, thus allowing for single shot LIGs measurements. LIGs has been successfully used over the years in temperature and velocity measurements in flow environments in the gas phase [172, 173] and even for underwater temperature measurements [174].

Chapter 4

Coherent Brillouin scattering

4.1 Introduction

As an initial performance test of the laser system presented in Chapter 2, a coherent Brillouin scattering (CBS) experiment in the high $y \approx 27$ parameter regime was conducted. Rather than following a geometry where the pump laser beams counter-propagate as in most CRBS experiments to date, this experiment used a co-propagating geometry for the two pump beams forming the lattice. To our knowledge this is the first CRBS experiment conducted in the pure hydrodynamic regime in a gas and also revealed additional spectral features, never seen before in CRBS in the gas phase. In this chapter I present the details of the experimental setup used and discuss the results obtained.

4.2 Experimental setup

The experimental setup used the laser system presented in Chapter 2 to deliver the high energy pump beams to create a controllable, constant frequency grating in the gaseous medium. The infrared (IR) pump laser pulses used were of 140 ns duration, and 200 mJ energy per pulse, each. The probe beam was provided by a laser which delivered 532 nm pulses of $\approx$ 10 ns duration and energy of $\approx$ 300 mJ per pulse[1]. The respective temporal profiles of the pumps and the probe, are shown in Fig. 4.1.

Since the pumps and the probe had considerably different pulse durations, we were able to scan the evolution of the resulting CBS spectral profile by changing the temporal position of the probe with respect to the pump. Experimentally this was achieved by

[1]Precision II by Continuum operating at 10 Hz

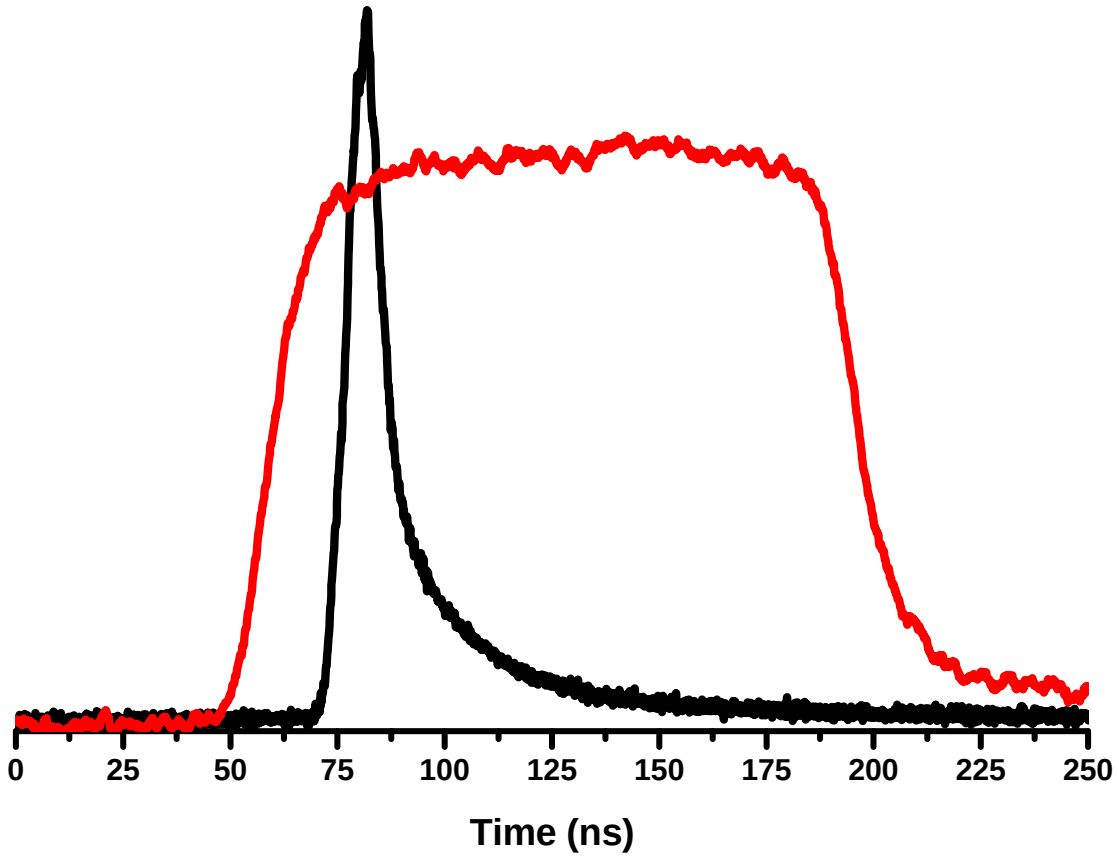

Figure 4.1: Temporal profiles of the pump (red) and probe (black) that were used in the CBS experiment. The y-axis represents arbitrary intensity.

controlling the firing of the probe through a digital delay generator[2], which was itself triggered by the capacitor banks of the custom IR laser system.

4.2.1 Geometry and alignment considerations

The geometry used in the CBS experiment is shown in Fig. 4.2(a). The angles of the co-propagating geometry that was used were largely determined by the optics we would use, as well as the wavelengths of the pump and probe lasers. All three beams were focused in the centre of a custom made glass cell (Fig. 4.2(b)) by the same 2" diameter, 50 cm focal length lens, AR coated for both 532 nm and 1064 nm. By using a long focal length lens we eliminate the risk of burning the AR coated windows of the glass cell.

Given the physical diameter of the lens and the fact that ideally we want the whole extent of the IR beams to be used in the grating formation (i.e. without clipping on the lens edges), a half angle of $\phi = 2.5^o$ for the pumps was used.

[2]DG-535 Stanford Research Systems

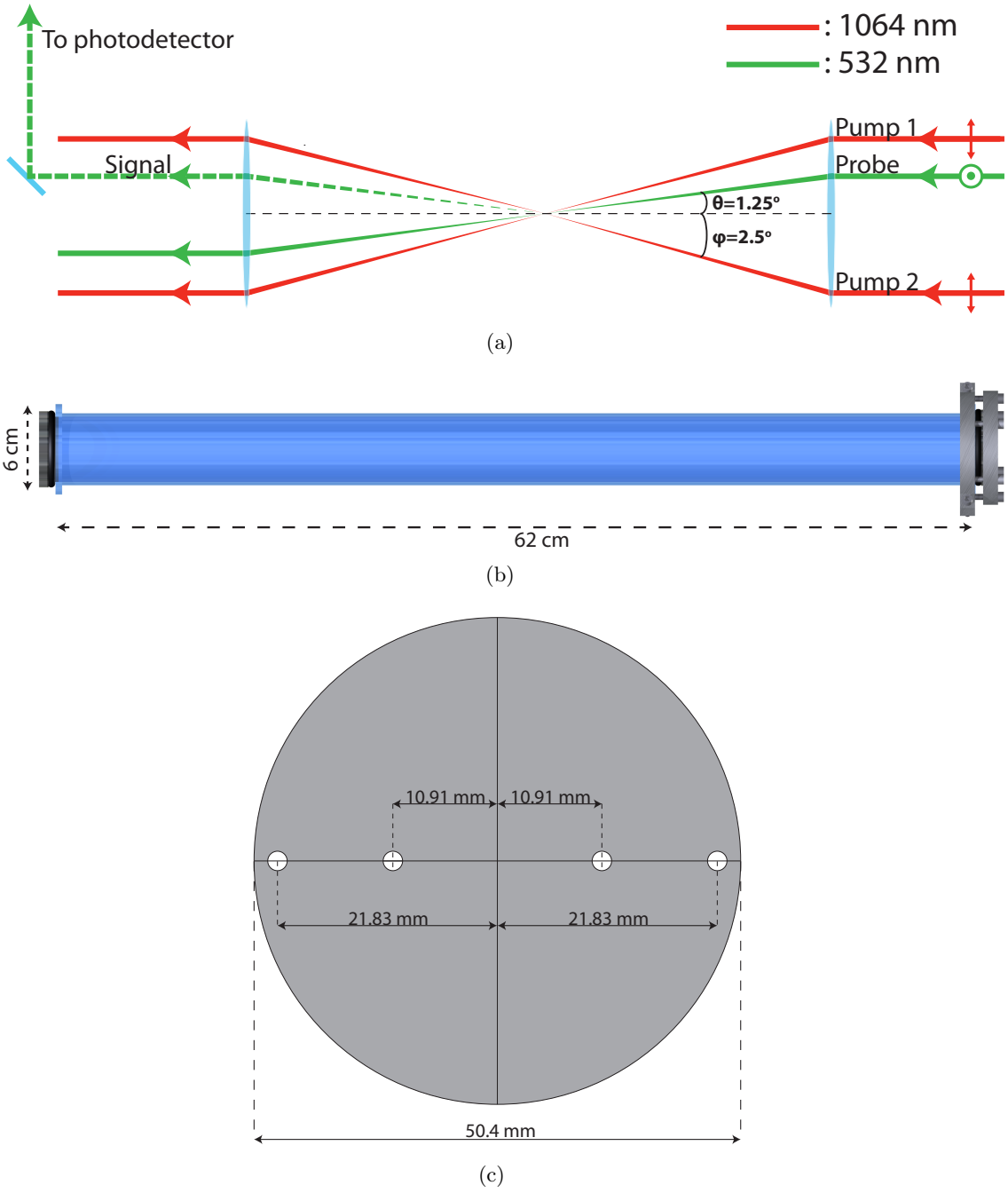

Figure 4.2: (a) Schematic showing the geometry followed in the CBS experiment. In red are shown the two IR beams which create the lattice whereas in solid green is the pump beam. The dashed green beam represents the resulting signal beam. (b) A render of the custom made glass cell that was used in the CBS experiment. On the right hand side are also shown the custom made clamps for the windows. These clamps are not shown on the left hand side to reveal the custom made O-ring holder and the optical window. (c) Drawing of the masks that were used to facilitate alignment.

Using this value in Bragg's formula yields a grating spacing of

$$\lambda_{\mathrm{g}} = \frac{\lambda_{\mathrm{pump}}}{2\sin(\phi)} \approx 12.2\mu\mathrm{m}. \tag{4.1}$$

In order to find the angle at which the probe has to be incident on the induced electrostrictive grating, we need to solve the same formula with respect to the probe half angle θ, where the values for λ_{probe} and λ_g are 532 nm and 12.2 μm respectively. By doing so, we find a value of $\theta = 1.25^o$ for the probe beam's incident angle.

Before entering the interaction region the probe beam is orthogonally polarised in order to avoid interference with the two pump beams, as shown in Fig. 4.2(a). Masks as in Fig. 4.2(c) were fabricated to aid with alignment. These were attached on the lens mounts of both the input and output lenses. This aided us in getting an initial rough alignment of the beams. Part of the probe was separated and aligned to the optical path where the signal beam was expected, in order to align a fast photodiode [3] to collect the signal ($4-5$ meters away from the interaction region in order to eliminate the background light). The rest of the beams were blocked after the output lens.

After this initial rough alignment, a CCD camera chip[4] was mounted on a post and inserted through the output side of the cell. While doing this, we maintained the optical window on the input side of the cell, so that we accommodate for the divergence induced by the window. Using the camera allowed us to accurately align the three beams, but was also useful in determining the physical size of the interaction region, simply by measuring the beam sizes at the focal spot. We need to note at this point that of course the focal spots of the IR and the 532 nm beams would not be spatially coincident, since they are focussed by the same lens. We chose to align the three beams at the point where the two pump beams would have their focus. If the coarse alignment was carefully performed, both IR beams would be very close to the desired position and only a fine adjustment would be needed thereafter. Interestingly, when there was no voltage applied to the EOM in the microchip laser, i.e. there was no frequency difference between the two pump beams, the interference pattern could be observed on the camera (Fig. 4.3). We would then adjust the beams at the point where we could see the maximum interference contrast. To confirm that the observed interference on the camera was indeed due to the interference of the two beams and not due an artefact or any thin film on the camera's CCD chip, we applied a voltage on the EOM and could immediately observe the movement of the interference pattern on the screen. We measured the interaction region to have an e^{-1} length of 96 μm, which yields an intensity for each pulse of $(144 \pm 25) \times 10^{12}$ Wm^{-2}, whereas the intensity

[3] DET210 by Thorlabs
[4] DCU223 CCD by Thorlabs

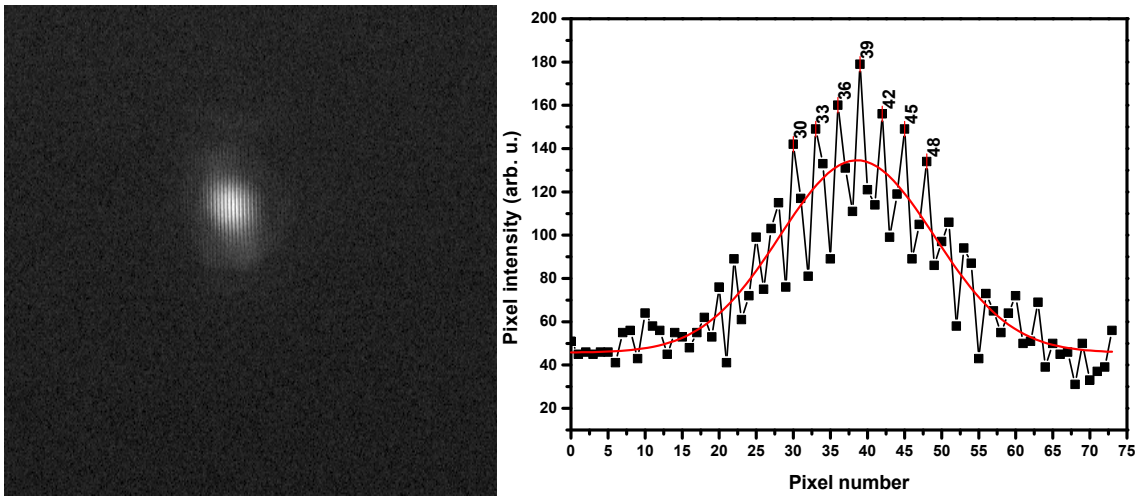

Figure 4.3: The interference of the two IR beams as was recorded by the CCD camera (left). The fact that we could observe this interference pattern was due to the co-propagating regime we were operating at, which produced gratings (wavelength of 12.2 μm) larger that the size of the individual pixel size of the CCD (4.35 μm according to the manufacturer). By analysing the intensity of individual pixels across the interference pattern (right), the "distance" between the lattice sites was determined to be three pixels which is 13.05 μm, a value very close to the calculated one. By fitting a Gaussian (in red) through the interference pattern, we can extract information about the length of the interaction region.

of the probe was $(30 \pm 5) \times 10^{12}$ Wm^{-2}.

Once the IR focal spot had been found, the probe beam was fine-tuned to be coincident with the interference pattern. Once this alignment procedure was performed, the CCD camera was removed and the cell was sealed up and pumped out. Measurements were performed in purified air at a pressure of 1000 mbar, which entered the cell through a filter[5].

4.2.2 Frequency considerations

Although the laser system had previously showed sinusoidal chirping capabilities [95, 62], for this experiment only constant frequency differences would be needed. This means that a DC voltage needed to be applied to the intracavity EOM crystal rather than a sinusoidal or ramped waveform. The induced constant frequency difference was constantly monitored by heterodyning portions of the two beams on a fast InGaAs photodiode[6], as shown in Fig. 4.4.

The fact that the frequency difference was constant (Fig. 4.5 top) meant that it was easy to measure. This task can be performed by the oscilloscope itself, or via an external

[5]810514001 0.5 μm by Swagelock
[6]G6854-01 by Hamamatsu Photonics

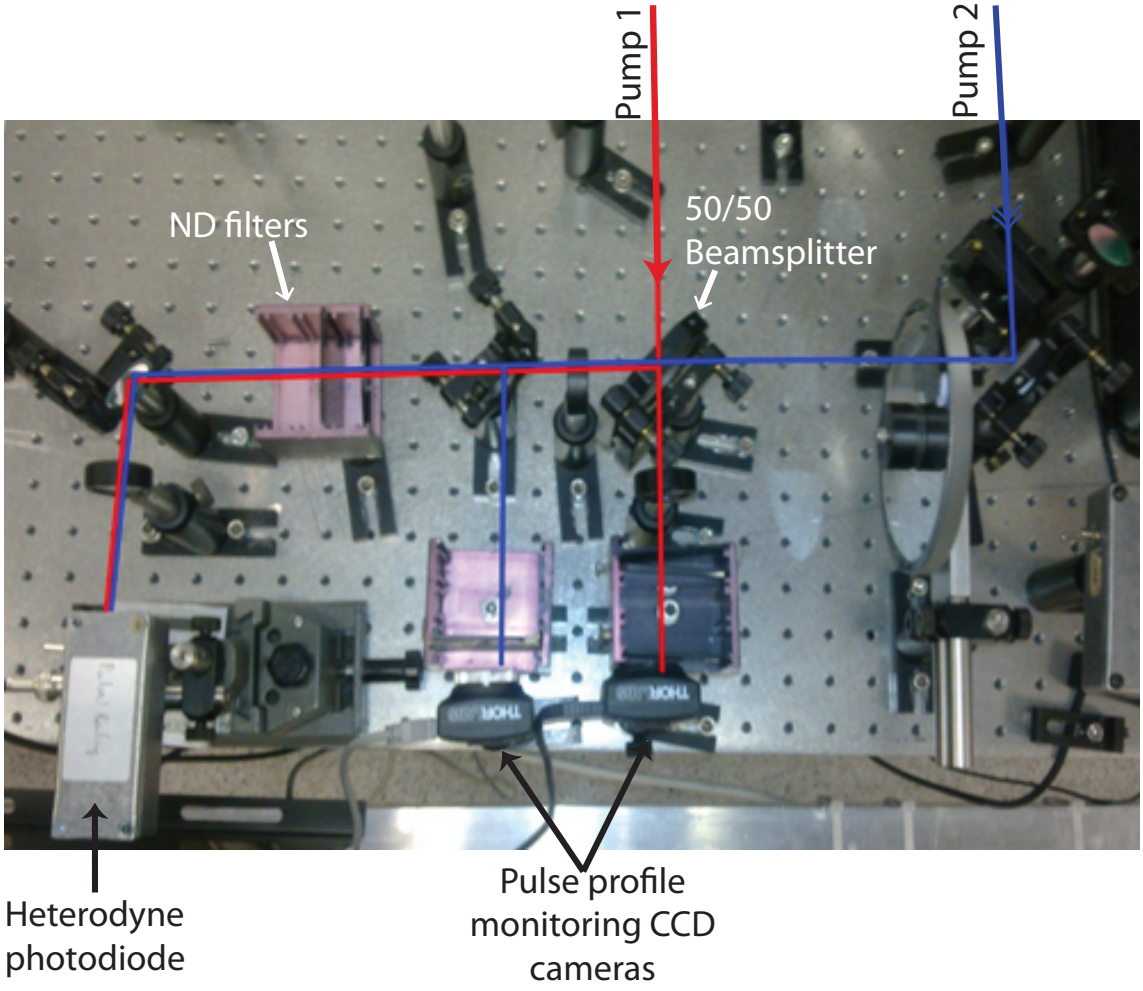

Figure 4.4: The diagnostics side of our optical bench. Portions of the two IR beams are heterodyned on a fast photodiode while their beam profile is monitored through two cameras.

program such as LabVIEW. For small frequency differences the period of oscillation is longer than the IR laser pulse duration, hence not easily measurable. However, since the induced frequency difference is linear with respect to the applied voltage, we can easily derive it by fitting a straight line to a voltage versus induced frequency graph (fig. 4.5 bottom). This measured frequency difference can then be converted into the velocity of the lattice through the relation

$$v = \frac{\Delta\omega}{\boldsymbol{q}} = \frac{2\pi\Delta f}{\frac{2\pi}{\frac{\lambda_{\text{pump}}}{\sin(\phi)}}} = \frac{\Delta f \lambda_{\text{pump}}}{\sin(\phi)}, \tag{4.2}$$

where $\boldsymbol{q}$ is the lattice wavevector, Δf is the induced frequency difference between the two beams, $\sin(\phi)$ is the half-angle between them and λ_{pump} is the unchirped pump wavelength. By controlling the frequency difference of the two IR beams we can thus control the velocity of the induced grating.

We need to mention that throughout this thesis, the wavevector is considered to be constant in the induced gratings for both constant frequency and frequency chirped lattices. Indeed, let us consider the equation for the lattice wavevector

$$\boldsymbol{q} = |\boldsymbol{k}_1 - \boldsymbol{k}_2| = 2\pi \sin(\phi)(\frac{1}{\lambda_{\text{pump1}}} + \frac{1}{\lambda_{\text{pump2}}}), \tag{4.3}$$

where $\boldsymbol{k}_1$ and $\boldsymbol{k}_2$ are the wavevectors of the beams forming the lattice and λ_1 and λ_2 their respective wavelengths. Should the laser beam frequencies have a time dependence (i.e. in the case of a chirped lattice), Eq. 4.3 can be rewritten as

$$\boldsymbol{q}(t) = \frac{2\pi}{c} \sin(\phi)(f_1(t) + f_2(t)). \tag{4.4}$$

It is apparent then from Eq. 4.4 that for a constant velocity lattice (constant frequency difference between the two beams) $\boldsymbol{q}$ will remain constant, whereas in the case of a chirped beam this equation implies $\frac{\Delta \boldsymbol{q}}{\boldsymbol{q}} = \frac{\Delta f}{f}$. For the IR laser beams which are used in our experiments to create the lattices, $\lambda_{\text{pump}} = 1064$ nm and for a chirp equal to 1 GHz we get $\frac{\Delta \boldsymbol{q}}{\boldsymbol{q}} = \frac{\Delta f \lambda_{\text{pump}}}{c} \approx 4 \cdot 10^{-6}$ which shows that effectively the lattice wavevector remains constant for the duration of the pulse. Finally, since the wavelengths used in the experiment are effectively the same, we can write the wavevector as

$$\boldsymbol{q}(t) = \frac{2\pi \sin(\phi)}{\lambda_{\text{pump}}}. \tag{4.5}$$

Obtaining a CBS spectrum

Once the alignment had been performed and the glass cell was filled with purified air (dust would be broken down by the lasers giving us erroneous signal) all lasers were released at full power. The frequency difference of the two pumps was set to a grating velocity equal to that of the speed of sound in air (≈ 340 m/s at 293^oK) which is where the maximum signal is expected. Indeed, should the alignment had been done precisely, a CBS signal would immediately be observed and fine tuning of the mirror mounts could be used to optimise the efficiency of the process. At optimum phase-matching, the signal beam was clearly observable by the naked eye.

CBS spectra could then be acquired by measuring the intensity of the Bragg scattered signal beam with respect to the velocity of the induced electrostrictive grating. Considering

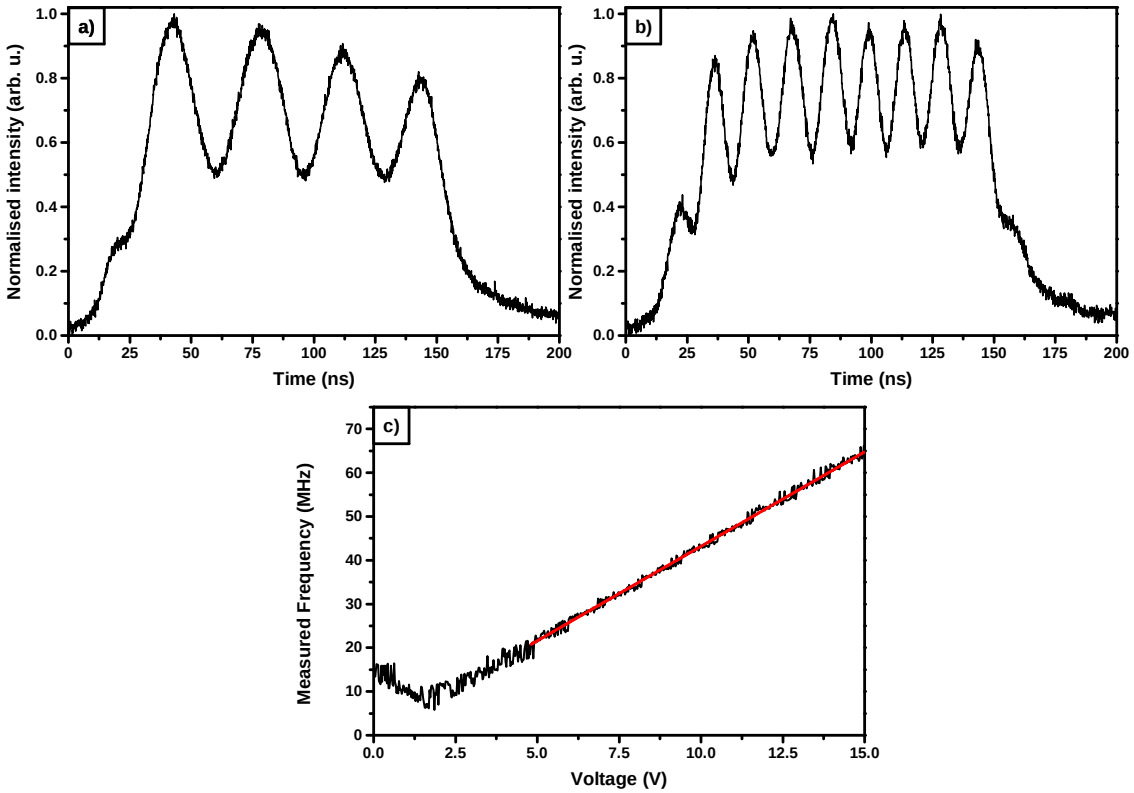

Figure 4.5: Figures a) and b): characteristic constant frequency interference patterns that were used in the CBS experiment, corresponding to frequency differences of 27 MHz and 60 MHz respectively. Figure c): characteristic frequency analysis that was used in order to convert the voltage applied to the EOM into frequency of the resulting interference pattern. In black is the measured frequency and in red is the fit to the linear portion of the curve from which information about the frequency at lower voltages is derived.

that the probe's pulse duration was much shorter than that of the pumps (Fig. 4.1), this allowed us to vary the pump-probe relative delay and observe the temporal evolution of the obtained CBS spectra.

Data acquisition

Given the fact that throughout the experiment we would ideally want to obtain CBS spectra in as many temporal positions of the probe with respect to the pump as possible, while keeping the frequency (lattice velocity) resolution as high as possible while simultaneously being limited by the 10 Hz repetition rate of our laser system, this would be a very lengthy measurement to be carried out manually. To enable efficient data acquisition, with good temporal and frequency resolution, the experimental procedure was computer automated.

A LabVIEW program was eventually written following a state-machine architecture. This program was of great importance since it meant we could reach the best possible result in the minimum possible time. Also, since it wasn't relying on the user for the

measurements to be performed, it eliminated the possibility for any systematic errors due to oscilloscope reading, fatigue etc. It also finally meant that we could monitor what was going on in a physically big lab, from the monitor of the user.

4.3 Results

One of the first things noticed while taking spectral scans for various pump-probe delays (Figs. 4.6 and 4.7), was that it was taking some time for the Brillouin peak to be stabilised in spectral position. Indeed, considering an interaction region width of 96 μm and a central speed of sound of ≈ 340 m/s at 293 K, it would take the Brillouin peak at this speed some ≈ 30 ns to reach its expected spectral position. This can be observed in Fig. 4.6.

After scanning though through the whole range of relative pump-probe delays with a 10 ns step, we observed sidebands appearing on either side of the Brillouin peak, which were becoming more distinct as the relative pump-probe delay was increased (noted with "s.b." in Figs. 4.6 and 4.7). These spectral sidebands, moved towards the Brillouin peak as the pump-probe delay was increased, while a width reduction of the main Brillouin peak was also observed with increased pump-probe delay.

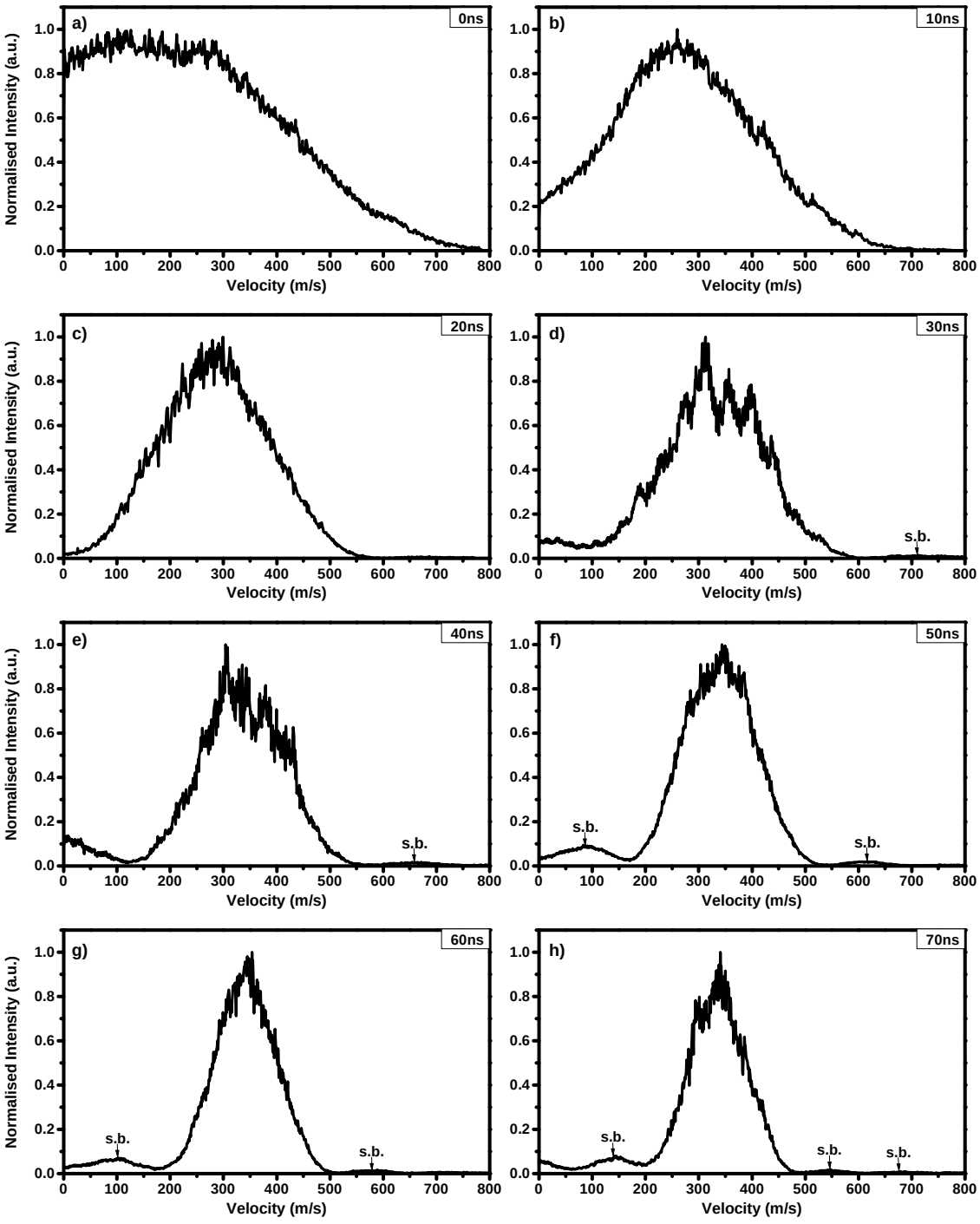

Figure 4.6: Experimentally obtained coherent Brillouin spectra for relative pump-probe delays of $0 - 70$ ns. Noted with s.b. are the positions of the observed sidebands.

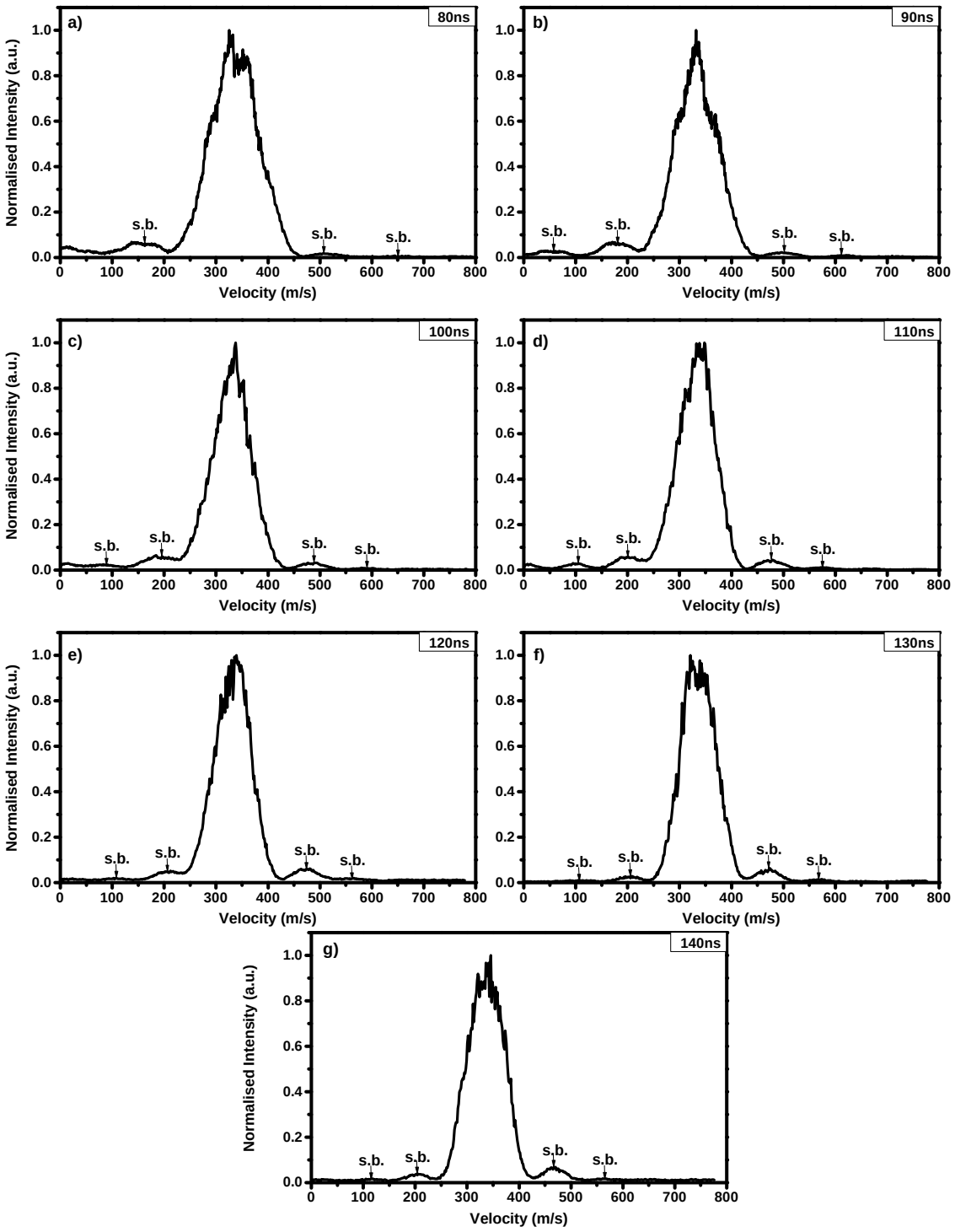

Figure 4.7: Experimentally obtained coherent Brillouin spectra for relative pump-probe delays of $80 - 140$ ns. Noted with s.b. are the positions of the observed sidebands.

We came to the conclusion that, although we were mainly inducing a density modulation via the electrostrictive force, in our process due of the thermalisation of the gaseous medium via absorption and subsequent thermal expansion, a secondary density modulation was produced in the form of acoustic waves propagating alongside our electrostrictive grating. These secondary acoustic (pressure) waves move away from the interaction region

in all directions [175]. Of importance to the CBS signal that we observe are the acoustic waves, which have a comparable wavelength to that of the optical lattice that created them, and travel in the same plane as the electrostrictive grating with a velocity equal to that of the speed of sound in the medium [176].

These acoustic waves also contribute to the Bragg scattered signal and have a strong effect when the lattice velocity is close to the speed of sound in the medium. The interaction between the electrostrictive grating moving at u_e and the sound wave at u_s forms the side bands observed in Figs. 4.6 and 4.7. As both gratings have the same period, but different velocities, constructive interference between each density grating occurs at specific relative velocities $u_\mathrm{e} - u_\mathrm{s}$ for a particular pump-probe delay. At these velocities the periodic density modulation and thus the Bragg scattered signal increases producing the sidebands in the spectrum. The relative velocity at which constructive interference occurs is given by

$$u_\mathrm{e} - u_\mathrm{s} = \frac{n\lambda_\mathrm{g}}{\delta t}, \tag{4.6}$$

where δt is the pump-probe delay and n is the integral number of wavelengths λ_g (defined from Eq. 4.1) moved due to the relative velocity between the two gratings.

4.3.1 Simulating CBS spectra

There is no analytical solution to the induced density modulation of the gas by the optical lattice in this regime. To determine this for a particular time and frequency difference between the two pump beams we numerically solve the axisymmetric 2D Navier-Stokes (N-S) equations in a cylindrical geometry subject to the volumetric longitudinal optical dipole force of the lattice F_z. The N-S equations are defined in [81] and the volumetric optical force on the gas due to the interaction with an electric field E_g of amplitude E_0 and frequency $\Delta\omega$ is given by

$$F_\mathrm{z}(r,z,t) = \frac{\alpha}{M}\rho\nabla_\mathrm{z}E_\mathrm{g}(r,z,t)^2 = \frac{1}{4}(\alpha_{\mathrm{O}_2}N_{\mathrm{O}_2} + \alpha_{\mathrm{N}_2}N_{\mathrm{N}_2})k_\mathrm{g}E_0(r,z,t)^2 cos[k_\mathrm{g}z - \Delta\omega t], \tag{4.7}$$

where ρ is the number density of molecules, M is the average molecular mass of the air and N_{O_2} and N_{N_2} are the number density of O_2 and N_2 respectively. The lattice wavevector is given by $k_\mathrm{g} = 2\pi/\lambda_\mathrm{g}$. The static polarisabilities of the major constituents of air (O_2 and N_2) are $\alpha_{\mathrm{O}_2} = 1.97 \times 10^{-40}$ $\mathrm{Cm^2V^{-1}}$ and $\alpha_{\mathrm{N}_2} = 1.8 \times 10^{-40}$ $\mathrm{Cm^2V^{-1}}$. A second order

MacCormack finite-difference scheme is used to solve the Navier-Stokes equations [177]. From the modulation in density, $\Delta\rho$, derived from the procedure above we then calculate the solution of the CBS signal $I_\mathrm{s} \sim |A_\mathrm{s}(r,z,t)|^2$ at each lattice velocity, time and position by solving the 1D wave equation given by

$$\frac{\partial^2 E(r,z,t)}{\partial z^2} - \frac{n^2}{c^2}\frac{\partial E(r,z,t)}{\partial t^2} = 0, \tag{4.8}$$

where $E(r,z,t,)$ is the superposition of the probe and the signal fields given respectively by

$$E_\mathrm{p}(r,z,t) = \frac{1}{2}A_\mathrm{p}(r,z,t)e^{-i(k_\mathrm{p}z-\omega_\mathrm{p}t)} + \text{c.c.}, \tag{4.9}$$

and

$$E_s(r,z,t) = \frac{1}{2}A_\mathrm{s}(r,z,t)e^{-i(k_\mathrm{s}z-\omega_\mathrm{s}t)} + \text{c.c.}. \tag{4.10}$$

These have amplitudes A_s and A_p and wave vector components k_s and k_p along the z-direction respectively, The refractive index is given by $n = n_0 + \Delta n$ where n_0 is the refractive index of the unperturbed gas and $\Delta n = (\Delta\rho/\rho)(n_0 - 1)$ is the modulation in refractive index variation induced by the lattice pump beams [178]. By utilising the slowly varying envelope approximation and realising that the optical field reaches a steady state on a timescale much faster than the fluid motion we therefore calculate the steady state values of the field for each time step of the fluid solver. These approximations lead to the well-known coupled mode equations (similar to those presented in Eq. 3.30) at each time step as

$$\frac{\partial A_\mathrm{s}(r,z,t)}{\partial z} + ik_\mathrm{p}\Delta n e^{-ik_\mathrm{g}z}A_\mathrm{p}(r,z,t) = 0, \tag{4.11a}$$

$$\frac{\partial A_\mathrm{p}(r,z,t)}{\partial z} - ik_\mathrm{s}\Delta n e^{ik_\mathrm{g}z}A_\mathrm{s}(r,z,t) = 0. \tag{4.11b}$$

Solutions of this model for several timings of pump-probe delays are presented in Fig. 4.8. These simulations were performed by Dr. Mikhail Schneider from the department of Mechanical and Aerospace Engineering at Princeton University. From the comparison with the experimentally gathered data, there is a good agreement with all features, namely the spectral sideband formation and the reduction of the main Brillouin peak.

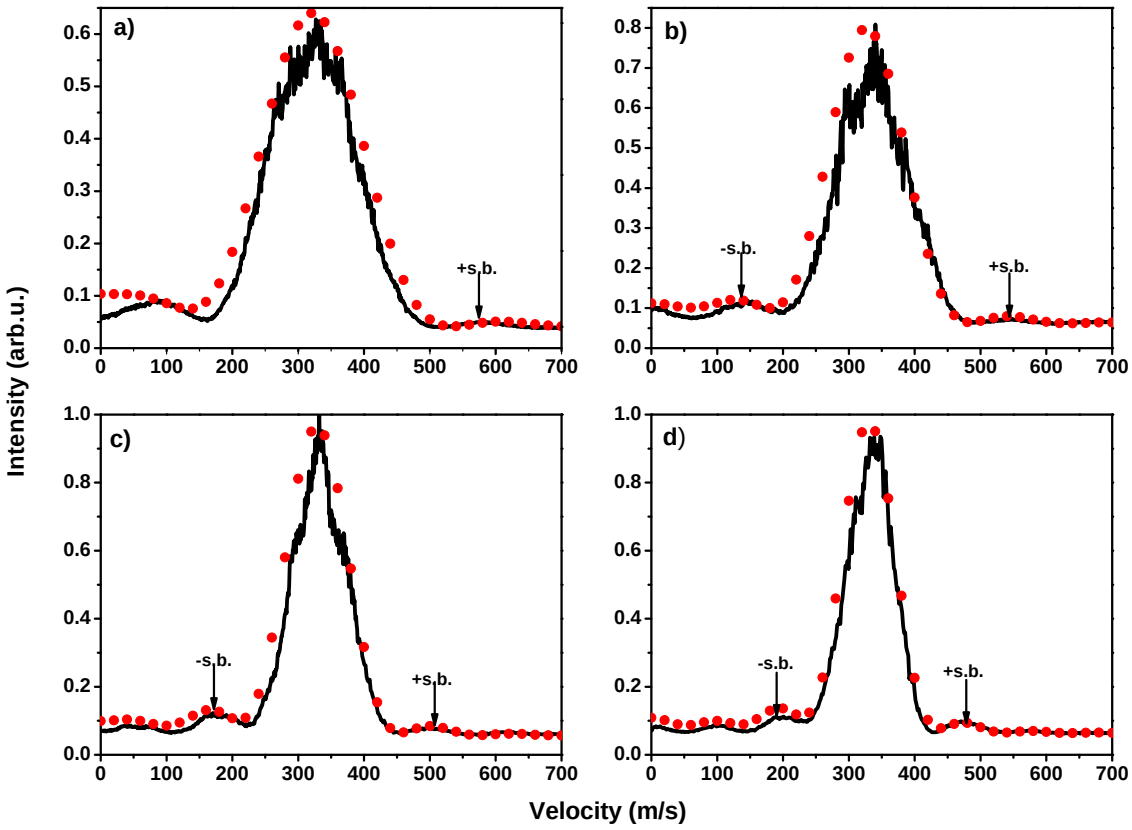

Figure 4.8: CBS spectra as a function of lattice velocity for four pump-probe delays of a) 50 ns, b) 70 ns, c) 90 ns and d) 110 ns. The black trace is the experimental data and the red dots are the simulated values for the CBS spectra. The observed sidebands are noted by -s.b and +s.b. depending whether they are observed in lower or higher velocities than the main Brillouin peak, respectively.

4.3.2 Validating the thermon formation.

In order to validate our model that an acoustic wave, similar to the ones generated in LITA, propagates alongside the induced electrostrictive grating in the medium, we plot the spectral positions of the sidebands versus pump-probe delay. These are observed in Figs. 4.6 and 4.7 with the positions predicted from our analytical model presented in Section 4.3.1 and the simple model presented in Eq. 4.6 which assumes that the acoustic wave is of a single wavelength and produced instantaneously at the start of the pump pulse. This plot is presented in Fig. 4.9. The circles in fig. 4.9 represent the first interference maxima ($n = \pm 1$) which are observed as the closest peaks either side of the Brillouin peak of each pump-probe delay of Figs. 4.8,4.6 and 4.7. The squares represent the 2nd interference maxima ($n = \pm 2$) which are observed as the 2nd closest peaks either side of the Brillouin peak of each pump-probe delay of Figs. 4.8,4.6 and 4.7. The solid shapes are taken from measured spectra, the hollow ones are predicted from Eq. 4.6 and the triangles are values taken from the simulated spectra. The crosses at approximately 340 m/s are

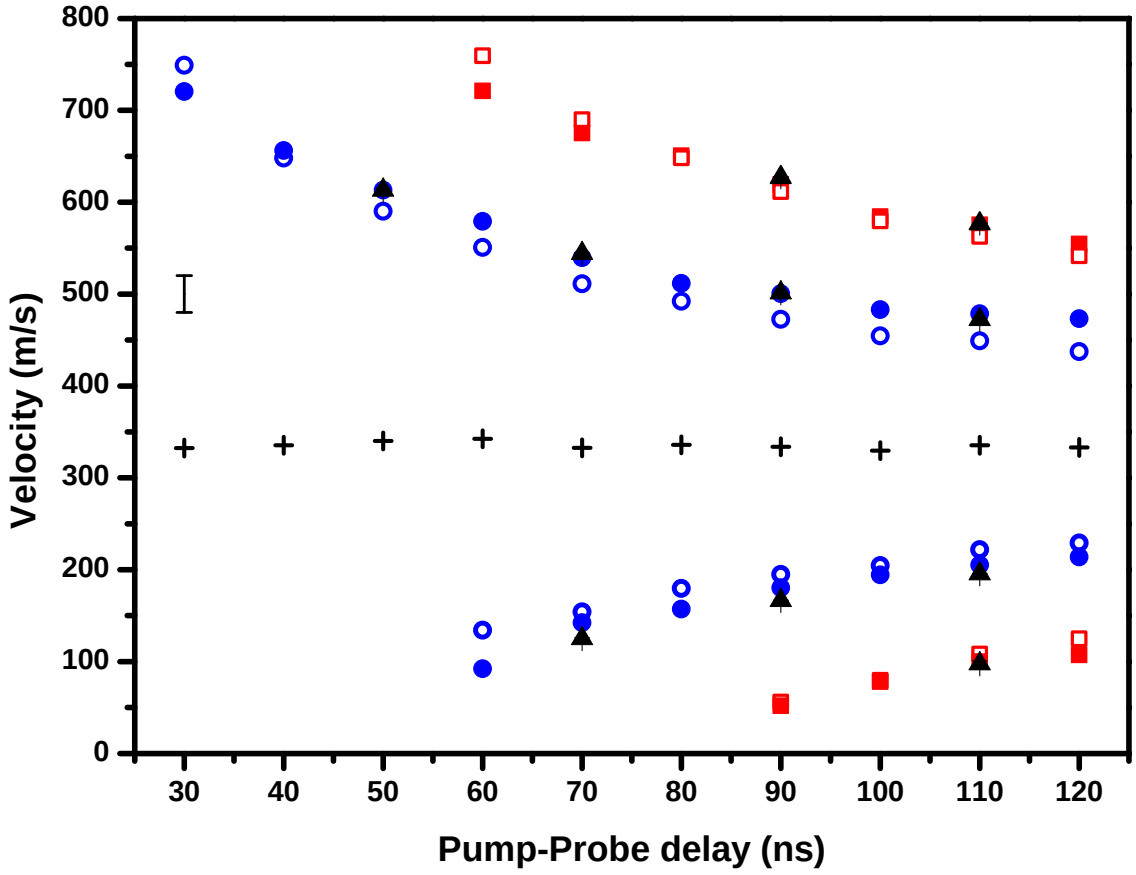

Figure 4.9: Plots of the spectral location of the sidebands for a range of pump-probe delays. The circles represent the first sideband maxima ($n = \pm 1$) which are observed as the closest peaks either side of the Brillouin peak for each pump-probe delay of Figs. 4.8,4.6 and 4.7. The squares are the 2nd sidebands ($n = \pm 2$). The solid shapes are experimental points and the hollow ones are predicted from Eq. 4.6. The triangular shapes are from the simulated spectra. The crosses are measurements of the center of the Brillouin peak which corresponds to the speed of sound in the gas. Also included is the typical uncertainty of the observed sidebands.

measurements of the center of the Brillouin peaks that correspond to the speed of sound in air. As this should be constant, the variation for different pump-probe delays represents the accuracy at which we can measure spectral features. There is very good agreement between the measured and calculated spectral position of the sidebands and also with our simple model (Eq. 4.6).

We observe that the sidebands follow a slow trajectory towards the position of the main Brillouin peak, suggesting that if we were to use pump pulses of longer pulse duration, for increased values of the pump-probe delay, even a bigger reduction of the width of the Brillouin peak would result, leading to erroneous estimates of the parameters relating to it, such as the gas temperature which is deduced by the width of the Brillouin peak.

A more detailed comparison between the measured and predicted spectral location of

the sidebands can be seen in Fig. 4.10 which is a logarithmic plot of the signal intensity as a function of lattice velocity for a pump-probe delay of 110 ns. Also included in this figure is a plot of the calculated CBS spectrum at the same pump-probe delay where the pump beams are slowly turned on with a linear ramp for the first 60 ns of the 140 ns pump beam pulse. No sidebands can be observed indicating that the fast turn-on when flat top pumps beams are used are responsible for the sidebands. In addition, the FWHM spectral width of the Brillouin feature is wider for the slow turn-on pulse than for the flat top profile showing the Brillouin peak is effectively narrowed by the presence of interference which leads to the sidebands. The inset graph in Fig. 4.10 is a plot of the FWHM of the CBS Brillouin peak as function of pump-probe delay for the measured (squares) and calculated (circles) spectra for the flat top profile. Also shown is the FWHM width for the simulated slow rise time pulse (triangles).

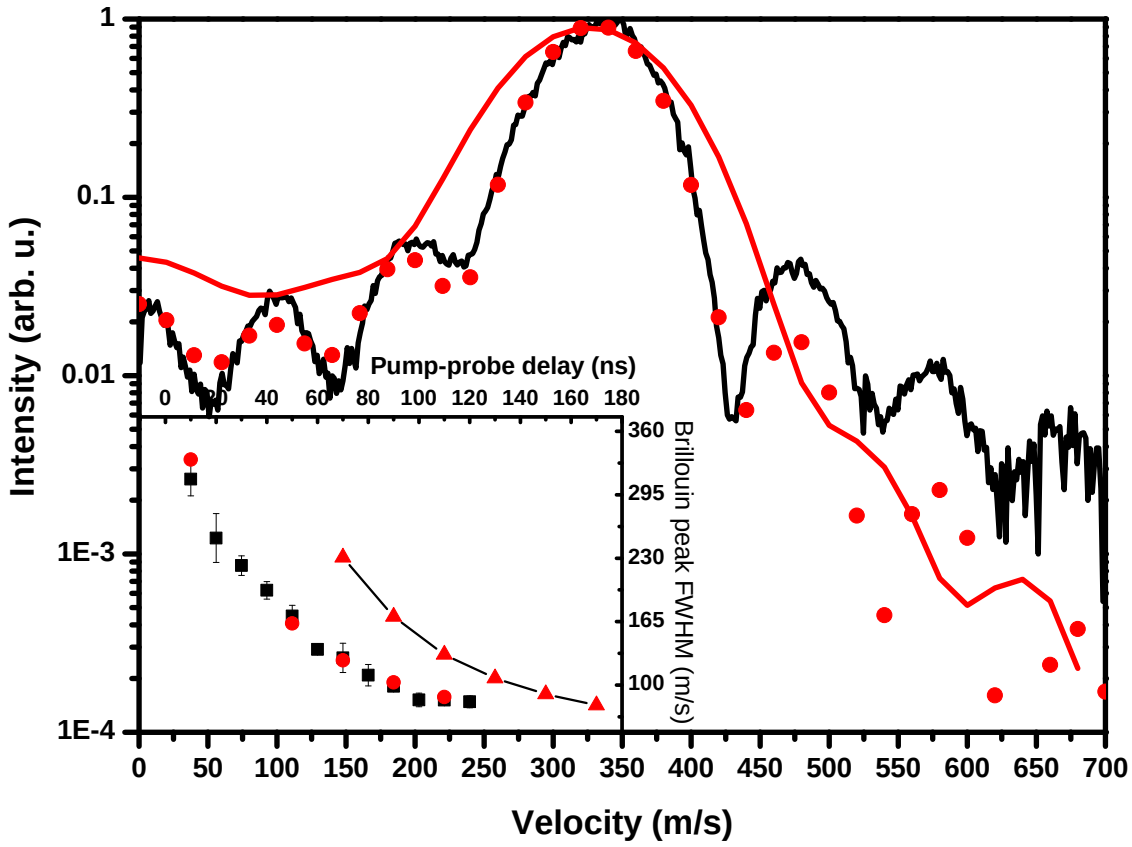

Figure 4.10: Plots of the CBS spectral profile for a pump-probe delay of 110 ns comparing the experimental spectrum (black line) with the simulated spectrum for the flat top pump beam profile (red circles). Also shown (red line) is the profile calculated for a slow rise time pump pulse where almost no sidebands are observed. The vertical intensity axis is shown on a logarithmic scale to indicate that all the predicted sidebands can be observed. The inset graph is a plot of the FWHM of the measured (black squares) and calculated spectra (red circles) for a range of pump-probe delays as well as for the slow rise time pump pulses (triangles). This graph shows that due to destructive interference between the dipole force grating and the acoustic wave that the line width of the Brillouin peak is approximately 40 % lower than for the slow rise time pump beam profile.

There is good agreement between the calculations and experiment using the flat top pulses but the FWHM of the Brillouin peak for the flat top profile is approximately 40 % less than that from the slow rise time pulses. The time of the decay of the width for all pulses is approximately the same for all cases and is consistent with that expected for the acoustic decay time of a plane wave in air by viscosity [179]. Importantly both line shapes limit to the same width such that for pulses significantly longer than the ones we used in

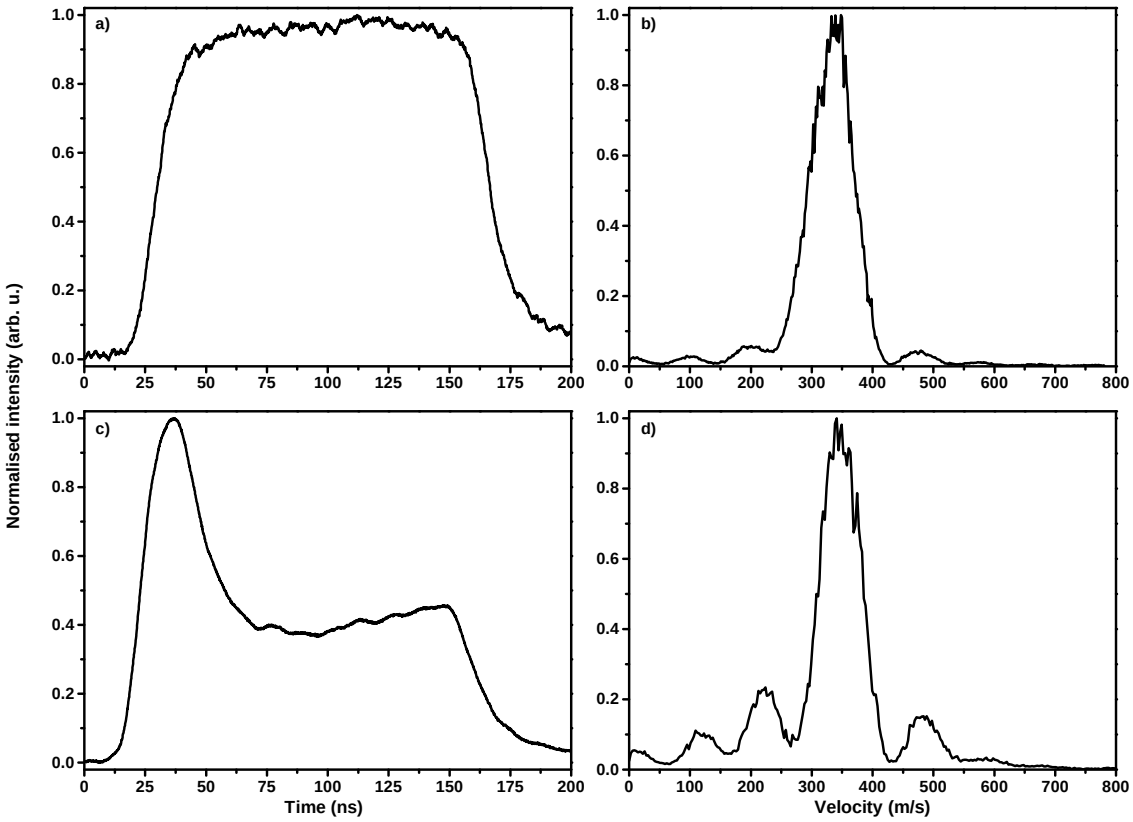

Figure 4.11: Plots of CBS (right column) for a pump-probe delay of 110ns when two different pump profiles are used (left column). We observe that the sideband formation can largely be enhanced (or suppressed) depending on the pulse profile used.

our experiment, the spectral profiles are expected to be independent of pulse duration or shape.

To provide a final experimental proof of how the pulse shape influences the sideband formation, we present a comparison between scans for the same pump-probe delay, taken with two different pulses: a flat top pump profile and a pump profile where the intensity of the initial $\sim 30\%$ of the pulse was $\sim 60\%$ more than the rest of it (Fig. 4.11). The use of such pulses allows us to modulate the intensity of the sidebands which can now reach intensities more than 20% of the main Brillouin peak, whereas with the use of the flat top profile they would have intensities of 5% to 7%. It is obvious then from comparing the results presented in Fig. 4.11 to the simulated data from Fig. 4.10 for the slow ramp pump profile, that thermalisation of the gaseous medium takes place in the first 30% to 40% of the pump pulse duration. One must then take that into consideration when performing such scans.

4.4 Conclusions

We have measured the CBS spectral profile as a function of time by utilising high intensity, long duration pump pulses which induce both acoustic and dipole force perturbations to the gas density. The interference between these two density gratings creates time dependent spectral sidebands and causes narrowing of the Brillouin peaks. Up to three sidebands have been observed and their spectral position with time agrees with a very simple model that assumes that most of the sound wave is produced at the beginning of the pulse. Further experimental proof to this assumption was also provided.

These sidebands cannot easily be observed for pump-probe delays of less than 30 ns and explains why these features may have not been previously reported using conventional laser pulses with typical durations in the 10 ns range. Our results indicate that the sidebands and the resulting spectral narrowing can be suppressed or enhanced by the temporal pump pulse profile. The location of the sidebands as a function of pump-probe delay is however independent of pulse shape.

The ability to use long pulses leads to an increase in the CBS signal to noise ratio. However, because the CBS spectral profile is strongly dependent on the shape and duration of the pump pulses, care must be taken to carefully incorporate the temporal pump pulse shape and intensity when using CBS and CRBS line shapes to measure gas properties when utilizing pump fields with durations exceeding 30 ns.

Finally, we note that this method is similar to the method of laser-induced gratings which typically watches the decay of a laser induced acoustic perturbation. We instead use CBS to observe the creation of an acoustic wave as both a function of time and also with the velocity of the laser induced travelling dipole force.

Chapter 5

Single shot coherent Rayleigh-Brillouin scattering

5.1 Introduction

Coherent Rayleigh-Brillouin scattering has been used many times over the past fifteen years as a means to probe inherent properties of media in the gas phase [145, 49, 146, 147, 180, 52, 181, 150, 151, 152, 182], be it in a lab environment or in combustion and flow measurements. The techniques used in the field so far though, do have a major drawback that is the acquisition time. As was outlined in Chapter 4, in the CBS studies we performed, a single spectrum could at best be acquired in $\sim$ 20 minutes. This limits the application of CRBS to environments where fast acquisition times are required, such as flow environments.

As part of the work performed for this PhD thesis, we addressed this issue by developing a method to acquire a single CRBS spectrum in the duration of one single laser shot ($\sim$ 140 ns in our case), thus reducing the acquisition times by ten orders of magnitude. This reduction in acquisition time makes CRBS an ideal technique for diagnostics in environments such as transient flows and combustion.

5.2 The story thus far

So far in all reported experiments on CRBS, either the frequency of the probe or the frequency of the pumps had to be scanned in order for the resulting spectrum of signal intensity versus lattice frequency (and hence lattice velocity) to be obtained.

In the first CRS implementation [145], two equipolarised broadband pump beams, derived from the same laser (by use of a 50/50 beamsplitter), were used to create a range of lattices in the medium, with frequencies spanning the whole bandwidth of the pump beams, from which an orthogonally polarised narrowband probe was scattered. An etalon was then used to measure the scattered frequency distribution, for various frequency values of the probe.

Although this technique has been successfully used over the years [49, 146, 147, 181], it is a technique requiring a stable frequency calibration of all involved beams as well as a good stability of all the lasers involved over the duration of a scan which, depending on the averaging and resolution used, typically takes some 30 minutes for a spectrum to be acquired. Also, the requirement for thermally stable etalons adds extra complexity to the method.

A different approach to scanning the probe, was proposed and implemented in [150] where it was now the frequencies of narrowband pumps that were scanned, while the probe was simply derived from one of the pumps. Thus by measuring the beat frequency of the two pumps, the frequency of the resulting optical lattice could be determined allowing for spectra of signal intensity versus lattice frequency to be obtained. This kind of experimental setup has also been used by other groups [182] with success.

This method is not different to the one used in the coherent Brillouin experiment presented in the previous chapter, but with the added complexity of having to constantly monitor the frequency of the two pump lasers creating the lattice, with the serious stability issues this adds to the setup. In contrast, in our CBS experiment the two pump beams were derived by the same seed laser, thus maintaining a fixed relative frequency, with the absolute frequencies of the two pump beams being unimportant. In both cases though, still depending on the resolution and the averaging, a scan would normally take typically 30 minutes for a spectrum to be acquired.

In both approaches, one of the main limitations is the repetition rate of the flash lamp pumped laser sources. These lasers have a repetition rate of 10 Hz, a figure mainly limited by the rate at which the flash lamps pumping the Nd rods can be switched on and off. Should the repetition rate be in the kHz, these CRBS spectra would be acquired on much faster time scales. Since high repetition rate, high energy per pulse lasers don't exist, an alternative solution needs to be found.

5.3 An alternative solution: chirped lattices

Our solution still involves scanning the frequency of the pumps. But we do this very *fast*. Since our laser system is capable of delivering lattices with linear chirps of up to 1.5 GHz over the pulse duration, and since the molecular response to the applied fields occurs on a much faster timescale, we can address all of the frequency components resulting in the CRBS spectrum, in just a single laser pulse. And since we have the ability to start the chirp with an initially large frequency difference, passing through zero around the centre of the pulse, and then increase it again, we can map out both Brillouin peaks around the central Rayleigh peak, and not just either one of them as was the case in CBS - we've got time to spare now.

Essentially what we are doing is obtaining the CRBS spectrum in the time domain which we then, by simultaneously monitoring and measuring the used chirped lattice frequency, can translate back into the frequency domain - and all in the duration of one laser pulse.

5.3.1 Experimental setup

The setup does not need to be greatly different from that used for CBS, apart from two key differences. The probe to be used in single shot CRBS is derived from one of the pumps and is then orthogonally polarised so as not to interfere with the two pumps. It is separated by a thin film polariser which is placed right after a $\lambda/2$ waveplate, which also determines the amount of light coupled into each of the beams. In fact any probe beam with duration equal to or longer than the pumps could be used, since we want to map out the lattice frequencies for the duration the pump fields are on. Even a CW beam would give the desired result, should the signal intensity be strong enough to be detected.

Because of the geometry used in CBS, only a small DC voltage needed to be applied to the EOM in order for the required lattice frequencies to be obtained, which would not exceed a value of 80 MHz. Hence the EOM was directly connected to a waveform generator. Since in CRBS a counter-propagating geometry is preferred to a co-propagating one, so that the mean free path of the molecules would be comparable to the lattice wavelength (i.e. operation in a smaller y-parameter) and both Rayleigh and Brillouin features can be distinguished, higher lattice frequencies are required as well. Also the voltage signals need to be fast-switching linear ramps to the desired upper voltage value. In order to achieve

that, the output of a controllable waveform generator[1] was the input to a high voltage amplifier[2] which would amplify our voltage signal 20 times in the required time.

A summary of the chirping process used in the single shot CRBS experiment can be seen in Fig. 5.1. A voltage ramp (Fig. 5.1(a)) is sent to the EOM when the second pulse is passing through the pulse shaper (Fig. 5.1(b)). Figure 5.1(c) shows the temporal profile of the output of one of the two arms of the custom made amplifier, while Fig. 5.1(d) presents the resulting heterodyned signal, measured on a fast InGaAs photodiode. Figure 5.1(e) is the frequency analysis of the heterodyned signal, as it was described in Section 2.4.3.

5.3.2 Geometry and alignment considerations

The geometry we used in single shot CRBS is the same counter-propagating geometry, originally used in [145] and in most CRBS experimental studies thereafter [49, 146, 181, 182]. A full crossing angle for the pumps of 178^o results in a lattice wavelength of ≈ 532 nm (Eq. 4.1), much smaller than the lattice wavelength of 12.2 μm that was used in CBS. This allowed us to reach lower y-parameter values. The probe, since it has the same wavelength as the pumps, crosses the lattice at the same angle, only symmetrically to one of the pumps, allowing phase-matching (zeroth order Bragg scattering). The geometry that was used in single shot CRBS is presented in Fig. 5.2.

The main difficulty in obtaining a single-shot CRBS signal in this geometry lies in the alignment. Since the beams are counterpropagating, we don't have the option of aligning them with a CCD camera. A first step in making sure that the alignment is correct, apart from using similar masks to the one in Fig. 4.2(c), is to use a pinhole positioned at the intersection of the focii of the beams from the two lenses. That alone was not enough, because the distance between the two lenses is in order of ~ 1 meter; three beams intersection at the two holes on the masks and the pinhole between them over that distance did not guarantee that they were completely coplanar, simply because the distance was not long enough. Although the beams might have seemed to be properly aligned, in fact they generally weren't and no single shot CRBS signal could be observed.

In order to overcome this, we installed irises on the outputs of the two pump beams from the custom amplifier. By doing so, we were able to add an extra $2-3$ meters for alignment purposes, and ensure that all beams were propagating on the plane set by these

[1] 3314A function generator by Hewlett-Packard
[2] A-303 high voltage amplifier by A.A. Lab Systems

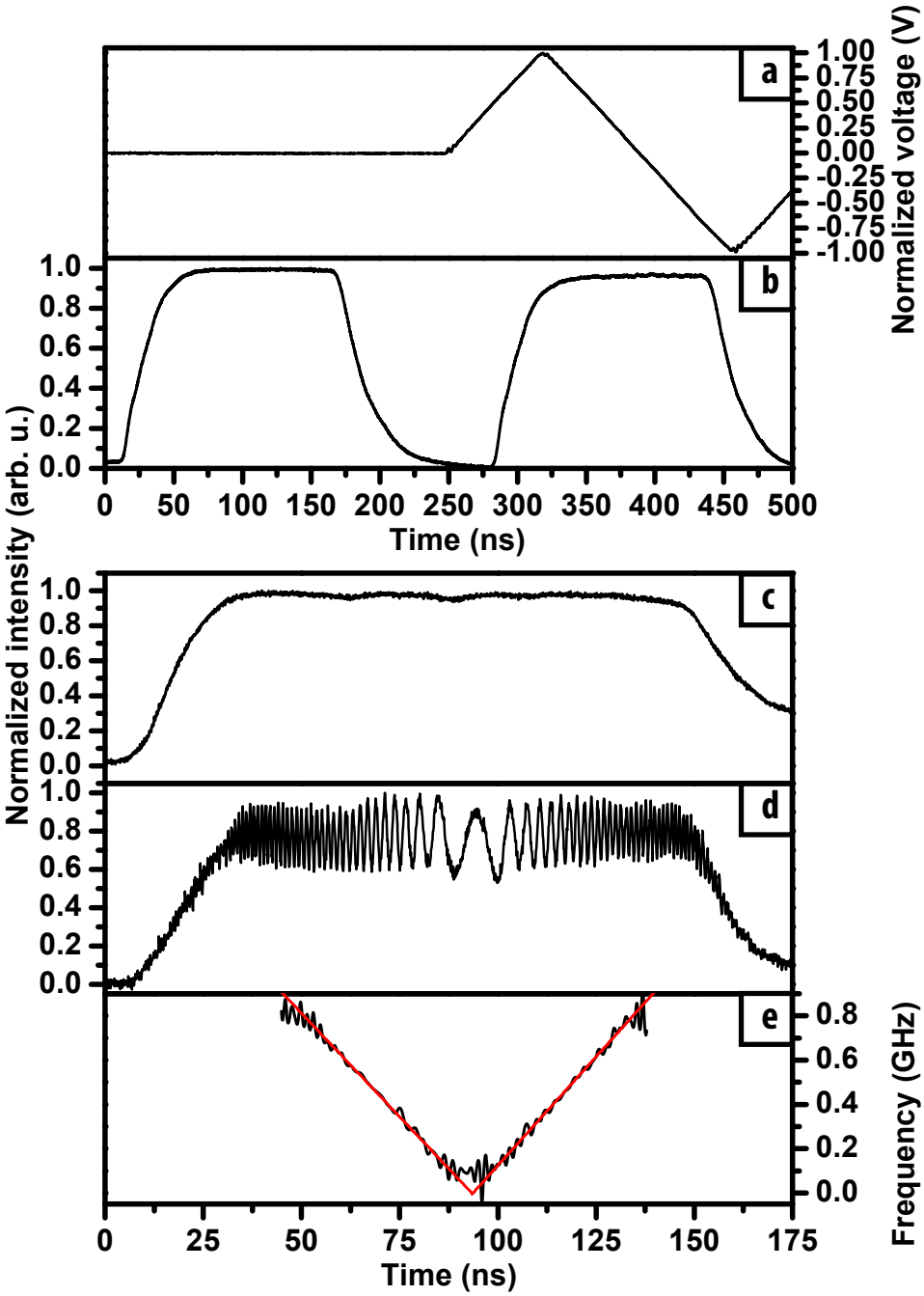

Figure 5.1: A diagram showing the optical lattice created by the laser system. a) The voltage applied to the $LiTaO_3$ EOM which frequency chirps the microchip laser. This occurs when the second pulse is passing through the pulse shaper, as shown on b). c) The intensity profile of an individual pulse from one of the two arms of the Nd:YAG amplifier. d) The heterodyned signal from both arms as a function of time shows the phase difference as function of time between the two beams. The black trace in e) shows a plot of the derived frequency difference between the two beams as a function of time using the data in d). The red trace in the same graph is a linear fit. Linear frequency differences of up to 1.4 GHz and beam energies up to 500 mJ/pulse can be achieved with this system.

two irises and the pinhole in the centre of the interaction region. Also, for alignment purposes, similar to the way the probe was extracted from pump beam 2 (Fig. 5.2), a

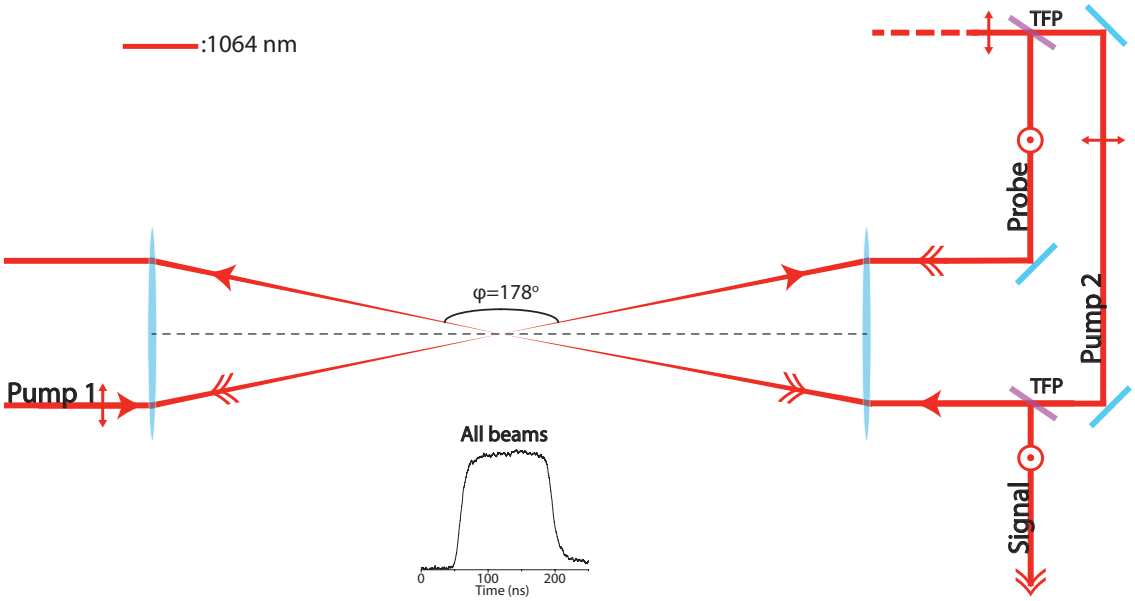

Figure 5.2: Schematic of the geometry used in our single shot CRBS experiment. Also shown is the temporal profile for all of the beams used in the experiment. The probe beam is separated by a thin-film-polariser (TFP) from pump beam 2 and orthogonally polarised in order to avoid interference with the two pump beams. The resulting signal beam counter-propagates pump beam 2, and is separated from it by another TFP.

fourth beam (which we call the *alignment beam*) was extracted from pump beam 1 which allowed us to align pump beam 2 along that path, but also to place the detector where the signal beam would be expected. The signal beam, resulting from the probe beam, counter propagates to pump beam 2 and is separated from it with the use of a thin film polariser. Once alignment is finished, the alignment beam is eliminated, pump beam 2 and the probe beam are set to 50/50 extinction and all beams are set to propagate at full power at the centre of the same glass cell as the one used in CBS, filled with CO_2 at 700 Torr.

Having placed a CCD camera where we were expecting the signal, if the alignment was correct, we could immediately observe the signal beam, which would vanish if we blocked either of the three beams involved in the experiment. Were we to stop frequency chirping, we could see the signal beam on the CCD camera moving at very low speed whereas if we applied the chirp we could see it moving very fast, in a similar fashion to what observed while aligning the beams in CBS. We then optimised the signal intensity as observed on the CCD camera. Further optimisation was done with the signal recorded on a fast photodiode which replaced the camera. The signal that was observed on the oscilloscope is presented in Fig. 5.3.

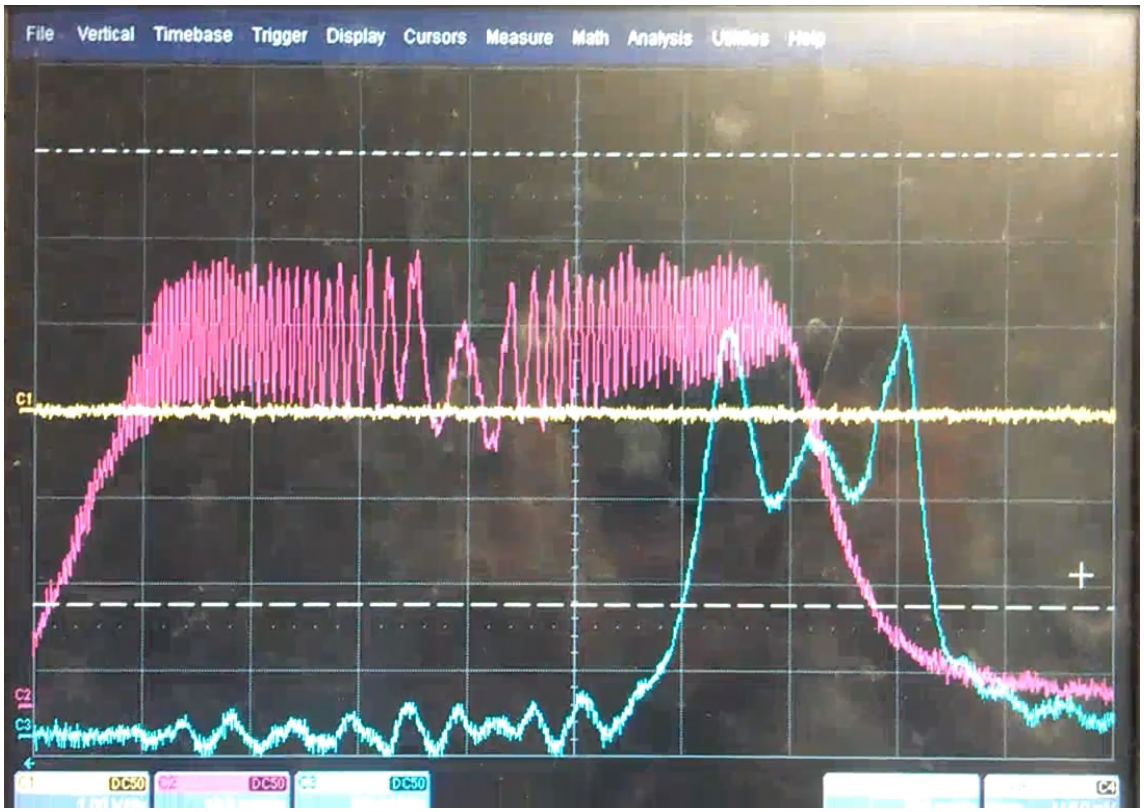

Figure 5.3: Actual photograph of the oscilloscope, where in red is seen the heterodyned interference pattern used for single shot CRBS and in blue is the resulting single shot CRBS spectrum. The CRBS spectrum appears to have a delay in time with respect to the lattice, due to the fact that they are being measured at different positions with different coaxial cable lengths.

One small issue

Since the probe was counter-propagating to pump beam 1 when alignment is optimum there is a very good chance that some of each beam would be fed back into the other arm, causing backwards amplification, which could damage the laser. In order to prevent this from occurring, a series of thin film polarisers and isolators had been placed right at the exit of the two amplifier arms. Although this measure did prevent the probe being fed back into the pump beam 1 amplifier arm, this was not the case for pump beam 1 feeding back light into the other arm. Although most of the pump beam was eliminated, a very small fraction of it still managed to be fed back, causing frequency instability on the resulting interference pattern. This could be observed after approximately half the duration of the pulse. Some ways to have overcome this would have been to use an extra isolator (which we didn't have at our disposal) or increase the path lengths of the two arms, where we didn't have the physical space to do so. As is expected then this was causing some discrepancies in the obtained single shot CRBS signal which I will discuss later in this chapter.

5.3.3 Data acquisition considerations

There would usually not be the need in such a system for a complex data acquisition program, since the CRBS and lattice frequency waveforms can directly be saved from the oscilloscope and then further analysed remotely. We had seen the need though to be monitoring in real time the induced chirp and the resulting CRBS signal since for example, should the pump beam profiles not be flat enough, the amplitudes of the two Brillouin peaks would be uneven - which should be avoided in such measurements, as in theory the two symmetrical Brillouin peaks should have the same amplitude. Another useful measurement that we need to make "live" is monitoring the rate at which we are chirping, before obtaining the single shot CRBS spectra since ideally we'd want chirp rates corresponding to lattice velocities greater than where the spectral positions of the Brillouin peaks were to be expected.

Since we had the means to obtain CRBS spectra in a minimal amount time, this gave us the possibility to perform dynamic parametrical CRBS studies with respect to e.g. pressure. This allows us to test the CRBS theoretical models in various y-parameter regimes, as well as prove our single shot CRBS method to be an adequate measurement technique for flow and combustion environments. By normalising the resulting spectra to unity, we are able to see how the CRBS spectra evolve and what spectral features dominate in a large y-parameter range.

We chose to write the program in LabVIEW, for the same reasons as we did in the case of CBS. The program for single shot CRBS was simpler than the one for CBS, and instead of a state-machine architecture, it would just be comprised of a while loop, running at the same repetition rate as the laser. In order for the parametric scans to be obtained and recorded, the output valve of the glass cell was opened so that the vacuum pump would slowly reduce the gas pressure in the cell. Then, the program would automatically log every CRBS spectrum corresponding to the respective pressure in the cell.

5.4 The results

To test the single shot CRBS method, experiments were performed over a range of pressures using Xenon and CO_2 gases. Figure 5.4a is the heterodyned signal recorded during single shot CRBS measurements. A well-defined chirp is recorded from 30 ns to 95 ns which corresponds to lattice velocities of -800 to 0 ms^{-1} and allows us to record half of the

symmetric CRBS spectral profile. For longer time delays, as we mentioned earlier, optical feedback from one arm of the amplifier into the other prevents single mode operation of the laser and thus only half of the spectrum is reproduced accurately.

Figure 5.4b is a single shot spectrum obtained from CO_2 gas at 700 Torr at room temperature (292 K). This corresponds to a y-parameter of 1.62 (in contrast to a value for the y-parameter of ≈ 27 that was explored in CBS). The grey trace is the profile recorded in the experiment while the black trace is this spectrum averaged over 50 laser pulses. The red trace is the calculated spectrum as described in Section 5.4.1. The recorded spectra show the main features of a CRBS spectrum and include the Brillouin peak due to the bulk motion of the gas which is centred at roughly the speed of sound in the medium. Also shown is the weaker Rayleigh peak due to the microscopic motion of the gas. Both the single shot and averaged measurements show a small deviation from the predicted profile indicating the utility of this technique for detailed comparison with theoretical models. It is obvious that should there not have been optical feedback the "positive" Brillouin peak would have been unaffected and symmetrical around zero to the "negative" one. Because of the feedback though, the spectral position of the second peak does show some discrepancy both in position as well as in width, and it is only presented for completeness in Fig. 5.5.

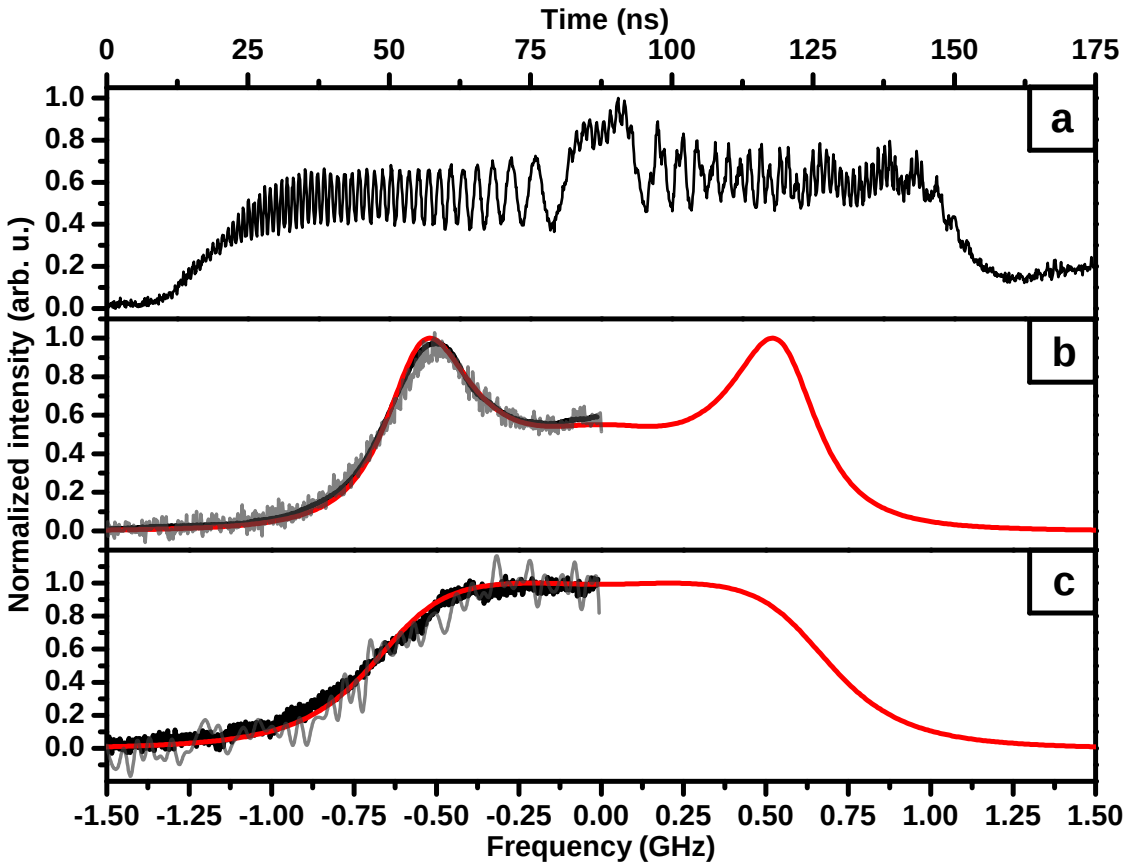

Figure 5.4: Graph a) shows the recorded beat pattern between the two lattice beams which is used to determine the frequency difference and lattice velocity as a function of time in the CRBS experiments. Graphs b) and c) show the CRBS experimental spectra (black traces) and the theoretical calculations (red traces) for CO_2 gas for pressures of 700 and 270 Torr, respectively. The graphs contain both normalized single shot CRBS spectra (gray trace) and spectra averaged over 50 laser pulses (black trace).

We have also recorded spectra at lower y-parameters. Figure 5.4c shows a CRBS spectrum recorded at a pressure of 270 Torr at 292 K which corresponds to a y-parameter of 0.62. At this lower pressure the Brillouin peaks are less pronounced compared to the Rayleigh features. Since the CRBS signal scales as the square of the gas density, the recorded signal is significantly lower than that at 700 Torr. At this pressure, however, we can still make a good comparison with the simulated spectral profile in a single shot using an unamplified photodiode.

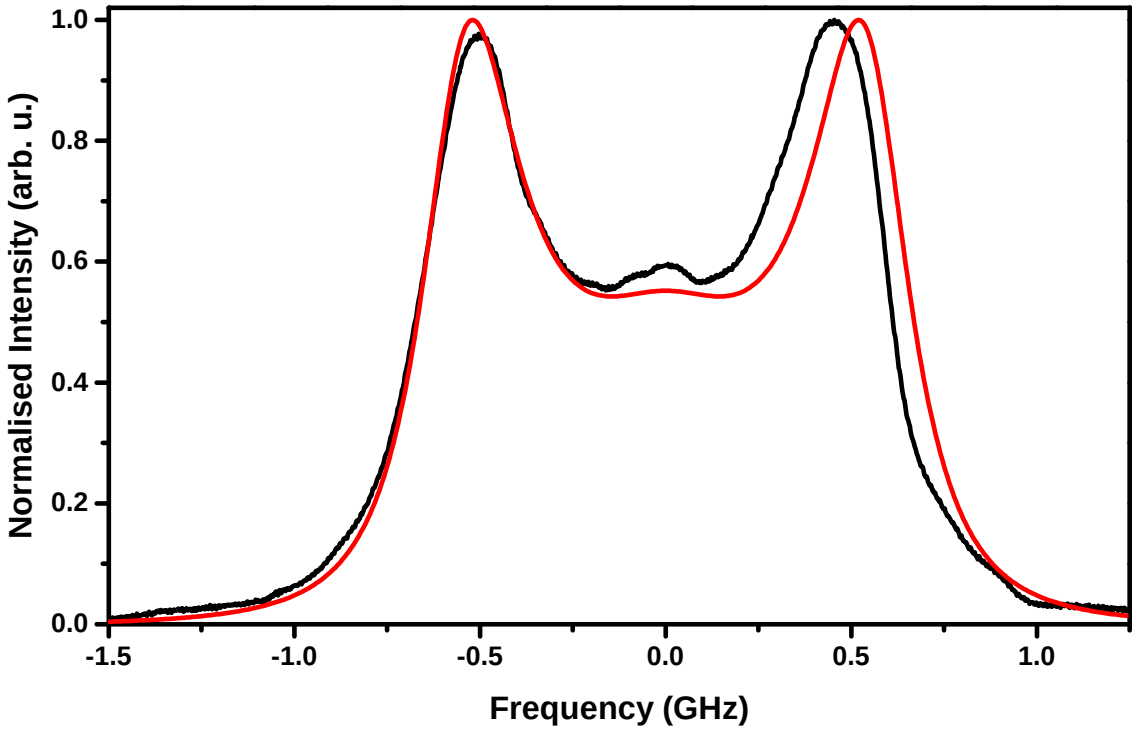

Figure 5.5: CRBS spectrum for CO_2 gas at a pressure of $\sim$ 700 Torr, averaged over 50 laser shots (in black) and the simulated spectrum (in red). It is obvious that the optical feedback starts deteriorating the spectral shape after approximately half the Rayleigh peak, while it also shifts the position of the second Brillouin peak and its width. Should the feedback not have been present, there should be no reason why the second half of the spectrum wouldn't be the same as the first, unperturbed, half.

5.4.1 Spectral simulations

For CO_2 gas, the CRBS spectral profile is obtained for a known set of thermodynamic functions using the Tenti s7 kinetic model [146]. When modelling CRBS in CO_2 for the experimental conditions used in our single shot experiments, the CO_2 vibrational modes are considered to be frozen because the frequency shift between the pump beams, which corresponds to the phase velocities close to the sound velocity, is on the order of 1 GHz, much slower than the vibrational excitation rates which lie in the THz regime [147]. Therefore, it is safe to assume for our experiments that the heat capacity ratio of CO_2 is $\gamma = c_p/c_v \approx 1.4$, as it is for linear molecules such as N_2. The presented results in Fig. 5.4, correspond to the same set of CO_2 gas-dynamics parameters assumed in [147], where $\gamma \approx 1.4$, shear viscosity $\eta = 14.6{\times}10^{-6}\ Pa{\cdot}s$, bulk viscosity $\eta_b = 0.25{\cdot}\eta$ and heat conductivity $\lambda = (1/4)(9\gamma{-}5)\eta c_v$. The vibrational modes are frozen so that $c_v = (1 + 3/2)R$, where $R = 188.93\ J/kg \cdot K$ is the gas constant. These simulations were performed by Dr. Mikhail Schneider from the department of Mechanical and Aerospace Engineering at Princeton University.

As in other approaches to CRBS, temperature, sound velocity and bulk viscosity can be measured for a single component gas at different densities and pressures by comparison with the s6 and s7 Tenti theory. Sound velocity at high density (Brillouin peak) can be measured for gas mixtures but for all other parameters to be determined the gas composition is required. As the analytical theory becomes more complicated at high density it is possible to apply DSMC (Direct Simulation Monte Carlo) to determine the CRBS profile. Comparison of DSMC results with CRBS experiments may be a future route for the definition of all thermodynamic parameters in gas mixtures. This includes high-speed flows and in combustion.

5.4.2 Parametrical three-dimensional (3D) CRBS profiles

In all previous CRBS experimental studies, because of the time required for the reproduction of one CRBS spectrum, usually the studies were performed for one or maybe two values of the y-parameter. By exploiting the technique we have presented in this chapter, we now have the possibility to obtain a whole range of CRBS spectra in a minimal amount of time for various values of the y-parameter. This gives us the chance to experimentally monitor any changes in the experiment's operating conditions in real time (such as gas temperature, flow, pressure etc.) and produce vast sets of data for theoretical comparison.

In order to demonstrate this capability, we recorded single shot CRBS data with respect to pressure, averaged over 50 laser pulses per spectrum. In order to experimentally achieve that, the only thing that had to be changed in the experiment was, rather than operating at a constant pressure, to open the outlet valve of our glass cell just a bit to reduce the gas pressure at a low, steady rate, while recording the acquired spectra through our LabVIEW program. All the acquired spectra were each normalised to unity in order to allow for comparison of the spectral lineshapes with respect to pressure. With this technique, for ~ 100 pressure values and with an averaging of 50 laser pulses per spectrum in a 10 Hz repetition rate, it only takes us ≈ 8.5 minutes to acquire 3D spectra such as the ones presented in Figs. 5.6.

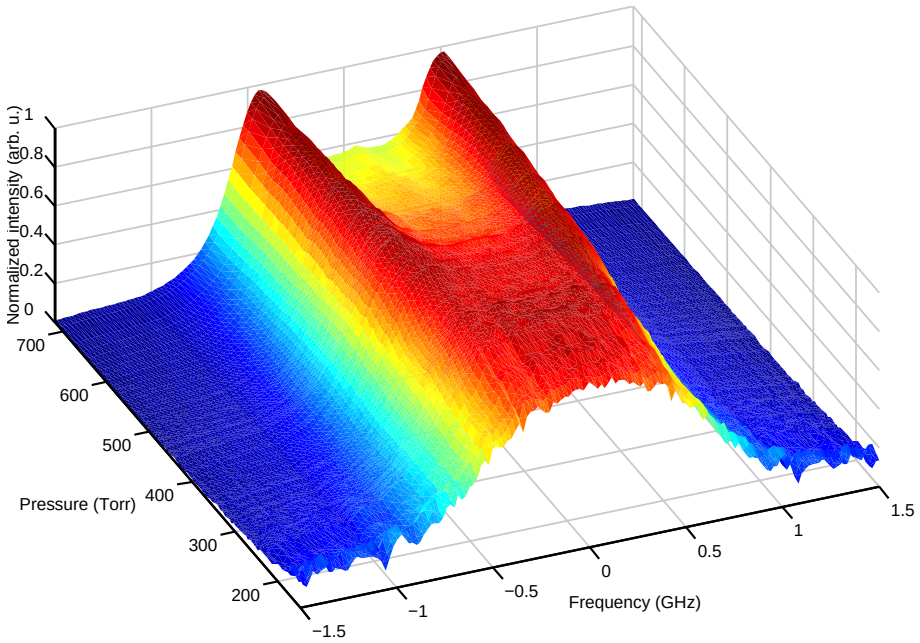

(a)

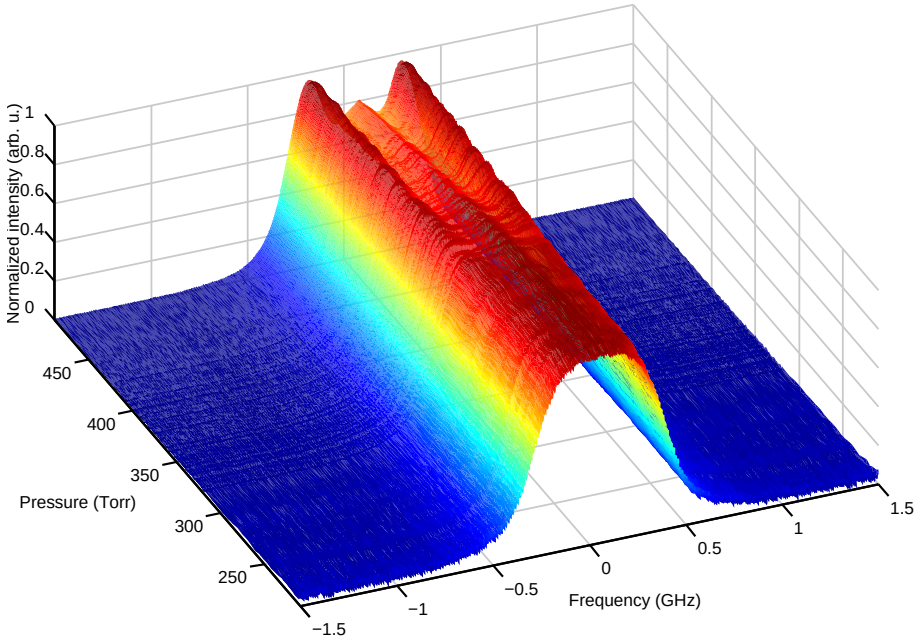

(b)

Figure 5.6: (a) 3D CRBS spectrum for CO_2, comprised of 78 individual spectra (b) 3D CRBS spectrum for Xenon, comprised of 134 individual spectra

5.5 Conclusions

We have presented a technique for fast acquisition of CRBS spectra, over the duration of a single laser shot. Experimental spectra have been acquired and compared with well-established theoretical models, with which there is good agreement, while $3D$ parametrical CRBS spectra have been presented over a large range of y-parameters, for the first time to our knowledge. This technique renders CRBS an ideal candidate for diagnostics in combustion and transient flow environments. An experiment employing single-shot CRBS for nanoparticle detection in plasmas is about to start at Princeton Plasma Physics Laboratory (PPPL), showing the applicability of the method.

The frequency resolution in our technique is fundamentally limited by the detector temporal resolution and also by the transform limit of the unchirped laser pulses. In our case, as we chirp at a rate of 17 MHz/ns with a detector integration time of 1 ns, a frequency resolution of 17 MHz is obtained. The resolution determined by the Fourier transform of the pulse shape is similar at approximately 10 MHz. The resolution in our system can be increased significantly to less than 1 MHz by chirping more slowly and using longer laser pulses, both of which can be achieved using the current laser system.

Finally, we note that there is also a fundamental limit to the spectral information that can be obtained from the gas, particularly for measurement of the bulk properties such as the speed of sound, which only occur on collisional timescales. CRBS carried out with laser pulse durations shorter than the collision time should be significantly different to the conventional CRBS spectra and should be carefully compared with conventional CRBS models before used for diagnostic methods in the a shorter pulse duration regime.

Chapter 6

Optical Stark deceleration - Theory

6.1 Introduction

In optical Stark deceleration (OSD) optical lattices are created by the interaction with the induced dipole force on polarisable species by intense optical fields which allows for trapping and controlling of their translational motion. In essence this method and its theoretical treatment is not very different to that presented in CRBS, with the main difference between the two lying in the fact that the densities used in OSD are orders of magnitude smaller than those in CRBS, hence collisions within the lattice sites are reduced and the trapped species' motion within the lattice can be treated individually rather than collectively.

Optical Stark deceleration is crucial to the sympathetic cooling scheme proposed by our group [183, 184] and has already demonstrated its capabilities in producing atomic argon beams of well-defined velocity and low energy spread for use in collisional studies [80]. In this chapter I will present the physics of optical Stark deceleration as well as the two different regimes by which it can be achieved.

6.2 The physics of optical Stark deceleration

Optical Stark deceleration uses optical fields that are far red detuned from any molecular dipole transition, so that the potential experienced by a polarisable particle is quasi-electrostatic, given by $U = -\frac{1}{4}\alpha_{\text{eff}}E^2$ as discussed in Section 3.5.1. The force on a particle in this potential is given by $F = -\nabla U$, hence it is strongly dependent on the gradient of the optical field. In order to maximise this gradient, we interfere two counter-propagating beams which produce a much steeper optical gradient than that resulting from a tightly fo-

cussed laser beam. The potential seen by the polarisable species is an interference pattern of the form

$$U(z,t) = -\frac{\alpha_{\text{eff}} E^2(t)}{2} \cos^2[qz - \Delta\omega t], \tag{6.1}$$

as we have shown in Section 3.5.1, where $\Delta\omega$ is the frequency difference between the two interfering beams and q is the difference of their wavevector. The force experienced by molecules in this potential is

$$F = -\nabla U = -\frac{\alpha_{\text{eff}} q E^2(t)}{2} \sin(qz - \Delta\omega t). \tag{6.2}$$

By manipulating the frequency difference $\Delta\omega$ between the two lattice beams using the laser system presented in Chapter 2, we can achieve efficient trapping and manipulation of the translational motion of the particles. Although the force experienced by the species is always the one shown in Eq. 6.2, OSD can be performed through two different mechanisms depending on whether the frequency difference is constant or chirped, as I will discuss in the next two sections.

6.3 Constant velocity optical Stark deceleration

Constant velocity OSD takes advantage of the fact that the trapped species undergo oscillatory motion within the lattice sites. For successful particle deceleration, the frequency difference between the two beams is chosen such that the lattice velocity v_L is smaller than the particle's velocity v_0. Then after a quarter oscillation within the lattice site the particle would be stationary with respect to the lattice, having been decelerated to a velocity equal to $v_0 - \Delta v$, where $\Delta v = |v_L - v_0|$. After an extra quarter-oscillation, having returned to its initial position within the lattice site, it would have lost an extra Δv in velocity. In total then, after a half-oscillation in the lattice site the particle would have reached a velocity equal to $v = v_0 - 2\Delta v$. Should the field be kept on, the particle would move in the opposite direction, gaining $+2\Delta v$ in velocity during a half-oscillation and thus returning to its initial velocity. In order to prevent that from occurring, in constant velocity OSD the optical fields are configured such that they switch off exactly after a half, or an odd integer multiple of half oscillations of the particles within the lattice sites (see Fig. 6.1).

For deeply trapped particles in the lattice site, where $\sin(qx - \Delta\omega t) \approx (qx - \Delta\omega t)$, the

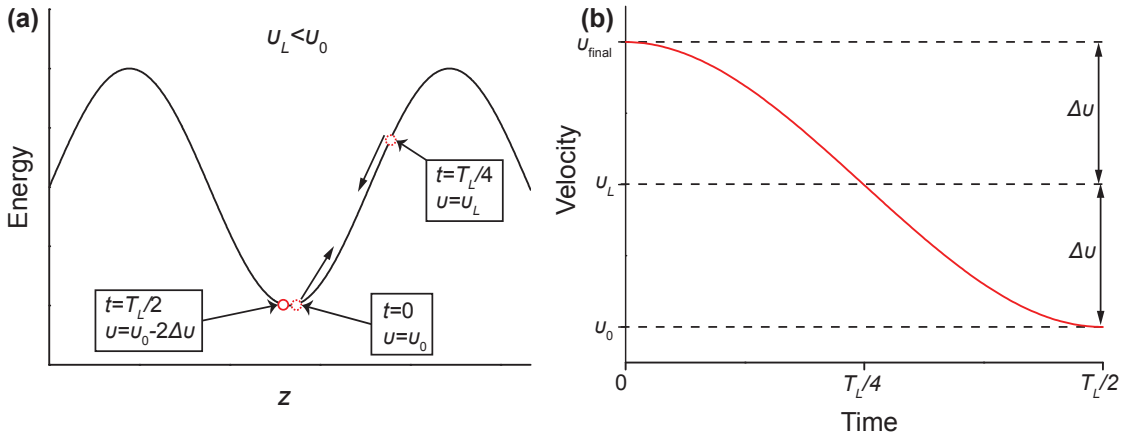

Figure 6.1: (a) Schematic of the oscillations undertaken by the particle within the lattice sites and (b) plot of the particles' velocity evolution after a half-period oscillation in the constant velocity optical Stark deceleration scheme.

force is, to a good approximation, harmonic and Eq. 6.2 then becomes

$$F \approx -\frac{\alpha_{\text{eff}} q E^2(t)}{2}(qz - \Delta\omega t), \tag{6.3}$$

and the oscillation period in the lattice frame would be [61]

$$T_{\text{L}} = \frac{2\pi}{q}\sqrt{\frac{\epsilon_0 cm}{\alpha_{\text{eff}} I}}, \tag{6.4}$$

where I is the intensity of one of the lattice beams, m is the particle's mass and ϵ_0 is the vacuum permittivity. Here, we assume that the particle starts its oscillation from the bottom of the trapping potential well. In life experiments, the trapped particles would be equidistributed across the potential well and hence only a small fraction of them would be efficiently decelerated. Another factor that needs to be taken into account when setting up constant velocity OSD is the minimum potential well depth required for successful particle deceleration, which should be equal to half the kinetic energy removed from the particle [61]. This requirement dictates a minimum for the intensity of the (equal in intensity) interfering beams of [137]

$$I_{\text{min}} = \frac{\epsilon_0 cm\Delta v_{\text{total}}^2}{8\alpha_{\text{eff}}}, \tag{6.5}$$

where m is the mass of the particle and $\Delta v_{\text{total}} = 2\Delta v$. This intensity is a theoretical minimum and in practice intensities up to twice that value have been used experimentally to accommodate for loss mechanisms such as radial motion (Section 6.4.1) within the lattice sites.

Constant velocity OSD has been successfully used in the past to slow nitric oxide (NO) and benzene (C_6H_6) molecules in a molecular jet in a backing gas of Xenon (95% by volume) [11, 137, 185].The molecules were introduced in the interaction region through a supersonic jet which was translationally cold (around 1.8 K), having a mean centre-of-mass velocity of approximately 400 m·s^{-1}. The lattice beams in the experiments were produced by two flashlamp pumped, injection seeded Q-switched Nd:YAG lasers whose frequency was tuned by varying their temperature while their relative frequency was constantly monitored on a spectrum analyser (a setup similar to the one used in early CRS [145] and CRBS [49, 146]). These lasers were able to deliver energies up to 350 mJ per pulse, with pulse durations below 15 ns and were focussed crossing at an angle of 167.5^o in the centre of the vacuum cell intersecting with a supersonic jet. Local intensities of order 10^{11} Wcm^{-2} were achieved with measured $1/e^2$ spotsizes of 60 μm.

Due to the technically challenging task of rapidly switching the optical lattice off, in the first experiment carried out using constant velocity OSD, NO molecules were decelerated from an initial velocity of 400 ms^{-1} to 270 ms^{-1} (representing a velocity loss of 32.5%) and accelerated to 500 ms^{-1}, with lattice durations of 5.8 ns [11]. Benzene (C_6H_6) was more efficiently decelerated from an initial velocity of 380 ms^{-1} down to 191 ms^{-1} representing a velocity loss of 49.7% [137]. In both cases, the decelerated particles underwent more than half an oscillation and were not brought to rest. To address this issue, a fast Pockel's cell was used to optically chop one of the pulses, allowing for C_6H_6 molecules to be brought to rest [185].

Although this method did produce some good results, it has some drawbacks. To begin with, relying on the thermal stability of the seed lasers is not experimentally ideal, as was the case with CRBS (Section 5.2). More importantly, the required fast switch off of the lattice beams is technically demanding and when that does not occur, the desired final velocity is not achieved. The most serious drawback of this implementation of OSD is that the velocity spread of the decelerated species is fundamentally limited to be equal at best to the initial velocity spread, rendering the method not suitable for collisional experiments where high velocity resolution is required. To overcome these drawbacks, a scheme for achieving optical Stark deceleration which uses chirped lattices has been proposed, which I will discuss in the following section.

6.4 Chirped optical Stark deceleration

In order to overcome the drawbacks of constant velocity OSD described in the previous section, theoretical studies on the use of chirped lattices to accelerate or decelerate atomic and molecular species have been undertaken [186, 187], while part of the work carried out for this thesis was towards the experimental implementation of this scheme. Chirped OSD does not rely on the oscillatory motion of the trapped particles and thus allows for much slower switching of the interacting fields and longer pulse durations (20-1000 ns). Although the chirped OSD scheme does not require such high intensities as the constant velocity scheme, relatively high energies per pulse are still needed due to the longer pulse durations (up to 500 mJ per pulse). The major advantage of the chirped OSD scheme though, is that it eliminates the fundamental limit on the velocity spread of the resulting decelerated species, thus rendering this method capable of producing well defined particle ensembles for use in high resolution collisional studies.

In order to study the particles' motion in such chirped lattices, we need to modify the expression for the potential that would be seen by the particle in order to accommodate for the sweeping frequency of one of the two beams with respect to the other. The potential in Eq. 6.1 becomes

$$U(z,t) = -\frac{\alpha_{\text{eff}} E^2(t)}{2} \cos^2[qz - (\omega_0 t - 1/2\beta t^2)], \tag{6.6}$$

where ω_0 is the initial frequency difference between the two lattice beams and $\beta = \Delta\omega/\Delta t$ is the chirp rate, Δt is the duration of the chirp (usually equal to the pulse duration) and $\Delta\omega = \omega_0 - \omega_{\text{f}}$, with ω_{f} being the final frequency difference. Depending on whether β has got a positive or negative sign, the resulting chirped lattice would be accelerating or decelerating respectively. In order to study the effect of the potential in Eq. 6.6 on the molecules interacting with it, we start with the equation of motion for a particle in this potential, given by [186]

$$\frac{d^2 z}{dt^2} = -\alpha(t) \sin[(qz + 1/2\beta t^2 - \omega_0 t)], \tag{6.7}$$

where $\alpha(t) = -1/2\alpha_{\text{eff}} q E^2(t)/m$ is the maximum force per unit mass supplied by the lattice. Of importance to our study are the trajectories of the molecules which are perturbed by the presence of the lattice and hence their motion must be studied in the reference

frame of the decelerating lattice. Equation 6.7 in this decelerating reference then becomes

$$\frac{d^2\theta}{dT^2} = 2 - \frac{2\alpha q}{dT^2}, \tag{6.8}$$

where $\theta = Z - T^2 - C$ is the phase of the particle with respect to the lattice, $C = \omega_0 T$ and where we have introduced the dimensional temporal and spatial variables $T = \sqrt{\beta/2t}$ and $Z = qz$ respectively. From this equation of motion then, we can now derive particle trajectories within the lattice in the velocity phase space $[\eta, \theta]$, where $\eta = d\theta/dt$. We now have a system of equations [186]

$$\frac{d\eta}{dT} = 2 - \frac{2\alpha q}{dT^2}, \tag{6.9a}$$

$$\eta = \frac{d\theta}{dt}. \tag{6.9b}$$

If we set each equal to zero, we find the critical points of the system at $\eta = 0$ and $\sin\theta = -\psi$, where $\psi = \beta/\alpha q$ is a dimensionless figure of merit of the ratio of the chirp rate to the lattice intensity. Linear stability analysis of Eqns. 6.9a and 6.9b reveals stable equilibrium points at $[\eta, \theta] = [2n\pi - \sin^{-1}\psi, 0]$ and unstable equilibrium points at $[\eta, \theta] = [(2n-1)\pi - \sin^{-1}\psi, 0]$, where n is an integer. In the reference frame of the decelerating lattice, the potential must also be changed to the one shown on Eq. 6.6 and would now be $U(\theta) = -\int (m/q^2) d^2\theta/dt^2 d\theta$. From Eqns. 6.9 this can be evaluated to be

$$U(\theta) = \frac{2}{\psi} cos\theta - 2\theta. \tag{6.10}$$

The depth of a potential well is defined as the difference between the bottom of the well and the nearest peak which represents the nearest unstable equilibrium point. This depth is given by:

$$\Delta U = \frac{m\alpha}{q}[2cos(\sin^{-1}\psi) - \psi(\pi - 2\sin^{-1}\psi)]. \tag{6.11}$$

Since mathematically $|\sin(x)| \leq 1$, it follows from Eq. 6.11 that no potential well can exist for $\psi > 1$, giving us a very important condition for optical Stark deceleration:

$$|\psi| \leq 1 \Leftrightarrow \left|\frac{\beta}{\alpha q}\right| \leq 1. \tag{6.12}$$

Physically this result means that when the chirp rate is much higher than the maximum

force per unit mass supplied to the particle by the optical lattice there can be no potential well. A mechanical analogue to this result would be the gearing system of a car, where the trap potential is equivalent to the torque supplied by the gearing, while the velocity remains the same in both systems. The well depth is at a maximum ΔU_{max} for $\psi = 0$, i.e. when there is no chirp and the lattice is either stationary or moving at a constant velocity. Figure 6.2 is a plot of the potential well for three values of $\psi = 0.25, 0.5, 0.75$ with respective well depths of $0.64\Delta U_{max}, 0.36\Delta U_{max}$ and $0.23\Delta U_{max}$. It is apparent then that the deeper potential well represented by a ψ value of 0.25, would trap and decelerate a larger proportion of molecules than the one represented by a well with $\psi = 0.75$. In physical terms, this result suggests that the intensity of the beams has to be well balanced with respect to the chirping rate, for efficient trapping and deceleration to occur.

Given that the motion of the particles in the lattice frame can be numerically represented by Eqns. 6.9, it is useful to map out the trajectories of particles around the lattice

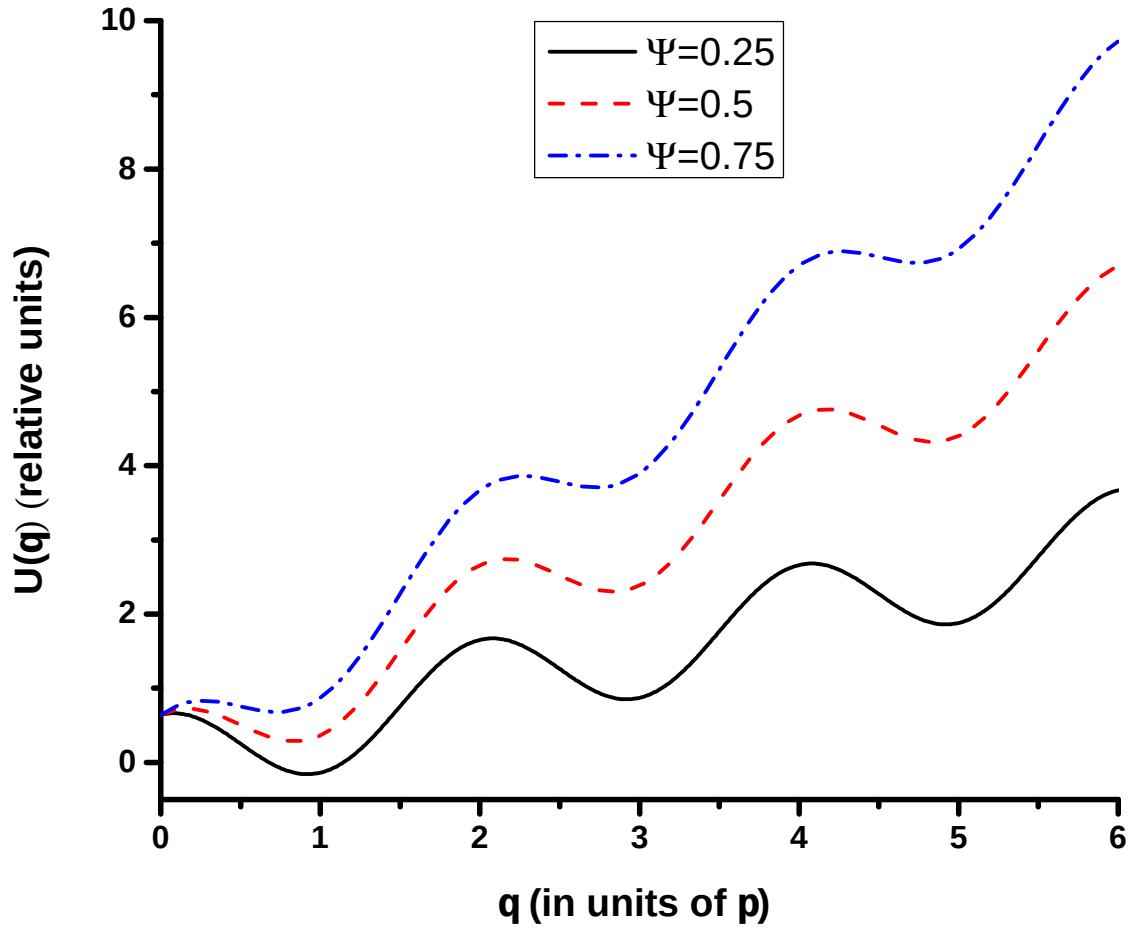

Figure 6.2: Chirped lattice potentials in the decelerated reference frame. The shown curves were calculated from eq. 6.10. It can clearly be observed how the well depths become shallower with increasing values of ψ.

sites in phase space plots, with respect to phase velocity η and phase position θ. Two of these phase space plots, for two different values of ψ, are shown in Fig. 6.3, representing the trajectories of 10 particles in the lattice frame. Here, the x-axis is the relative phase θ of the particle with respect to the lattice, while the y-axis is the dimensionless phase velocity η which can be related to the velocity in the lab frame from the equation $v = \eta\frac{\sqrt{\beta/2}}{q}$. The almost closed, tear drop shaped trajectory, maps out the boundary between the trapped and untrapped particles from the lattice. Particles within these separatrices remain trapped as the lattice decelerates, while following orbits of the local equilibrium point, assuming no collisions between the particles take place. The rest of the particles have their velocity perturbed, but remain untrapped for the duration the lattice is on.

The maximum velocity a particle can have and still be efficiently trapped and decelerated is phase and velocity dependent and is given by [187]

$$v_{\mathrm{c}}(\theta) = V[\cos\theta - cos(\pi - \sin^{-1}\psi) + \psi(\theta + \pi + \sin^{-1}\psi)], \tag{6.13}$$

where $V = 2\frac{\sqrt{\beta/\psi}}{q}$.

Another important factor to be taken into account when designing experiments using the chirped OSD method, is the capture efficiency κ of the particles. This is given by the number of particles which are overlapping the phase space plot as shown in Fig. 6.3. These particles are initially in thermal equilibrium in the interaction region, with a velocity distribution defined by the Maxwell-Boltzmann distribution for the initial temperature they are at. The fraction of molecules that are captured and decelerated by the lattice is given by

$$\kappa = \frac{\int_{z_1}^{z_2}\int_{v(z_1)}^{v(z_2)}\sqrt{\frac{m}{2\pi k_{\mathrm{B}}T}}e^{-mv^2/2k_{\mathrm{B}}T}dvdz}{\int_0^{\lambda/2}\int_{-\infty}^{\infty}\sqrt{\frac{m}{2\pi k_B T}}e^{-mv^2/2k_B T}dvdz} \tag{6.14}$$

where z_1 and z_2 are the two critical points of eq. 6.13, while $v(z_1)$ and $v(z_2)$ are the respective velocities of the particles at these points. Figure 6.4 is a plot of the calculated capture efficiency κ with respect to the ψ value, for H_2 at a mean temperature of 100 mK. These calculated values represent a maximum, since molecules would escape the lattice sites in the radial direction due to the decrease in lattice intensity/well depth. Nevertheless, it does suggest an optimal experimental situation for low values of the ψ parameter, along with Fig. 6.5 that represents the capture efficiency κ with respect to the initial molecular temperature for H_2, for a range of values of the ψ parameter. It can be observed that the

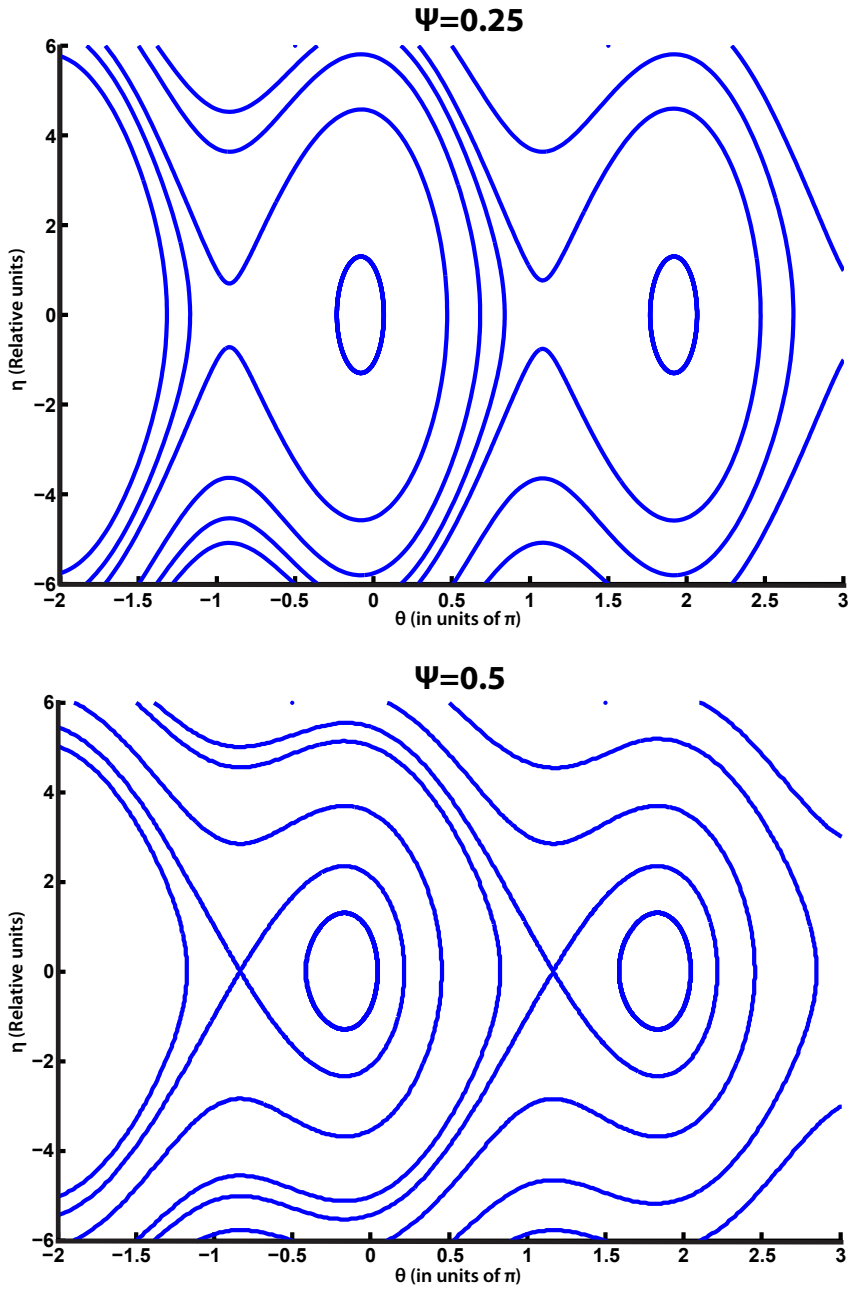

Figure 6.3: Phase space diagrams for two different values of ψ. It can be observed that the almost closed, tear drop shaped area where the particles are efficiently trapped and decelerated is larger for a smaller value of ψ, suggesting a more efficient mode of operation for decelerating experiments. The particles that are eventually trapped start with an initial velocity equal to that of the lattice, while they are relative close to the lattice site in order to remain confined for the lattice duration. The rest of the particles are simply perturbed by the lattice, with the degree of perturbation depending on how close they pass to the lattice sites centres.

capture efficiency remains almost constant, until the width of the velocity distribution of the molecules becomes larger than the velocity width of the separatrix of the lattice site.

Although both Figs. 6.4 and 6.5 suggest that ideally one should operate deceleration experiments at a low value of the ψ parameter, since a larger number of molecules are

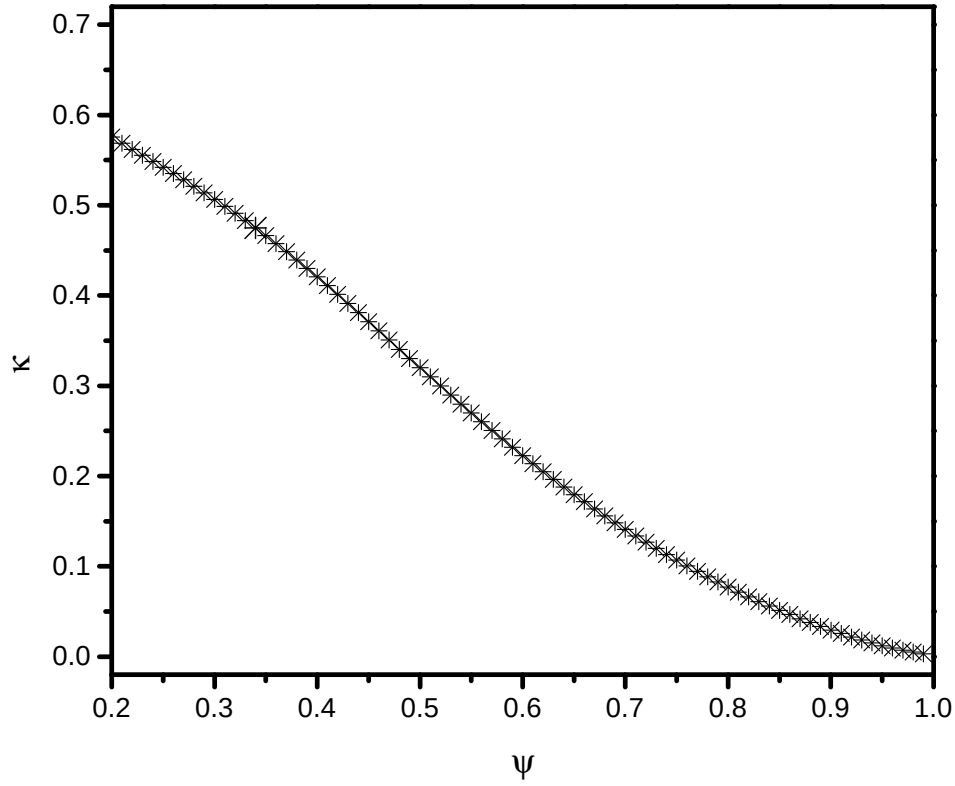

Figure 6.4: Capture efficiency κ with respect to the ψ value, for H_2 at a central temperature of 100 mK.

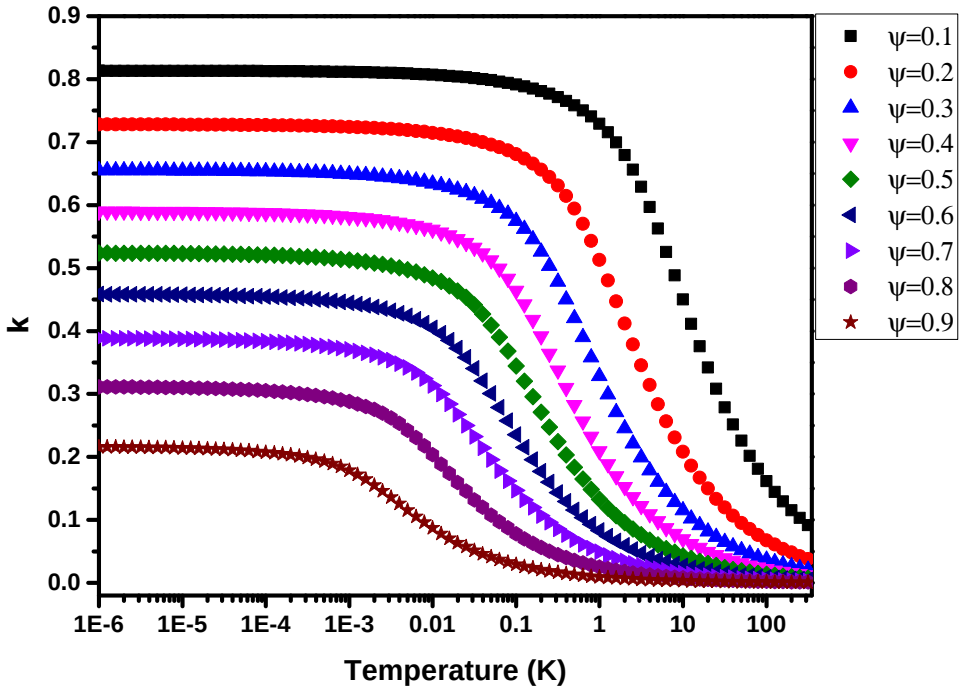

Figure 6.5: Capture efficiency κ with respect to temperature, for a range of ψ values.

trapped and decelerated, one also needs to take into consideration the effect of ψ on the resultant width of the velocity distribution of the decelerated molecular ensemble. The velocity width is dependent on the well depth ΔU as defined in Eq. 6.11, so that the

maximum velocity spread of the decelerated particles is given by

$$\Delta v = 2\sqrt{\frac{2\Delta U}{m}}. \tag{6.15}$$

Equation 6.15 suggests that in order for a narrow velocity distribution of the molecular ensemble to be obtained at the end of the deceleration process, one has to use low values for the lattice potential ΔU. This result has to be used in combination with what was suggested from Figs. 6.4 and 6.5, where high optical potentials lead to an increase in the capture efficiency. These findings imply that there should be a trade-off between the fraction of molecules that could be trapped and decelerated, and the resultant velocity spread.

6.4.1 Radial motion in lattice sites

Particles trapped in chirped lattices undergo radial oscillatory motion within the lattice sites, due to the radial intensity gradient in a Gaussian beam, as with constant velocity lattices. These intensity gradients are much smaller than the ones in the axial direction, but over long lattice durations can lead to significant divergence of the resulting decelerated molecular beam. The potential in the radial direction is given by

$$U(r) = U_0 e^{-\frac{2r^2}{w_0^2}}, \tag{6.16}$$

where U_0 is the peak well depth given by $U_0 = \frac{2\alpha_{eff} I_0}{\epsilon_0 c}$, r is the radial coordinate and w_0 is the $1/e^2$ radius of the beam. The force then seen by a particle in this potential is:

$$F(r) = -\nabla U(r) = \frac{4rU_0}{\omega_0^2} e^{-\frac{2r^2}{w_0^2}}. \tag{6.17}$$

Assuming a low temperature of the decelerated gas particles with respect to the depth of the lattice potential, and that the particles oscillate in the harmonic part of the potential, we can use a second order Taylor expansion in order to rewrite eq. 6.17 as $F(r) = -U_0 r/w_0^2$. The period of oscillation within the lattice sites is then:

$$T = 2\pi\sqrt{\frac{mw_0^2}{U_0}}. \tag{6.18}$$

Considering a lattice with intensity of 5×10^{13} Wm^{-2}, $1/e^{-2}$ radius of 100 μm, for the case of H_2 molecules with $\alpha_{\text{stat}} = 8.7565\times10^{-41}$ Cm^{2}V^{-1}, then from Eq. 6.18 we get an oscillation period of $T \approx 19.9$ μs, which is some orders of magnitude longer than the duration of the deceleration pulse, thus validating the quasi 1-dimensional model approximation we use in our simulations. The maximum force that can be experienced by a particle in the radial direction can be found by simply letting $\nabla F(r) = 0$. The maximum is found at $r = w_0/2$, where $\nabla F(w_0/2) = \frac{2U_0}{w_0 e^{-1/2}}$.

6.5 Simulating optical Stark deceleration

Although the model presented in Section 6.4 is useful in gaining physical insight into the optical Stark deceleration process, it is not very useful in accurately simulating deceleration experiments, due to the fact that it does not account for intensity variation over the duration of the lattice. In order to simulate optical Stark deceleration with experimental lattice parameters, we employ a Monte Carlo method where the trajectories and final velocities are calculated individually for each particle interacting with the lattice. The initial positions and velocities of the particles are assigned based on what is expected from the experiment. By performing these calculations on a large number of particles, we can obtain useful and reliable statistics about the final velocity distribution after the deceleration process.

Assuming no collisions take place between the interacting particles, through the equation of motion given by Eq. 6.8 we can calculate the trajectory of a particle over the duration of the decelerating lattice, for a given initial position and velocity. To do this, Eq. 6.8 must be first rewritten as

$$\frac{dv(x,t)}{dt} = -F_0 \sin(qv(x,t) - \phi(t)), \tag{6.19a}$$

$$\frac{dx}{dt} = v(x,t), \tag{6.19b}$$

where $F_0 = \alpha q I(t)/(m\epsilon_0 c)$ and $\phi(t)$ is the relative phase between the two lattice beams. The Eqns. 6.19 can then be solved through a fourth order Runge-Kutta method for realistic temporal intensity profiles and frequency chirps. Programmatically, the code performs this task through the ODE45 solver in Matlab for a large number of particles (>20000). The interacting particles are assigned an initial x, y, z coordinate within the lattice and at each

time step within the simulation the potential experienced by each particle is derived from the instantaneous intensity $I(t)$ and phase $\phi(t)$, both of which can be defined either from ideal or experimental intensity and chirp profiles, respectively. This code was originally implemented in [62] and further improved in [61], where the lattice potential was extended to three dimensions rather than one.

In order to demonstrate the influence of intensity and chirp rate, i.e. the parameter ψ, in the deceleration process, I modified the original code to obtain simulation data for decelerated H_2 molecules with an initial translational velocity of 250 ms^{-1} and velocity width determined by the Boltzmann distribution for molecules at a temperature of 1 K. The intensity profiles that were used were experimental ones from the laser system described in Chapter 2, while the linear, decelerating chirp profiles were ideal ones starting at an initial chirp rate defined by the user at the beginning of the pulse and always ending at a frequency difference of 0 MHz. Figure 6.6 shows a plot of the initial velocity distribution of 25000 H_2 molecules, as well as the simulated deceleration of these molecules for two chirp rates, at various intensities. The initial velocity of the lattice that corresponds to these chirp rates is calculated from equation 4.2.

It is clear from these plots that the more the initial velocity of the lattice matches the mean velocity of the molecular ensemble, the more efficient the deceleration process becomes, resulting in more molecules being decelerated with a narrower velocity width. They also confirm what is expected from the chirped optical Stark deceleration scheme, since we can end up with narrower velocity distributions than the ones we started with, overcoming the constraint posed in constant velocity OSD, as discussed in Section 6.3. Finally, by increasing the intensity we end up with most of the molecules decelerated but with a much wider and not a well-defined velocity distribution. Hence, as discussed in section 6.4 concerning the ψ values, there has to be a trade-off between the intensity and the chirp rate to be used, in order to end up with a narrow velocity width molecular ensemble.

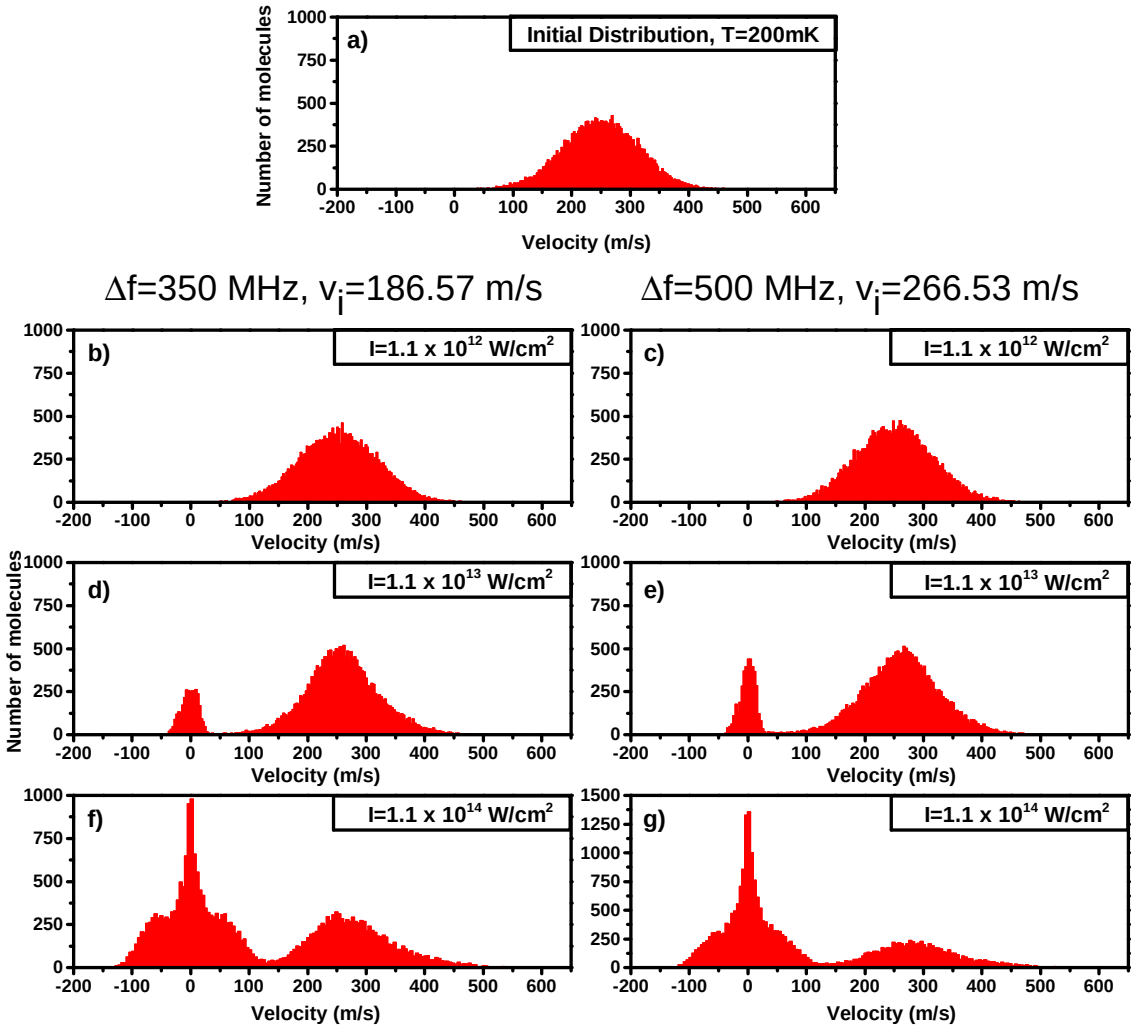

Figure 6.6: Figure a): Initial velocity distribution of 25000 H_2 molecules, corresponding to a forward velocity of 200 mK. Figures b), d), f): simulated deceleration for three intensity values (I) and an initial frequency difference of the beams of 350 MHz, corresponding to an initial velocity (v_i) of the lattice of 186.57 ms^{-1}. Figures c), e), g): simulated deceleration for three intensity values (I) and an initial frequency difference of the beams of 500 MHz, corresponding to an initial velocity (v_i) of the lattice of 266.53 ms^{-1}. In all of the plots the y axis represents the number of molecules.

In order to obtain a more clear view of the different operating regimes, we extended these calculations to a wide range of intensities and chirp rates, which are presented in Fig. 6.7. As was previously the case, the optimum intensity drops as the chirp rate increases. Depending on how narrow we want the resultant velocity distribution, we have to accordingly adjust the operating intensity of the lattice beams, as well as the chirp rate of the lattice.

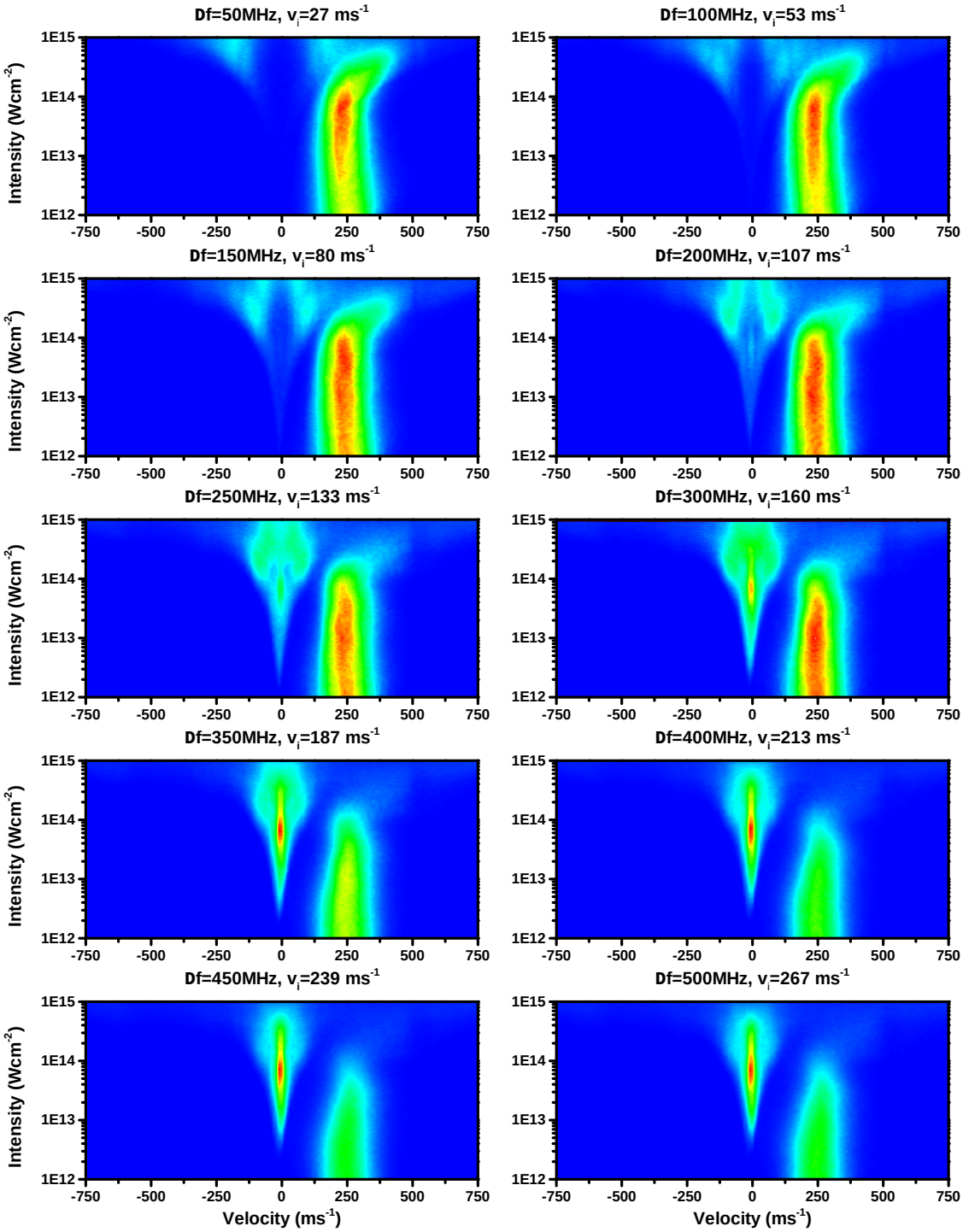

Figure 6.7: Plots of the simulations for 25000 H_2 molecules, for the conditions described in Section 6.5. Red represents a number of molecules $\sim 2500-3000$, yellow represents a number of molecules $\sim 2000-2500$, green represents a number of molecules $\sim 1000-2000$ while blue is used to represent a lower number of molecules ($\sim 0-1000$).

6.6 Conclusions

In this chapter I presented an overview of the theory behind optical Stark deceleration as well as the two main ways by which it can be achieved using constant velocity lattices and chirped velocity lattices. Simulations of the chirped optical Stark deceleration scheme were presented for H_2, for conditions meeting those of the experiment. Part of the experimental work carried out for the purposes of this thesis was about achieving chirped optical Stark deceleration, which will be discussed in the next chapter.

Chapter 7

Optical Stark deceleration - Experiment

7.1 Introduction

As part of the sympathetic cooling scheme proposed by our group [183], molecules need to be decelerated to low enough velocity to be optically trapped. This has to be implemented through OSD so that decelerated H_2 molecules could then be co-trapped and further cooled by collisions with argon atoms, in a dipole trap. Ground state H_2 was selected because of its importance in the astronomical and chemical scientific communities as well as because it cannot be cavity cooled or trapped by other means.

In this chapter I will describe the steps taken and the apparatus used for the development of a detection scheme which can be used to tag the H_2 molecules that are decelerated via chirped OSD. Through this detection scheme, background free measurements of the decelerated H_2 molecules can be performed in future experimental demonstrations of chirped OSD.

7.1.1 Atomic optical Stark acceleration of Ar*

As a proof of principle experiment, previous members of our group have already shown that chirped optical Stark acceleration can indeed be used as a particle accelerator technique, by accelerating Ar* atoms from a magneto-optical trap (MOT), initially at rest, to velocities which they could control at will [80]. Deceleration only requires a change in the sign of the voltage applied to the EOM in our microchip laser.

In their experiment, a schematic of which is shown in Fig. 7.1, the IR laser beams

Figure 7.1: Schematic of the experimental setup used for optical Stark acceleration of Ar*. The two IR beams creating the optical lattice are shone onto the Ar* MOT. The accelerated packet is imaged by an EMCCD camera. (image taken from [80]).

created by the laser system presented in Chapter 2 were used in a counterpropagating geometry on the Ar* MOT, which contained Ar* atoms at rest ($T = 77\mu$K). By employing a sinusoidally chirped accelerating lattice, they were able to achieve final velocities for the accelerated Ar* packet of 191 ms^{-1}, with velocity spreads of $6 - 11$ ms^{-1}. Over the duration of 70 ns that their pulse was on, they produced an acceleration of 10^8g while up to 50% of the Ar* atoms in the MOT were trapped and accelerated.

In order for them to able to detect the interaction of the chirped lattice with the MOT, they used an electron-multiplier CCD (EMCCD) camera which could image the induced fluorescence from an 811.53 nm beam. Also, an ionisation beam at 532 nm was used for time-of-flight (TOF) measurements to be able to be carried out, by the use of a multichannel-plate (MCP) detector.

7.2 Realising chirped optical Stark deceleration of H_2

The realisation of chirped optical Stark deceleration (OSD), does not have to be very different to the experimental setup that was used for constant velocity OSD, shown in Fig. 7.2. In the constant velocity lattice OSD experiment, molecules from a pulsed molecular source were captured by the optical lattice formed by two IR beams in a counter-propagating

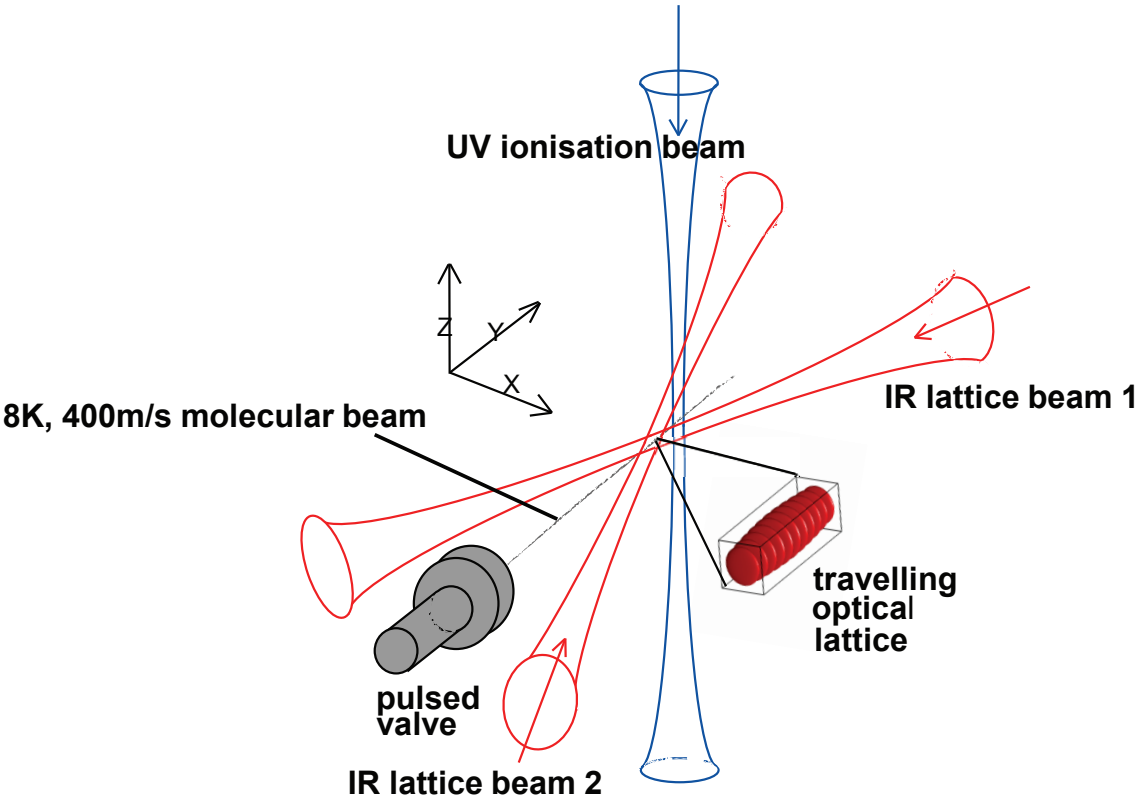

Figure 7.2: Schematic of the experimental setup used for constant velocity OSD. Molecules from the supersonic expansion of a pulsed molecular beam are captured by the constant velocity lattice and ionised by means of REMPI and detected on a TOF mass spectrometer (image taken from [11]).

geometry. After deceleration, the molecules were detected via ionisation from a UV beam using resonantly enhanced multiphoton ionisation (REMPI). The resulting molecular ions were detected on a TOF mass spectrometer where their velocity could be determined [11].

In order for us to implement the chirped optical lattice OSD for ground $X^1\Sigma_g^+$ electronic state H_2, we also need to add to our setup a molecular source of H_2 (Section 7.4.1) which provides with transversely cold H_2 molecules which can then be trapped and decelerated by chirped lattices where the initial lattice velocity is equal to the initial mean velocity of the molecular species. Due to the fact that the interaction region of the deceleration process is much smaller in size than the molecular beam provided by the source we are using (~ 100 μm in comparison to ~ 0.5 cm), we implemented a detection scheme based on stimulated Raman pumping (SRP) in order to promote from the $X^1\Sigma_g^+$ v= 0, J= 1 state to the higher $X^1\Sigma_g^+$ v= 1, J= 1 ro-vibrational state only the H_2 molecules that have interacted with the decelerating lattice (Section 7.12). From this higher state we can ionise the decelerated molecules by using a $(2+1)$ REMPI process (Section 7.2.2). The created ions will again be detected by a microchannel plate (MCP) detector (Appendix A).

7.2.1 Molecular tagging through stimulated Raman pumping.

The prerequisite of detecting only the H_2 molecules that have interacted with the lattice, dictates that the tagging scheme to be followed would certainly need to make use of the 1064 nm radiation provided by the IR beams. Through this scheme the interacting molecules, initially residing at the $X^1\Sigma_g^+$ v= 0, J= 1 ro-vibrational state, should be promoted to a higher ro-vibrational state, still on the ground $X^1\Sigma_g^+$ electronic state though, from where they could be ionised via REMPI detection. The scheme that was chosen to perform this task was stimulated Raman pumping (SRP). SRP is a well-established technique which has been extensively used to provide with H_2 molecules at specific ro-vibrational states [188, 189, 190].

Unlike Rayleigh and Brillouin scattering which can be seen as being the result of the *macroscopic* motion of atoms and molecules, Raman scattering involves their internal energy structure, and occurs because of transitions between the different molecular rotational and vibrational levels. Raman scattering as a process involves the absorption of a photon by the molecule, its transition to a *virtual* state and its fast decay to a different energy state than the one it started from. Through the introduction of the virtual state, Rayleigh scattering can also be seen as a special case of Raman scattering, where simply the molecule returns to the state it started from.

Raman scattering in general can easily be understood with the use of energy diagrams, such as the ones shown in Fig. 7.3. Depending on whether the final energy state of the molecule is higher or lower than the initial one, the scattered photons can have lower energies compared to the illuminating photons, in which case the process is called Stokes Raman scattering, or higher energies, in which case the process is called anti-Stokes Raman scattering. The intensity of the resulting Stokes lines is typically much larger than the anti-Stokes ones, since in thermal equilibrium the population of the excited state $|e\rangle$ is smaller than the population in the state $|g\rangle$ by the Boltzmann factor $exp(-\hbar\omega_{\mathrm{eg}}/kT)$, where ω_{eg} is the frequency difference between the states textbf$|g\rangle$ and textbf$|e\rangle$[119]. It is rather obvious from the nature of the process that Raman scattering constitutes an inelastic scattering process.

The virtual state simply denotes an energy value which doesn't coincide with any of the rotational or vibrational levels of the molecules. In this case the process is called *non-resonant* Raman scattering. If the virtual state does indeed coincide with a rota-

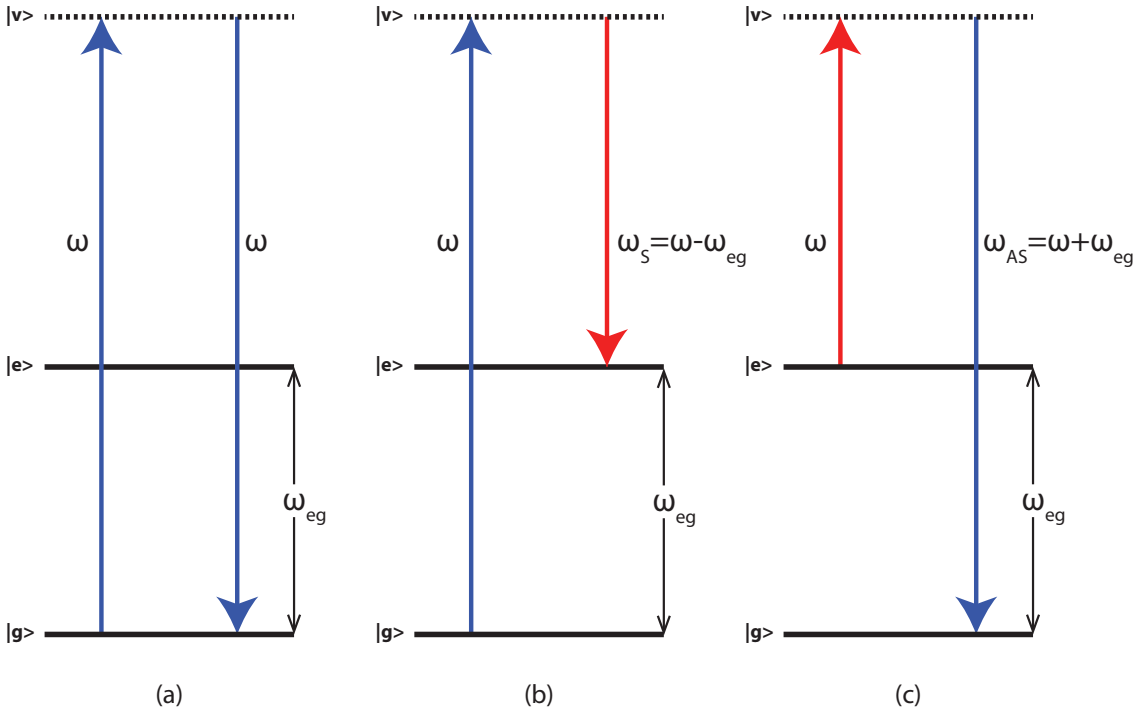

Figure 7.3: Energy diagram depicting the Rayleigh (a), Stokes-Raman (b) and anti-Stokes-Raman scattering processes. In $|g\rangle$,$|e\rangle$ and $|v\rangle$ are noted the ground, excited and virtual states, respectively.

tional or vibrational level, then the process is called *resonant*. The spectroscopic importance though of Raman scattering lies in the fact that it allows transitions which are quantum-mechanically forbidden for single-photon spectroscopical methods, to be accessed and studied. Since Raman scattering consists a two photon process, selection rules for the ro-vibrational transitions dictate that $\Delta v = \pm 1$ and $\Delta J = 0, \pm 2$, since angular momentum has to be conserved.

The most usual Raman scattering techniques are stimulated Raman scattering (SRS) and coherent anti-Stokes Raman scattering (CARS). In SRS two laser beams are being exploited, called the *pump* and the *probe*, whose frequency difference matches the energy difference between two specific molecular ro-vibrational states [191, 192]. The pump will then undergo SRS loss, while the probe will experience SRS gain, resulting in the SRS signal. In CARS, a second pump photon is being exploited from the upper ro-vibrational state, in order to promote the molecule to an upper virtual state, from which the molecule will decay emitting a *signal* photon whose frequency ω_s will be given by $\omega_s = 2\omega_{\text{pump}} - \omega_{\text{probe}}$. The process is called coherent due to the coherent nature of the interaction which is driven by three coherent beams, resulting in a fourth beam, constituting CARS a four wave mixing process. Figure 7.4 presents energy level diagrams of the two processes. In SRP,

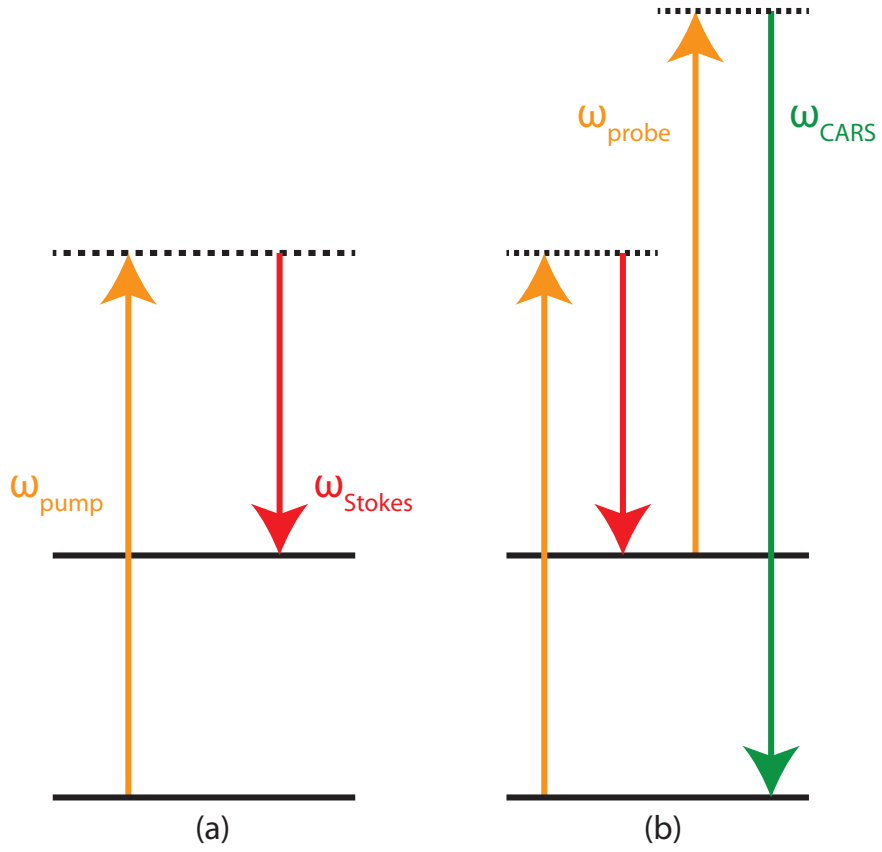

Figure 7.4: Energy level diagrams presenting (a) stimulated Raman scattering and stimulated Raman pumping and (b) coherent anti-Stokes Raman scattering.

similarly to SRS, only two photons are exploited, one from the pump and one from the probe. This way molecules can be promoted from a lower ro-vibrational level to a higher one. The SRP wavelengths can be established by either CARS or SRS, while detection of the final ro-vibrational level can be performed through REMPI.

Since two different transitions from the $X^1\Sigma_g^+$ v= 0, J= 1 H_2 level can occur (the $X^1\Sigma_g^+$ v = 1 , J = 1 $\longleftarrow$ $X^1\Sigma_g^+$ v = 0 , J = 1 and the $X^1\Sigma_g^+$ v = 1 , J = 3 $\longleftarrow$ $X^1\Sigma_g^+$ v = 0 , J = 1), it is important to decide which one to exploit, based on the efficiency of the process. This efficiency is determined by the Placzek-Teller coefficients which show that "the Q branch polarisability [...] is determined both by the mean and the anisotropy of the derived polarisability, while for the S and O branches it is determined simply by the anisotropy. This would indicate a Q branch response that is much stronger than that of the S and O branches" [193]. In our scheme this would imply that the Q branch $X^1\Sigma_g^+$ v= 1, J= 1$\longleftarrow$ $X^1\Sigma_g^+$ v= 0, J= 1 transition would be stronger than the S branch $X^1\Sigma_g^+$ v= 1, J= 3$\longleftarrow$ $X^1\Sigma_g^+$ v= 0, J= 1 transition and should thus be preferred. The O and S branches refer to the Δv= 1, ΔJ= -2 and Δv= 1, ΔJ= $+2$ transitions, respectively, while

the Q branch refers to the Δv= 1, ΔJ= 0 transitions.

The $X^1\Sigma_g^+$ v= 0, J= 1 level has got an energy difference equal to 4155.25 cm^{-1} from the $X^1\Sigma_g^+$ v= 1, J= 1 level [194]. In our detection scheme, we will be establishing the SRP pump wavelength through CARS. SRS could be used for the determination of the SRP wavelength as well but, since we are not expecting to saturate the transition, the resulting SRS pump loss and SRS probe gain would be small and thus hard to measure. Since the probe beam in this SRP/CARS implementation is going to be provided by one of the 1064 nm (= 9398.5 cm^{-1}) beams of our laser system, a beam having a wavelength of 4155.25 $cm^{-1} + 9398.5$ $cm^{-1} = 13553.75$ $cm^{-1} = 737.8$ nm should be used as the pump beam. These wavelengths are easily achieved by a dye laser. The CARS process would then result in a signal beam of wavelength equal to 2×13553.75 $cm^{-1} - 9398.5$ $cm^{-1} =$ 17709 $cm^{-1} = 564.68$ nm. There would be no physical reason preventing us from using the 1064 nm beam as the pump beam instead of the probe. That would though require the use of a 1907.21 nm beam as the probe; these wavelengths though are not easily achievable.

7.2.2 Molecular ro-vibrational state detection through REMPI

Resonantly enhanced multiphoton ionisation (REMPI) is an $(n+m)$ multiphoton absorption and further ionisation technique where the molecule to be detected, initially in its electronic ground state, absorbs n photons to reach an excited electronic state and furthermore m photons which ionise it. The spectral profile is obtained by counting the resultant photoelectrons or ions or both, with respect to the excitation wavelength. Figure 7.5(a) is an energy diagram schematic of a (2+1) REMPI process.

Although the cross-sections for two and three photon absorption are far smaller to the ones for single photon absorption (representative respective values of 10^{-50} cm^4s^{-1} and 10^{-84} cm^4s^{-1} in comparison to 10^{-17} cm^4s^{-1} for single photon absorption [196]) intense laser sources allow saturation of these transitions. Furthermore, REMPI has allowed for transitions which would only be accessible with vacuum ultraviolet (VUV) wavelengths, to be explored with much less technically demanding and commercially available wavelengths. Although it is not a necessity for the multiphoton ionisation process to be successful, it is also noteworthy that the process is greatly enhanced when the first absorption step leads to an exited state rather than a virtual intermediate state (hence the technique is called resonantly enhanced MPI and not simply MPI). REMPI was demonstrated for the first

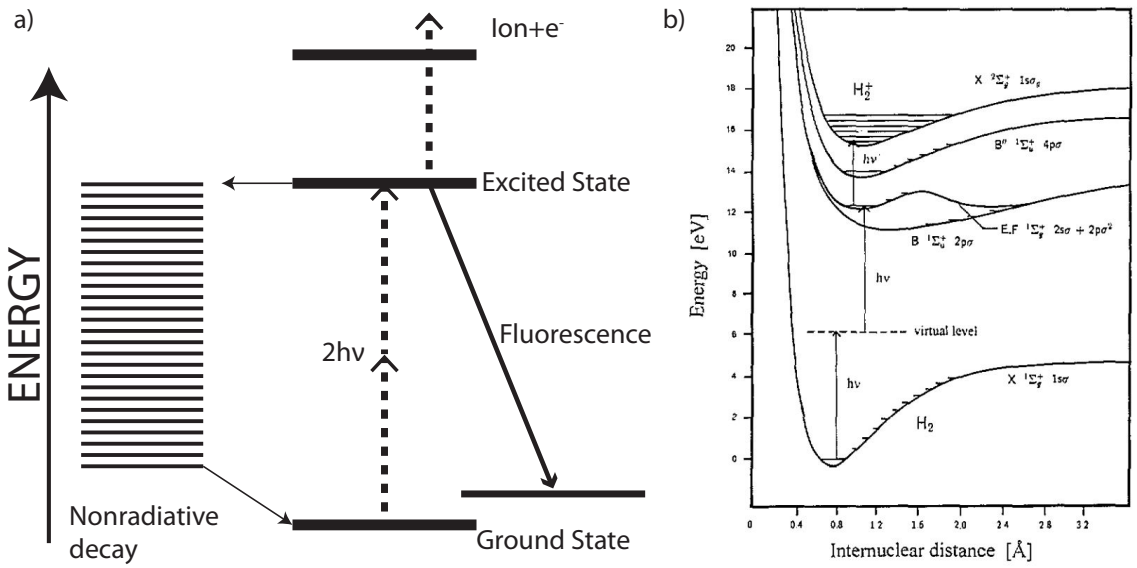

Figure 7.5: a) Schematic of a typical 2+1 REMPI process. The competing processes, intramolecular relaxation and fluorescence, which deplete the excited state population and reduce the ion yield are also shown. b) Potential energy curves for some electronic states of H_2 and H_2^+. The excitation and ionisation steps for the (2+1) REMPI process that will be used in the chirped OSD detection scheme for H_2 are shown (image taken from [195]).

time in stable NO radicals [197] and molecular iodine [198] in 1975. Very good review articles on the technique can be found in [196] and [199].

In order for the REMPI wavelengths of H_2 to be established, the output of a pulsed, commercial dye laser[1] was added to our experimental setup. This is pumped by ≈ 400 mJ/pulse provided by a pulsed commercial 532 nm laser[2]. The third harmonic generation can provide up to 6 mJ per pulse in the wavelength region between $\approx 200 - 220$ nm.

7.3 Calibration of laser wavelengths

7.3.1 Detecting H_2 REMPI in a test cell

Before directly measuring the REMPI wavelength in the molecular chamber used for deceleration, REMPI measurements were performed on a test cell as the one shown in Fig. 7.6. This way, the unknown REMPI wavelengths for the H_2 ground electronic $X^1\Sigma_g^+$ v$= 0, 1$, J$= 0, 1$ levels can be obtained. Although not shown in Fig. 7.6, the two copper electrodes are connected on the outside to a variable power supply[3] providing up to -800 V voltage difference between the electrodes, since it is the H_2^+ ions we wish to detect. The ionisation

[1] Cobra-Stretch from Sirah
[2] Surelite II by Continuum operating at 10 Hz repetition rate
[3] Custom made photomultiplier tube power supply

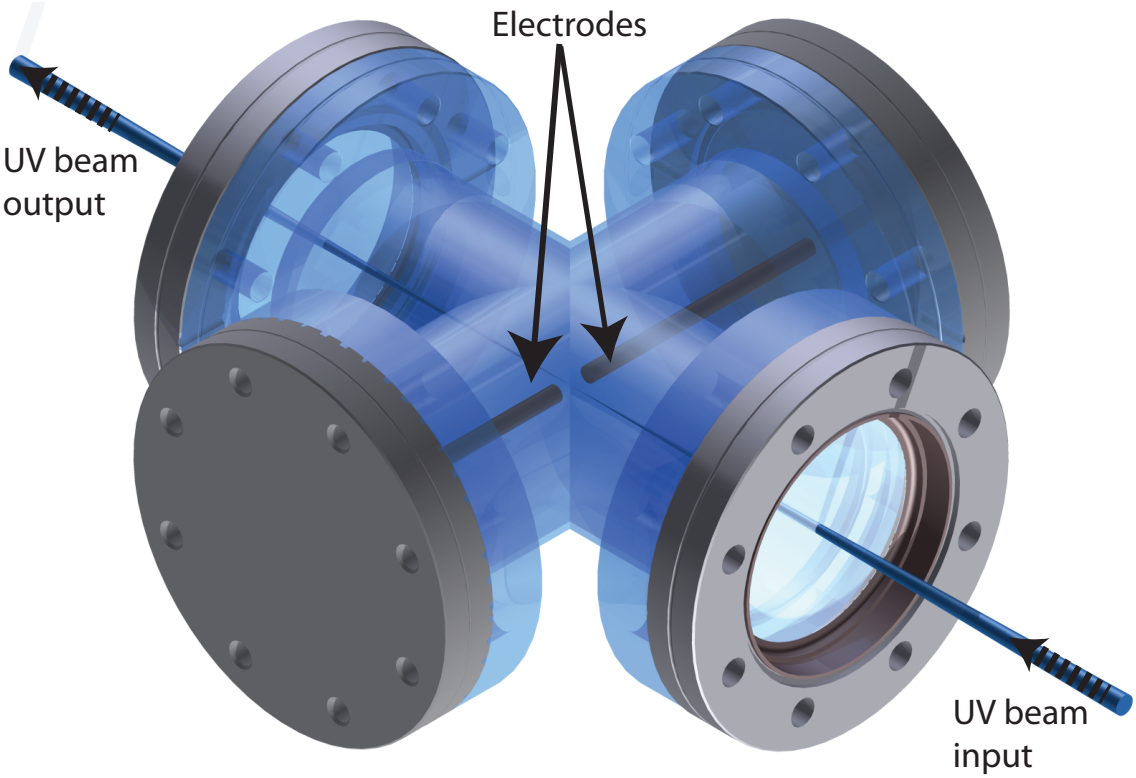

Figure 7.6: Render of the test cell used for the initial REMPI measurements. Shown are the two copper electrodes, separated by a distance of $3-5$ mm which would measure the ions created via the REMPI process H_2^+, as well as the input and output UV beam entering and exiting the beam through two fused silica optical feedthroughs. Not shown for simplicity are the outputs of the electrodes, as well as the inlet and outlet gas flanges.

signal is measured in parallel to that circuit loop through the oscilloscope, with the addition of a high voltage capacitor in series in order to cut out the DC signal. Also not shown, is the 10 cm focussing lens used to focus the UV beam in the centre, right in between the two copper electrodes.

For H_2, the intention is initially for the ground electronic $X^1\Sigma_g^+$ v$=0,1$, J$=0,1$ states to be measured through the resonant $E,F^1\Sigma_g^+$ state. We perform measurements by using a gas mixture of 10% H_2 in Neon. It is important that we use the maximum possible laser intensity and gas pressure, since the signal is expected to be much weaker due to the smaller absorption cross-section of the $(2+1)$ REMPI process in H_2. Spectral locations for the H_2 REMPI signals, can be found in the literature for previous studies performed in this regime, either experimental [195, 200] or theoretical [201].

Figure 7.7 is an experimentally obtained REMPI spectrum for the $X^1\Sigma_g^+$ v$=0$, J$=0,1$ H_2 levels obtained from our test cell. The measurement was performed by measuring the signal on the electrodes in the cell, with respect to the UV wavelength. The measurements

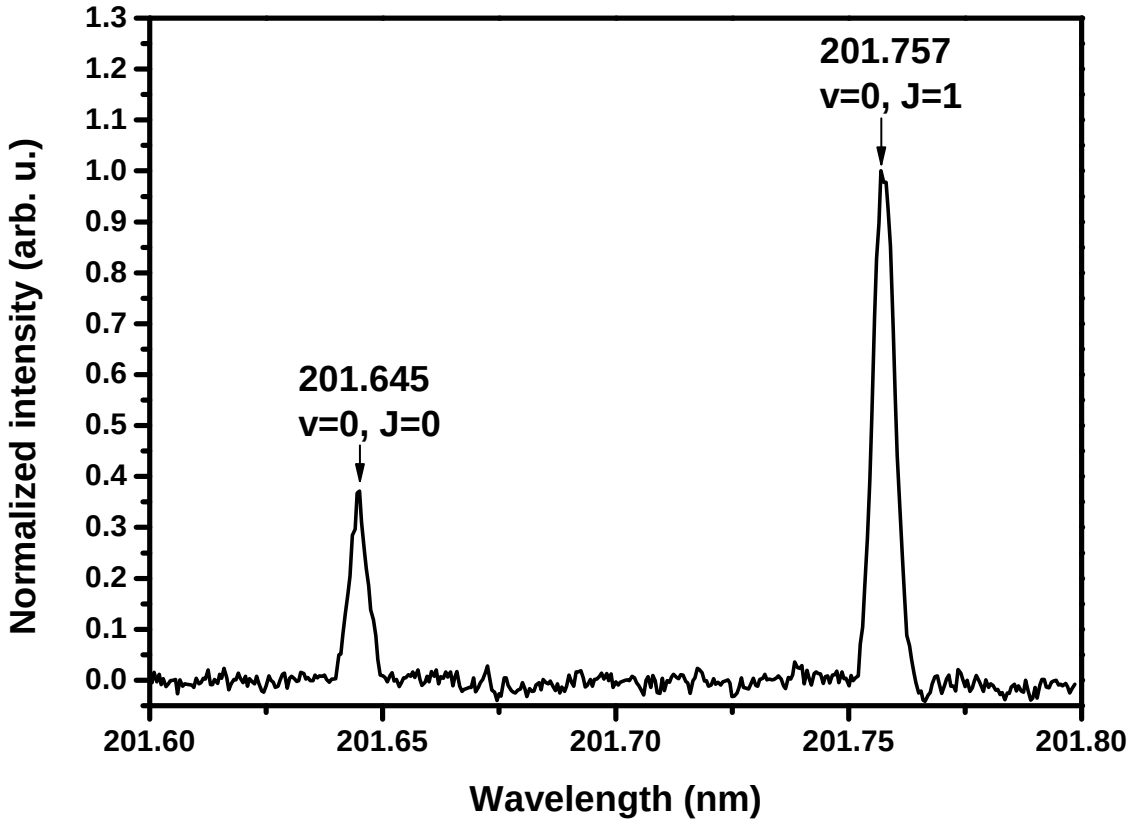

Figure 7.7: Obtained experimental H_2 REMPI spectrum from our test cell for the ground electronic, v= 0, J= 0 and v= 0, J= 1 molecular states.

were recorded via a simple LabVIEW program. The pressure in the cell was at ~ 10 Torr, while the voltage across the electrodes was set to just below discharge at approximately 200 V, with an electrode separation of 0.5 cm. The ground electronic, v= 0, J= 0 and v= 0, J= 1 spectral lines can be clearly identified, with a good signal-to-noise ratio (SNR).

Through the Boltzmann distribution, for an operating temperature of 293 K it is expected for the $X^1\Sigma_g^+$ v= 0, J= 0 state of H_2 to be populated by $\approx 16.6\%$ of the H_2 molecules while the $X^1\Sigma_g^+$ v= 0, J= 1 state by $\approx 27.8\%$. Hence the relative heights of the peaks shown in Fig. 7.7 should have a relative intensity ratio of $\approx 1:2$, which is clearly not the case as this relative intensity ratio is $\approx 1:3$. This happens simply because H_2 can appear in the form of *ortho*-H_2, where the spins of the hydrogen nuclei are parallel, and the form of *para*-H_2 where the nuclear spins are anti-parallel [202, 203]. This induces a degeneracy of 1 for even J states and of 3 for odd J states [204]. Taking this degeneracy into consideration, explains the $\approx 1:3$ ratio which we observe in our measurement. The fact that this ratio is not *exactly* $1:3$ is simply due to the magnetic interaction of the H_2 nuclear spins with paramagnetic centres, such as the copper electrodes we are using in our setup [203]. This can lead to conversion of *para*-H_2 into *ortho*-H_2 and hence change the

relative ratio of the two populations.

7.3.2 Finding the $X^1\Sigma_g^+$ v= 1, J= 0, 1 H_2 REMPI wavelength

The difficulty in finding the REMPI wavelengths for high ro-vibrational state populations in H_2 lies in the fact that they are not highly populated in thermal equilibrium. The Boltzmann equation for the various (v,J) ro-vibrational level populations is given by [195]

$$N(\mathrm{v},\mathrm{J}) = g_\mathrm{n}(2\mathrm{J}+1)e^{-E_\mathrm{rot}(\mathrm{v},\mathrm{J})/kT} \times e^{[-E_\mathrm{vib}(\mathrm{v})+E_\mathrm{vib}(0)/\sum_{\mathrm{v},\mathrm{J}} N(\mathrm{v},\mathrm{J})]}, \tag{7.1}$$

where g_n is the nuclear spin degeneracy factor, with

$$E_\mathrm{rot}(\mathrm{v},\mathrm{J}) = [B_\mathrm{e} - \alpha(\mathrm{v}+\frac{1}{2})]\mathrm{J}(\mathrm{J}+1) - D_\mathrm{J}\mathrm{J}^2(\mathrm{J}+1)^2, \tag{7.2a}$$

$$E_\mathrm{vib}(\mathrm{v}) = \omega(\mathrm{v}+\frac{1}{2}) - \omega_x(\mathrm{v}+\frac{1}{2})^2, \tag{7.2b}$$

where B_e is the rotational constant, α is the rotational-vibrational coupling constant, D is the centrifugal distortion constant, ω is the vibrational frequency and ω_x is the second order anharmonicity term. Solving Eq. 7.1 for a range of temperatures reveals that no more than $\sim 2\%$ of the total H_2 population would populate the v= 1, J= 1 level which is of interest to us, and that would only occur at $\sim$ 5000 K, if H_2 even exists in these temperatures. Figure 7.8 is a plot of the v= 0, J= 0, 1 and v= 1, J= 0, 1 populations for a temperature range of $0 - 10000$ K. It is of course then implied that, even if we were able to heat up the molecular gas at such a high temperature, detecting those scarcely thermally populated ro-vibrational levels would have been a very difficult task with the simple electrodes used in the test cell. Thus, an experimental scheme has to be found in which the higher ro-vibrational levels would be sufficiently populated and detected through our simple detection setup.

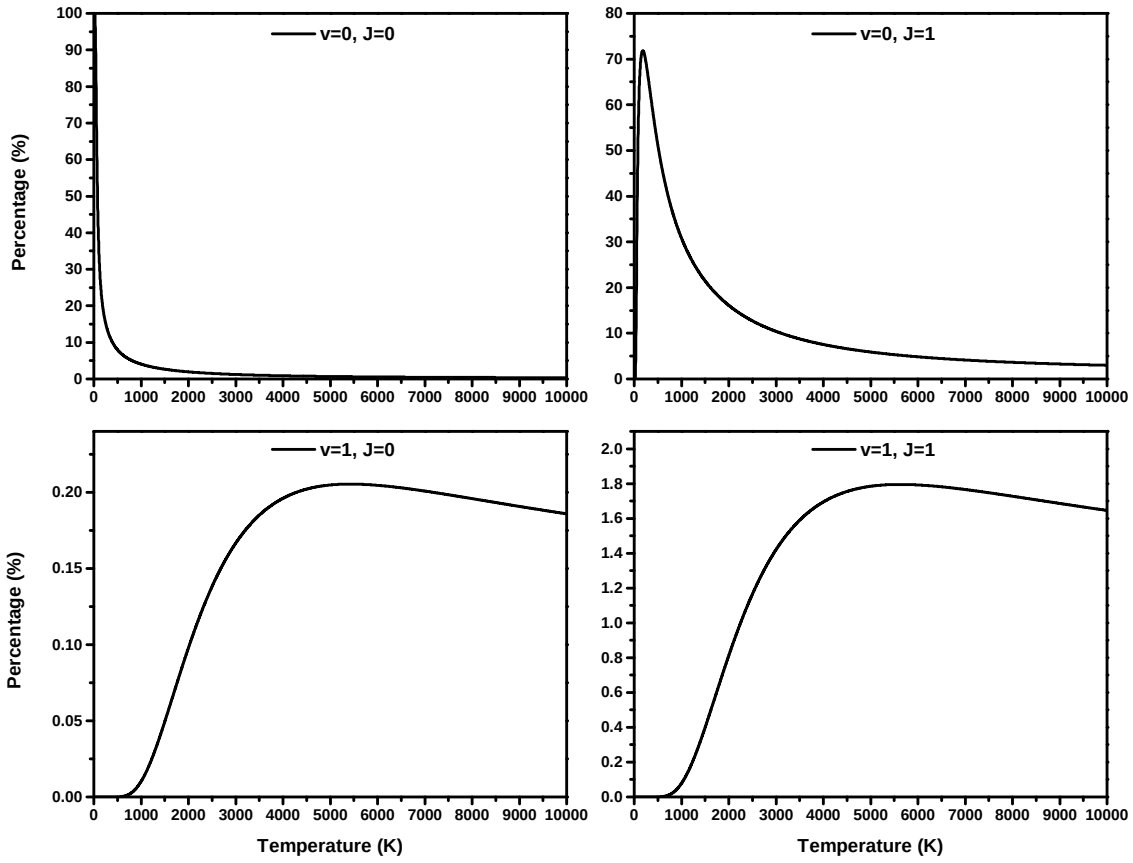

Figure 7.8: Simulations of the v= 0, 1, J= 0, 1 H_2 state populations for a temperature range of T= 0 − 10000 K. Not more than 2% of the total H_2 population can be found in the v= 1, J= 1 state that is of interest to us.

Populating ro-vibrational levels via non-equilibrium discharges

The solution to efficiently populate the H_2 $X^1\Sigma_g^+$ v= 1, J= 1 level so that it can be detected via REMPI, comes through implementing a non-equilibrium DC glow discharge in the test cell. A gas discharge is an ionised gas constituted of equal concentrations of positive and negative charges and a large number of neutral species. In its simplest implementation it is formed by a relatively high voltage difference (ranging from a few hundred volts to a few kV) across two electrodes in a cell filled with gas. Due to the potential difference, electrons that are emitted from the cathode due to the cosmic radiation are accelerated away from it, giving rise to collisions with the gas atoms or molecules. The occurring excitation collisions give rise to excited species which can decay to lower levels by the emission of a photon - hence the name *glow* discharge. Apart from the excitation collisions, ionisation collisions also take place which create ion-electron pairs. The resulting ions are then accelerated towards the cathode where they release secondary electrons; these electrons

are then accelerated towards the anode giving rise to more excitation/ionisation collisions and this way reinitiating the process. Because of this action of the secondary electrons, the glow discharge is characterised as a *self-sustained plasma*.

In order to experimentally obtain a DC glow discharge, a modification needed to be made to the test cell in order for it accommodate a longer electrode spacing, which would allow for a bigger positive column to be formed [205]. The positive column is the space in the discharge where most of the collisions take place. Thus, the UV REMPI beam should be propagating through it as it is where most of the H_2 molecules in the $X^1\Sigma_g^+$ v= 1, J= 1 state would be found.

The electrodes were also modified to have a larger area, so that an even bigger discharge volume could be created across them. We operated the discharge at a pressure of $\sim$ 15 Torr, with a potential difference of $\sim$ 1.2 kV across the electrodes, the separation of which was now 5 cm. The voltage had to be adjusted such that the discharge overcame the positive

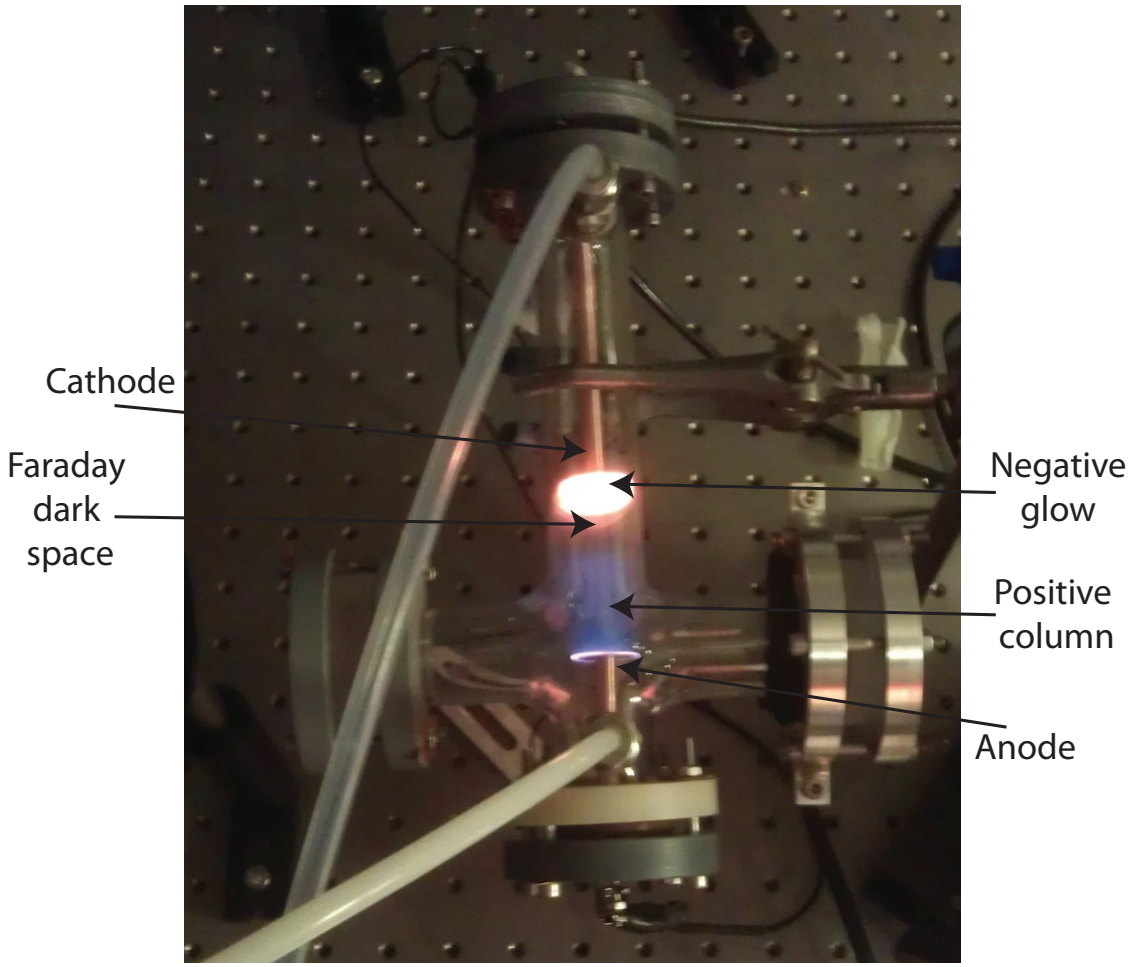

Figure 7.9: A DC glow discharge as was observed in our lab. Noted are the anode and the cathode, as well as the characteristic regions of the discharge (the negative glow, the Faraday dark space and the positive column).

column corona oscillations and reached the steady self-sustained regime [206, 207]. Figure 7.9 is an actual photograph of the modified glass cell, when a self-sustained plasma has been achieved.

With the DC glow discharge established, REMPI measurements were ready to be obtained for the higher ro-vibrational states of H_2. Expected wavelength values for these lines were again obtained from the literature, while the scans were made through the same LabVIEW program used in the $X^1\Sigma_g^+$ v= 0, J= 0, 1 REMPI scan. Figure 7.10 presents the REMPI spectrum obtained for the $X^1\Sigma_g^+$ v= 1, J= 0, 1, 2, 3 states of H_2 in the non-equilibrium DC glow discharge. It is noteworthy that we were able to detect not only the population that we were interested in, but also even higher J populations, thus rendering glow discharges ideal for identification of these states. It is also worth mentioning that even in a highly collisional regime such as the one that exists in the glow discharge, the para-H_2 states (J= 1 and J= 3) are more populated than the respective ortho-H_2 states (J= 0 and J= 2).

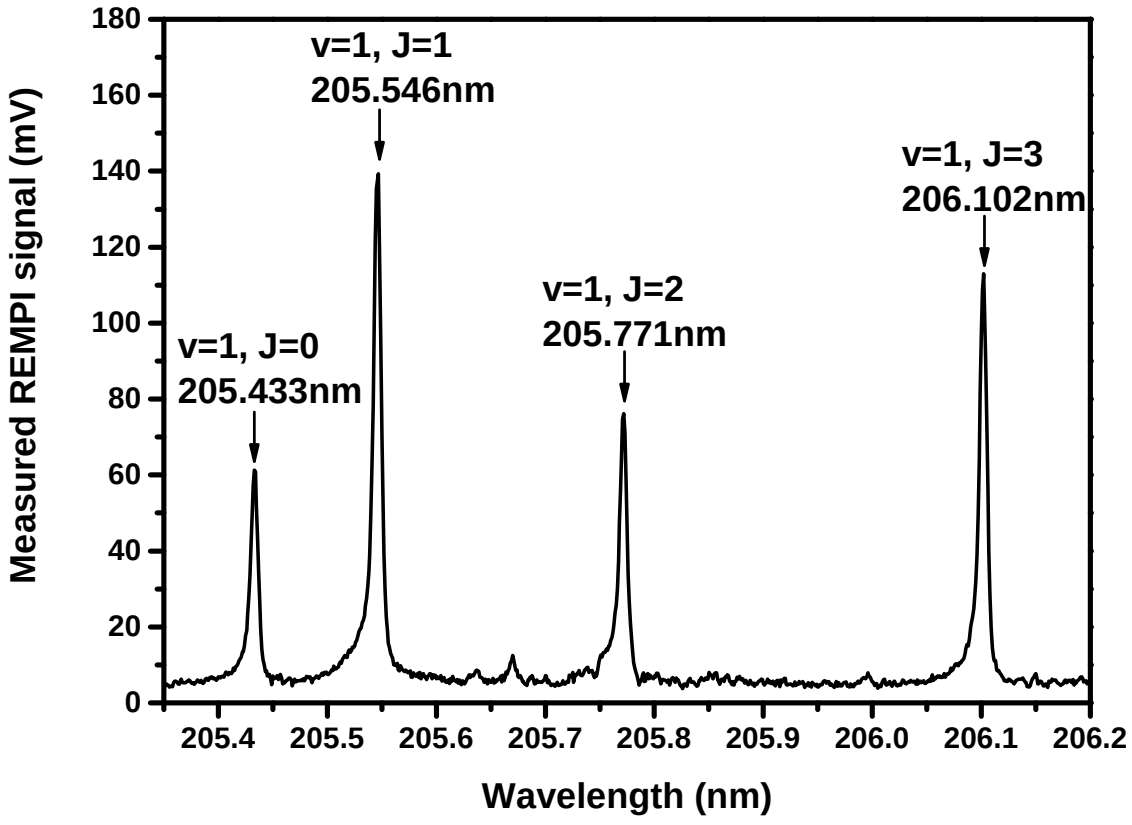

Figure 7.10: Experimentally obtained REMPI wavelengths from the DC glow discharge shown in Fig. 7.9. It is observed that even higher than the v= 1, J= 1 state that is of interest to us ro-vibrational states can be mapped out using this method.

7.3.3 Establishing the SRP wavelength

As mentioned earlier, the SRP wavelength for the desired $X^1\Sigma_g^+$ v = 1, J = 1 $\longleftarrow$ $X^1\Sigma_g^+$ v = 0, J = 1 transition can be established via CARS. A new dye laser[4] was installed in the lab to provide with the pump wavelength of the SRP process. This dye laser, when pumped by $\approx$ 400 mJ by a 532 nm pump[5], provides with pulses of energies up to 5 mJ/pulse in the $730-740$ nm region. We have to note that due to the laser being largely miscalibrated, all spectra hereafter referring to this laser will be based on the reported by the laser wavelength which does not necessarily coincide with the true value of the wavelength.

As was the case with finding the REMPI wavelengths for the $X^1\Sigma_g^+$ v = 0 , J = $0, 1$ states, the CARS pump wavelength which would subsequently be the SRP pump wavelength in our detection scheme, was to be found in the test cell initially (Fig. 7.6). One of the two IR beams was focussed through a 15 cm lens in the centre of the cell while the probe beam, co-propagating to the IR beam, was sent along the same path. The focii of the two beams were aligned through a CCD camera. The CARS process is proportional to the density of molecules providing the signal [119], hence the test cell was filled with the same 90% Ne - 10% H_2 gas mixture to be used in the deceleration experiment, at a pressure of an atmosphere. Even higher pressures would have been desirable, but we would be running the risk of gas leaking out of the cell.

The CARS signal consists of photons with a 564.68 nm wavelength, so there was no need for a voltage difference to be applied to the electrodes in the cell. Right after the output face of the cell two dichroic mirrors were placed, one to discard the 1064 nm radiation and a consecutive one to discard the $\sim$ 735 nm radiation. Some of the pump beam was leaking through the second dichroic, which we used in order to align a fast photodiode[6] to it, as the CARS beam would be co-propagating the pump and probe beams on the output of the cell. An uncoated lens of 5 cm focal length was used to focus the beam on the photodiode. Once optimum alignment of the photodiode was performed, the leaking pump beam was filtered out with the use of an additional 565 ± 5 nm laser line filter. The pump and probe beams were temporally aligned with the use of a photodiode at the interaction region.

Measurements were obtained by modifying the same LabVIEW program that was used for the determination of the REMPI wavelengths to be controlling the wavelength of the

[4]ND6000 by Continuum
[5]Quanta-Ray by Spectra-Physics, operating at 10 Hz
[6]DET36A/M by Thorlabs

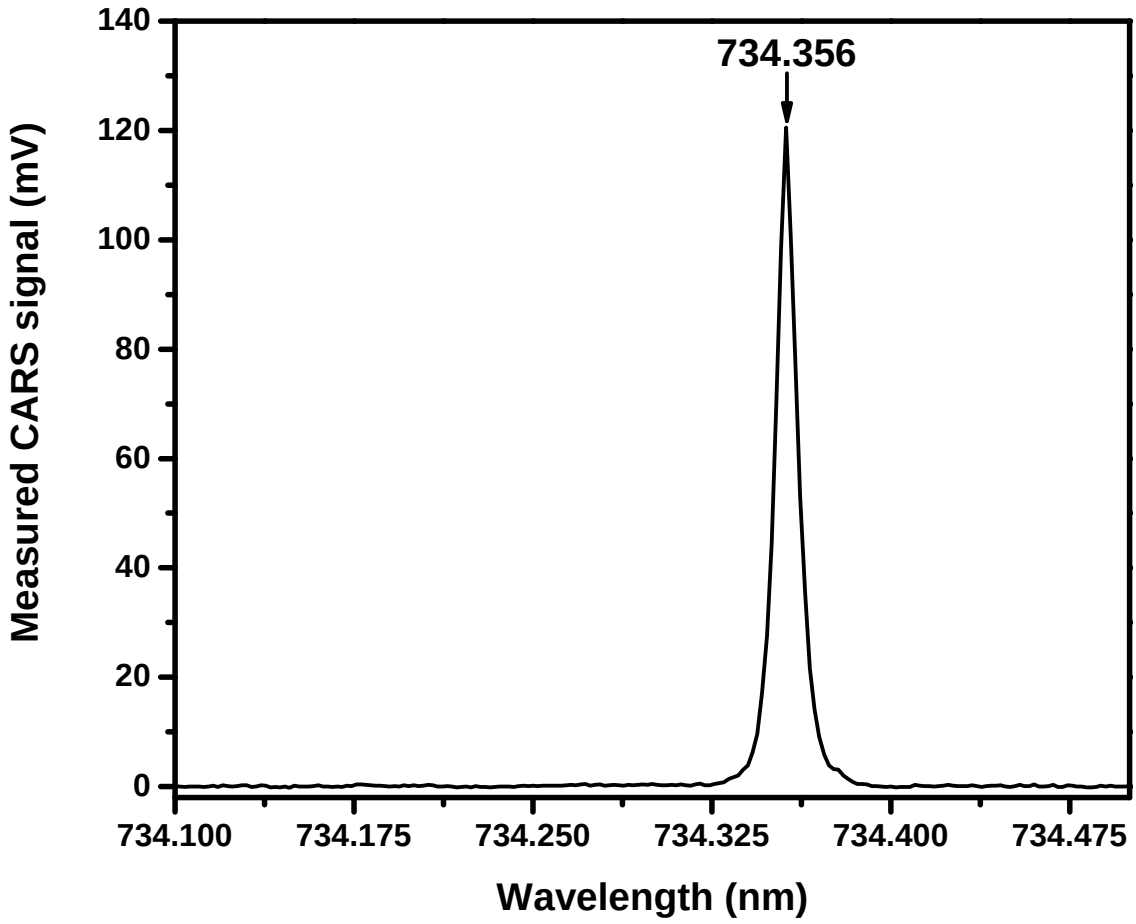

Figure 7.11: Measurement of the CARS wavelength, obtained from our glass cell.

pump laser this time rather than the REMPI wavelength. By manually scanning the wavelength of the pump, we were able to coarsely find the wavelength where the CARS signal was to be obtained. In that wavelength, the signal beam was a very bright yellow-green beam, easily observable by the naked eye. This allowed us to fine tune the alignment in order to optimise the process. Verification of the fact that indeed a CARS process was occurring, was made by blocking either one of the pump and probe beams and observe the signal disappearing. Because the signal was so bright that it saturated the photodiode, an additional ND= 1 filter was placed in front of the photodiode. It is also important to note that the probe's polarisation was varied with the use of a $\lambda/2$ waveplate, in order to match the polarisation of the pump beam, since CARS is a polarisation dependent process. Figure 7.11 is a plot of the obtained CARS measurement. It can be observed that the CARS peak is sharp, having a width of ~ 0.01 nm, while we are estimating a $\sim 0.03\%$ efficiency of the process (Appendix B).

7.3.4 Obtaining an SRP plus REMPI signal

After both the SRP and the $X^1\Sigma_g^+$ v= 1, J= 1 H_2 REMPI wavelengths had been independently defined, the last step in configuring our detection scheme to be used in tagging the H_2 molecules interacting with the decelerating lattice, was to actually obtain an SRP plus REMPI signal from the test cell. This would demonstrate the ability to successfully transfer molecular population from the $X^1\Sigma_g^+$ v= 0, J= 1 level to the $X^1\Sigma_g^+$ v= 1, J= 1 from where molecules would be detected via REMPI.

In order to experimentally demonstrate this in the test cell, the UV REMPI beam was set to counter-propagate the pump and probe beams driving the SRP transition. Alignment was performed with all three beams going through the same holes (set by masks) on the two focussing lenses, as well as through the same pinhole in the centre of the glass cell. Temporal alignment of the beams was performed by a photodiode close to the interaction region. The electrodes were changed to the ones used in the $X^1\Sigma_g^+$ v = 0 , J = 0, 1 measurement, having a separation of 3 mm and a voltage difference of $\sim$ 1 kV. The pressure in the gas cell was an atmosphere. The UV wavelength was set to the one obtained from Fig. 7.10 for the $X^1\Sigma_g^+$ v = 1 , J = 1, while the wavelength of the pump laser would be scanned in order to verify the SRP signal. Through coarse scanning of the wavelength of the pump laser, the SRP plus REMPI signal was obtained at the wavelength found for CARS (Fig. 7.11). Indeed, sparking could be observed across the electrodes at the correct pump wavelength, while the process was verified by observing the signal disappearing when either one of the three beams resulting the SRP plus REMPI signal was blocked. Figure 7.12 is a plot of the obtained SRP plus REMPI spectrum from the test cell. It can be observed that the width of the SRP plus REMPI line is wider than the one obtained for CARS alone (Fig. 7.11), but that can be attributed to the fact that the measurement is saturated. Before starting to look for deceleration, our detection scheme had to be verified in the vacuum chamber containing the source of H_2 molecules to be decelerated.

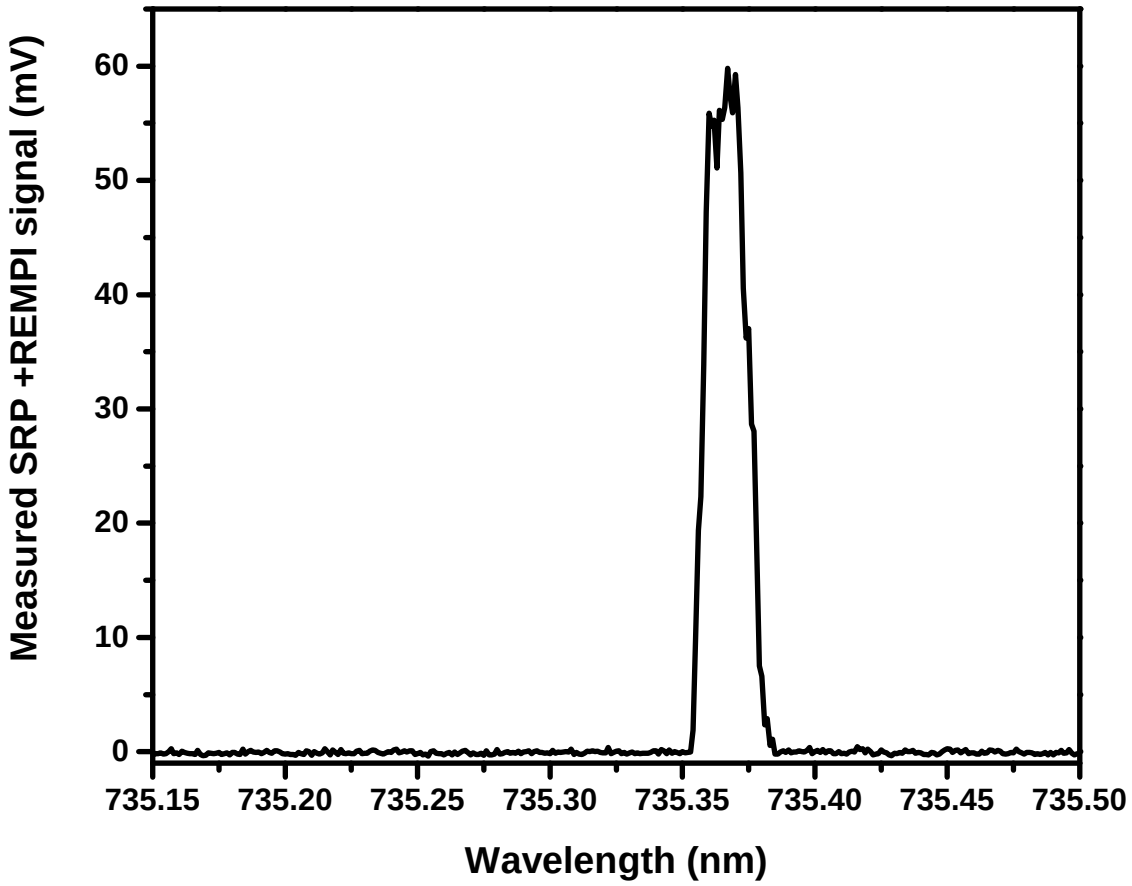

Figure 7.12: Experimentally obtained SRP signal from the test cell. The wavelength of the pump laser was varied and the ions created and detected by the electrodes were recorded.

7.4 Establishing the H_2 detection scheme in the vacuum chamber

7.4.1 The source

The source used in the experimental setup for chirped OSD was provided by our collaborators from Dr. Michael Tarbutt's group at Imperial College London. The source consists of a pulsed solenoid valve[7] which uses a mixture of 10% H_2 in an inert carrier gas. Its output is connected to a curved nozzle, delivering gas to the interaction region (Fig. 7.13). The valve is mounted on a plate that can be cooled using liquid nitrogen, or mounted on the 4 K cold plate of a closed-cycle cryocooler. The backing pressure of the valve is set at around 1000 mbar while the pressure within the vacuum chamber with the use of a turbopump[8] reaches 5×10^{-8} mbar. The custom made electronics that drive the valve allow it to produce molecular beam pulses of variable durations ranging from $200 - 1000$ μs, depending

[7]Series 99 from Parker-Hannifin
[8]TMP-1003LM by Shimadzu

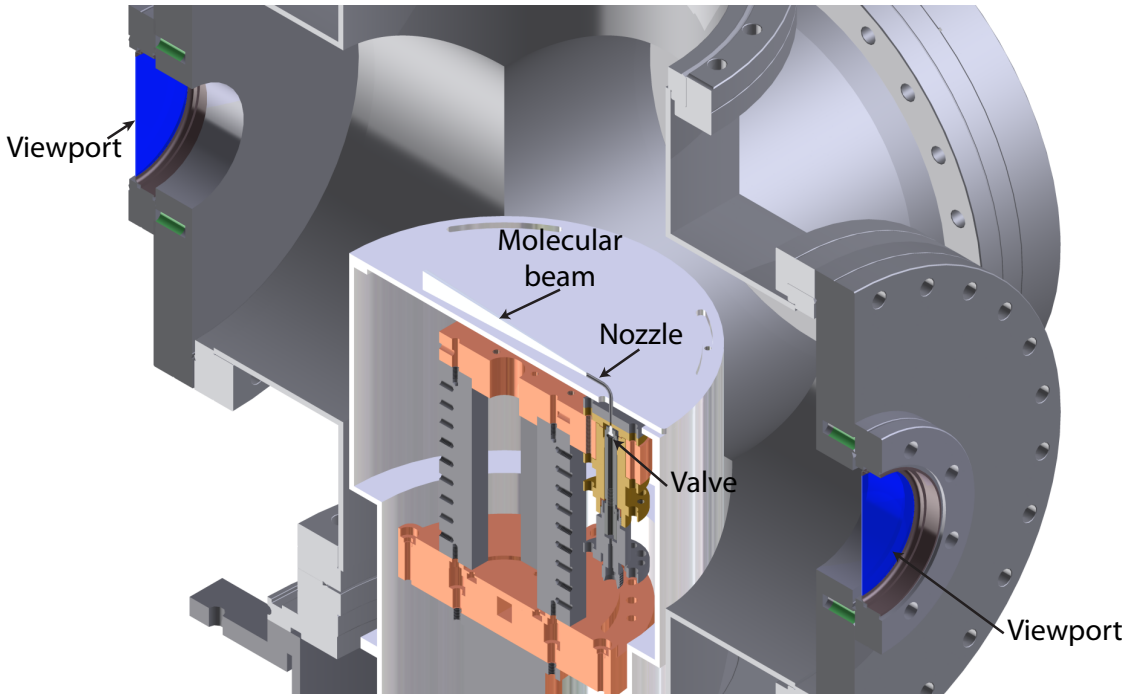

Figure 7.13: Render of the H_2 source used in the chirped OSD experiment. Shown are the valve and the nozzle which delivers the Ne-H_2 gas. The source is housed in a standard 6-way DN200CF cross (C6 − 1000 from Kurt J. Lesker). Reducer DN200CF flanges provide for optical viewports for the laser beams and electrical feedthroughs for all the necessary connections inside the chamber. The turbopump (not shown here) sits on the top flange.

on the duration of TTL signals received from the delay box. Pulsed valve operation is preferred to a constant flow, since much higher molecular densities can be obtained. Hydrogen molecules in the beam are expected to have a translational temperature of less than 1 K, and to be mostly in the ro-vibrational ground state.

The mean velocity of the molecular beam is determined by its temperature through the equation

$$\frac{\gamma}{\gamma - 1} k_B T = \frac{1}{2} M v^2, \tag{7.3}$$

where $\gamma = 5/3$ is the heat capacity ratio, k_B is Boltzmann's constant, T is the gas temperature, M its mass and v its velocity. Since the gas mixture used consists mainly of neon, it is safe to make the assumption that the gas mass is equal to that of neon. At room temperature, the use of a neon carrier gas gives a mean beam velocity of 830 ms^{-1}. In order to reach lower velocities for the molecular beam, so that deceleration would be more efficient there are two approaches. The first is to use a carrier gas of higher mass, such as argon ($M = 40$ amu), giving a speed of 590 ms^{-1} or krypton ($M = 84$ amu), giving 410 ms^{-1}. Inert gases are preferred due to the fact that they do not react with H_2. Experimentally it has been found that beam fluxes using very heavy carrier gases can be lower, perhaps due

to clustering effects. The second approach is to lower the temperature of the gas mixture to just above the vapour temperature of the carrier gas (27 K for Ne, 87 K for Ar, 120 K for Kr). At liquid nitrogen temperatures a neon beam has a speed of 420 ms^{-1} and an argon beam has a speed of 300 ms^{-1}. Using a cryocooler to reach temperatures of about 4 K it is possible to obtain beam velocities as low as 210 ms^{-1}. Initially the source will be operated using a neon or argon carrier gas at room temperature. Once deceleration is experimentally observed in this beam, we can attempt to use a heavier carrier gas or to cool the valve with liquid nitrogen.

7.4.2 Detecting $X^1\Sigma_g^+$ v= 0, J= 1 H_2 REMPI in the vacuum chamber

Since the REMPI wavelengths had been established, the next step was to replicate them in the molecular chamber with the pulsed H_2 molecular beam. The UV beam was focused through a 50 cm lens and delivered through a fused silica window to the interaction region. Initially the UV wavelength was set at the wavelength corresponding to the $X^1\Sigma_g^+$ v= 0, J= 1 state, and the timing of the pulsed valve was varied until enough signal was observed through the MCP. Then the same LabVIEW program was used to scan the wavelength of the UV laser. Figure 7.14 is a render of this setup while Fig. 7.15 is a plot of the results from this scan in comparison to the ones obtained from the test cell.

The two spectra presented in Fig. 7.15 show perfect agreement, while in the case of the detection through the MCP the signal-to-noise ratio (SNR) has improved by much.

Before starting to look for the SRP plus REMPI signal in the vacuum chamber, it is important to obtain the temporal profile of the pulsed molecular beam, both in order to temporally align the molecular beam to the laser beams, but also in order to obtain the velocity distribution of the beam. Figure 7.16 presents the molecular beam profiles obtained for two values of valve opening times, 300 μs and 400 μs, at a distance of 3 cm from the valve. These measurements were obtained by measuring the signal on the MCP while varying the UV beam's relative delay with respect to the opening of the valve and were performed with the UV beam's wavelength set to ionise the $X^1\Sigma_g^+$ v= 0, J= 1 state. For the temporal alignment of the molecular beam we only need to operate at the time when the maximum number of molecules is delivered to the interaction region (i.e. the peak of the curve). For the velocity distribution to be derived, a second measurement needs to be performed further away from the valve.

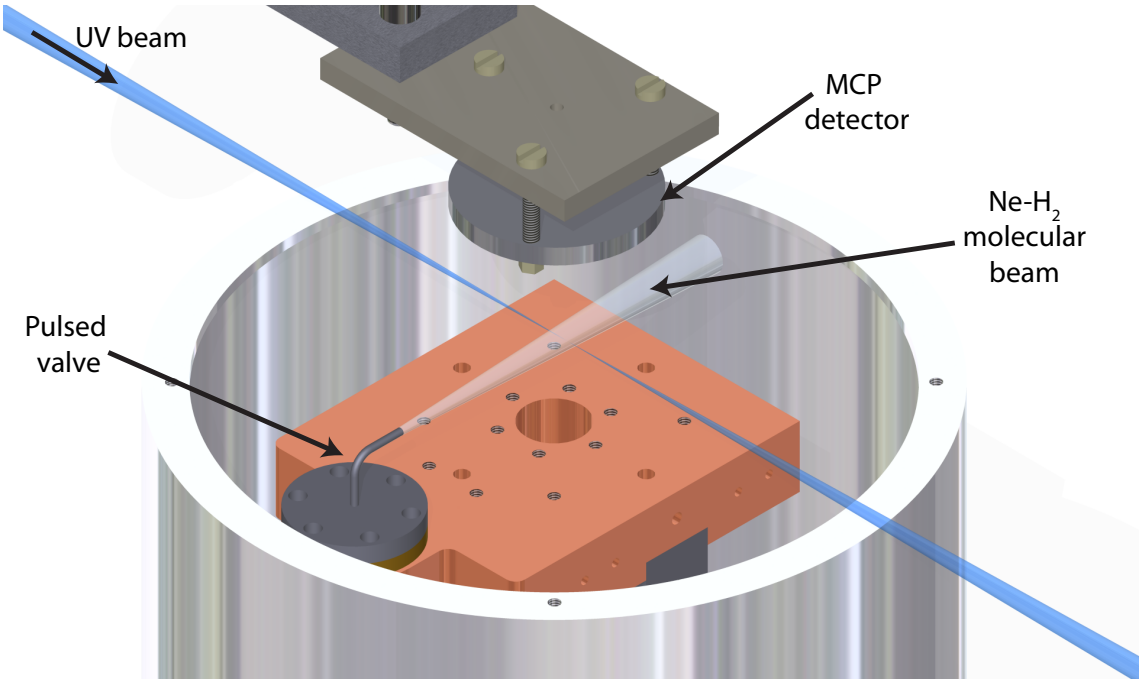

Figure 7.14: Render of the setup used for the detection of the $X^1\Sigma_g^+$ v= 0, J= 0, 1 states of H_2 in the molecular chamber. Shown are the pulsed valve, the microchannel plate (MCP) detector attached to its custom made base, the UV REMPI beam as well as the Ne-H_2 molecular beam.

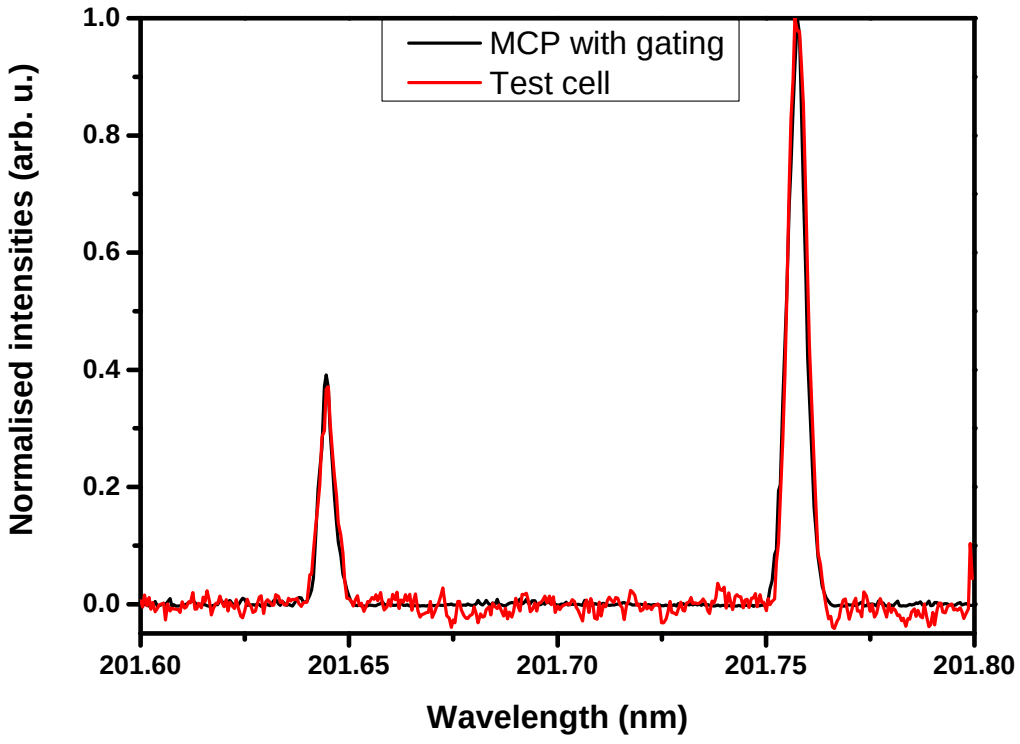

Figure 7.15: Comparison between the experimental REMPI spectra obtained from the test cell (in red) and the molecular chamber (in black)

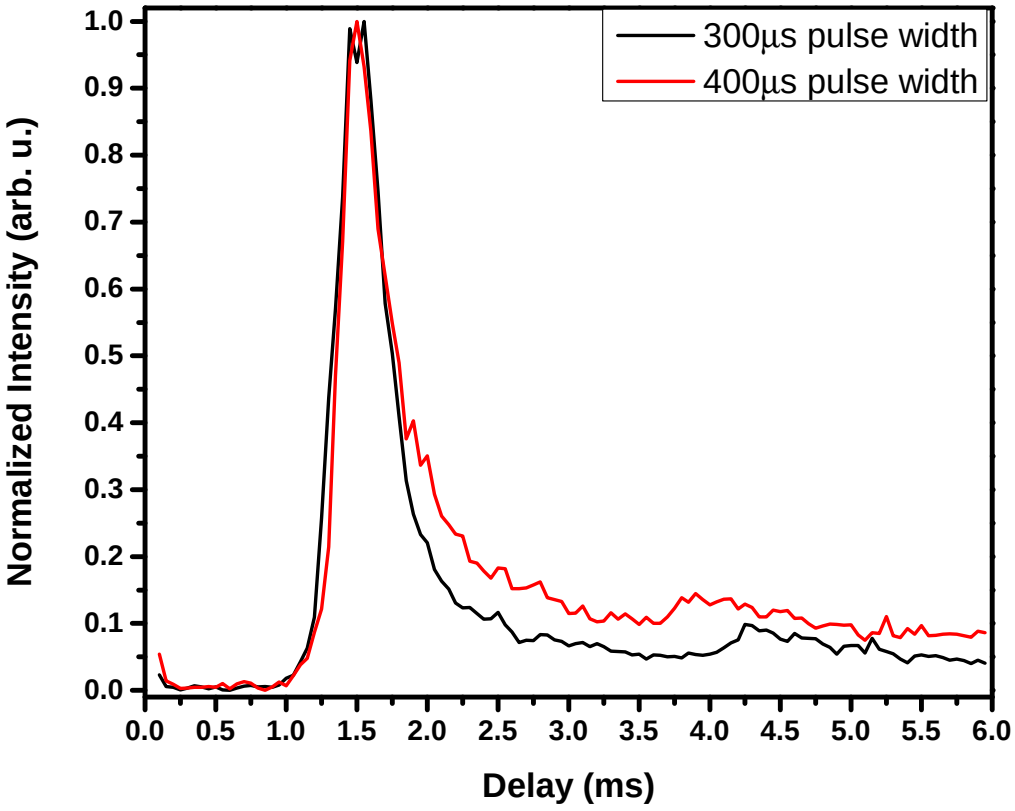

Figure 7.16: Molecular beam profiles for two different pulse width durations of the valve.

7.4.3 Obtaining the SRP plus $X^1\Sigma_g^+$ v= 1, J= 1 H_2 REMPI in the vacuum chamber

The last step in the experimental demonstration of our detection scheme, is to obtain the SRP plus $X^1\Sigma_g^+$ v= 1, J= 1 H_2 REMPI signal in the vacuum chamber. Initially the two IR beams forming the decelerating lattice were aligned by means of single shot CRBS, while the Raman beam was set to co-propagate with IR beam 2 (Fig. 7.17) with the use of a CCD camera. With the use of the same camera, the UV REMPI beam was aligned to be coincident on the focal spot crossing of IR beam 1 (Fig. 7.17) and the probe beam used in single shot CRBS. This way, we know that the UV beam is also aligned to the focal point of IR beam 2 since in order for single shot CRBS to be obtained, IR beam 2 needs to be coincident on the same spot.

Once the chamber was sealed, measurements were performed by scanning the wavelength of the Raman beam, while the UV was set at the $X^1\Sigma_g^+$ v= 1, J= 1 H_2 REMPI wavelength. Figure 7.18 shows a comparison between the SRP plus $X^1\Sigma_g^+$ v= 1, J= 1 H_2 REMPI signal obtained from this measurement, and the one obtained from our glass cell. It can be observed that the two peaks are centred at the exact same wavelength, while

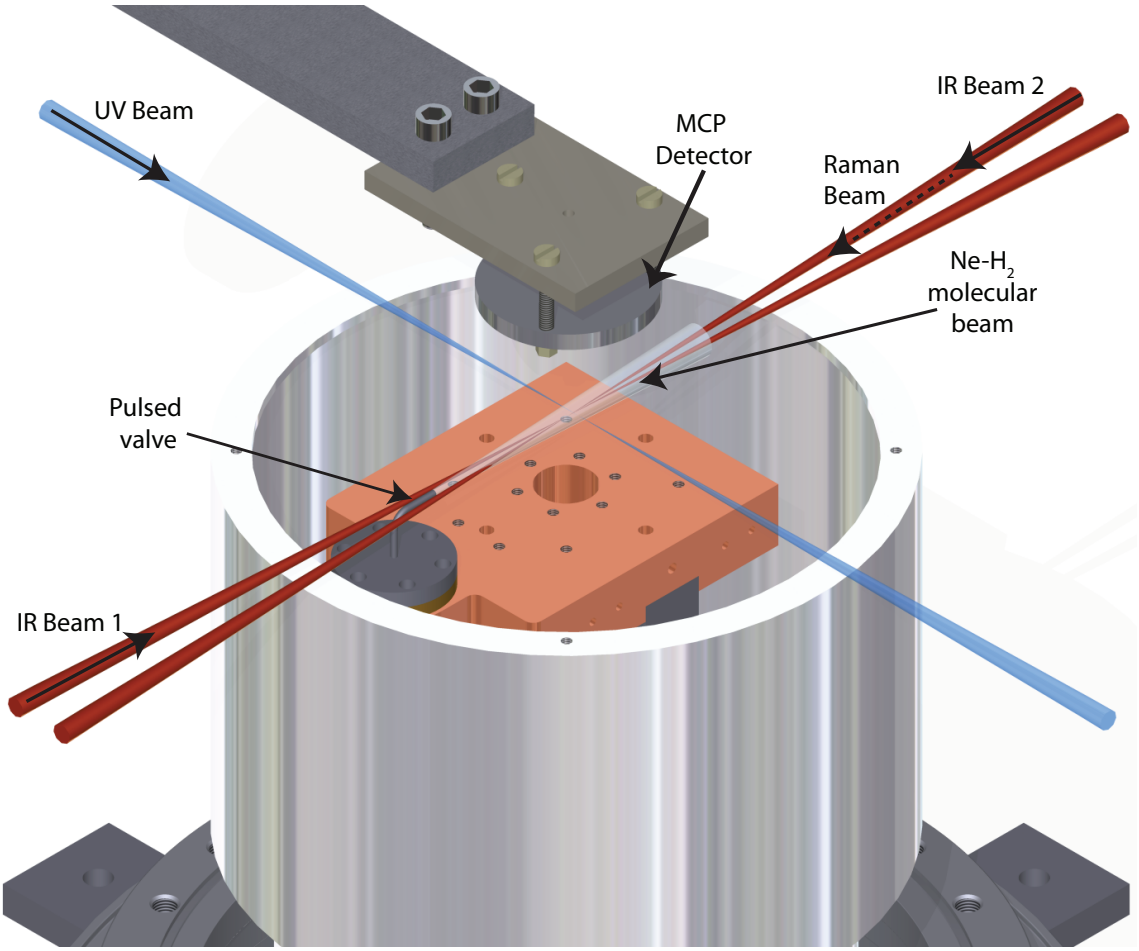

Figure 7.17: Render of the setup used to detect the SRP plus $X^1\Sigma_g^+$ v= 1, J= 1 H_2 REMPI signal in the vacuum chamber. Shown are the two IR beams which were aligned by single shot CRBS, the Raman beam involved in the SRP process and the UV beam. Also shown are the pulsed solenoid valve providing with the molecular beam and the MCP detector used to detect the H_2 molecules ionised via REMPI.

the width of the peak from the vacuum chamber is comparable to the one obtained in the CARS measurement in the glass cell (Fig. 7.11). The SNR of the measurement is not as high as in the $X^1\Sigma_g^+$ v= 0, J= 1 H_2 REMPI measurement (Fig. 7.15) but this is expected as now only a small fraction of the delivered molecules from the nozzle are in the $X^1\Sigma_g^+$ v= 0, J= 1 state from which they are ionised via REMPI. Verification of the SRP plus $X^1\Sigma_g^+$ v= 1, J= 1 H_2 REMPI process was performed by blocking each of the laser beams involved in the measurement and observing the signal disappearing. It is also noteworthy that an SRP plus $X^1\Sigma_g^+$ v= 1, J= 1 H_2 REMPI signal was obtained when either of the two pump beams were on, hence validating our alignment procedure.

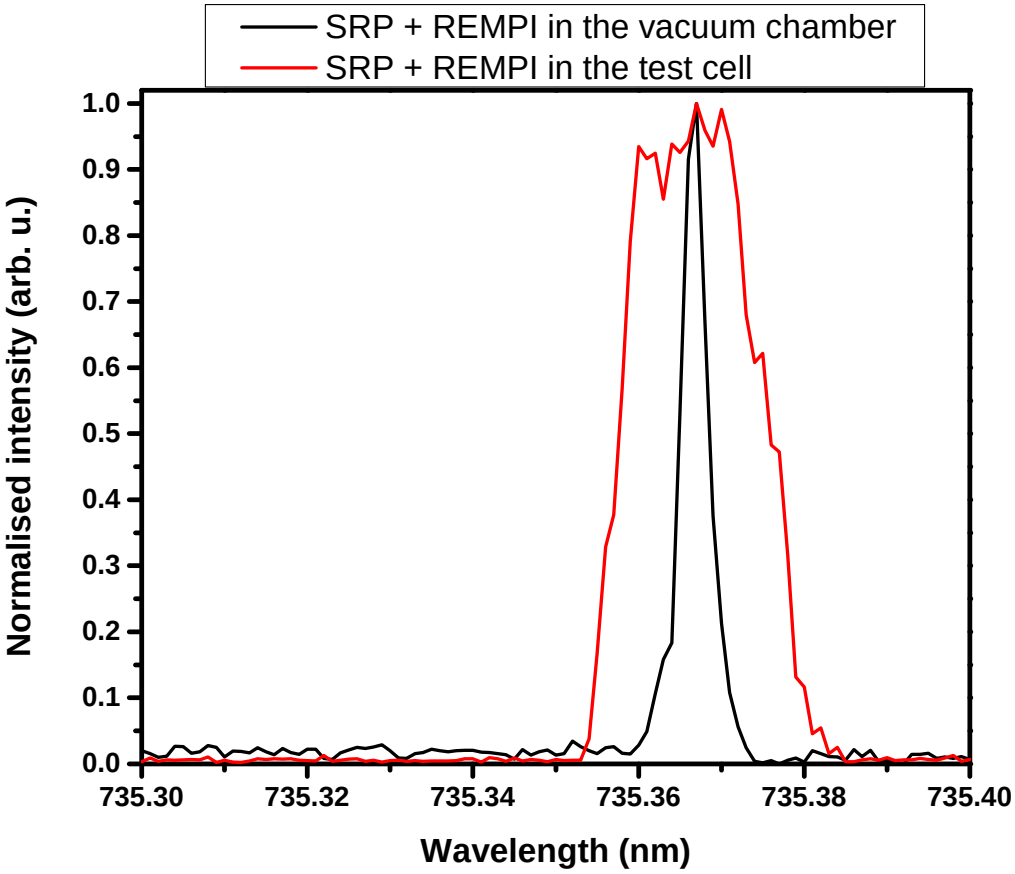

Figure 7.18: Comparison between the obtained SRP plus $X^1\Sigma_g^+$ v= 1, J= 1 H_2 REMPI spectra obtained from the glass cell (in black) and the vacuum chamber (in red).

7.5 Conclusions

In this chapter I presented a setup built for experimental demonstration of chirped OSD as well as a method for transferring H_2 molecules delivered from a molecular beam initially at their ground electronic, ground ro-vibrational state to an upper ro-vibrational state. This molecular population energy level transfer is performed via SRP, while detection of the molecules in this state is performed via REMPI. This method allows for H_2 OSD measurements with the H_2 molecular gas background being eliminated, hence a more detailed and of high SNR experimental demonstration of the OSD scheme can be performed. Additionally, this detection scheme can be used in the optical Stark deceleration of any molecule, provided that the respective SRP and REMPI wavelengths are within the wavelengths offered by the high power lasers that are available.

Chapter 8

Conclusions

This thesis describes the improvements performed to a frequency agile laser system developed by our experimental group and its use in gas diagnostics in the form of coherent Rayleigh-Brillouin scattering. It also describes the development of a method for background free measurements in optical Stark deceleration of H_2 molecules. In this chapter I will summarise the developed laser system and discuss the principal results from the experiments carried out. Finally, I will outline future directions for experiments relating to the work presented in this thesis.

8.1 Summary of the laser system

Our group had already developed a laser system capable of producing laser pulses linearly chirped up to 1.5 GHz over durations between 20 ns to 10 μs, representing chirp rates in excess of 10 GHz/μs. Being based on the output of a single Nd:YVO_4 microchip laser which incorporates an intracavity $LiTaO_3$ EOM, this system through subsequent amplification can produce two pulses of variable frequency difference with energies up to 700 mJ/pulse, corresponding to intensities in the 10^{14} Wm^2 range. These pulses can be used to produce deep periodic optical potentials ($> 1 - 20$K), which can be used for optical Stark deceleration and gas diagnostics.

The microchip laser originally used in this system was presenting some stability issues, mainly due to thermal fluctuations, in its frequency and intensity outputs. In order to overcome this, a new, thermally stable laser was developed. This laser is based on a plane-concave laser cavity configuration rathen than a plane-plane one, thus allowing it to provide with a more stable intensity output. Being a smaller construction compared to the original

one, this laser can achieve the same chirp rates in single mode operation, but at more than three times the output power and higher optical-to-optical slope efficiency (17.02% compared to 2.5%). Although in the end this laser did not replace the one originally intended, it has been used successfully in probing whispering gallery modes in silica spheres, thus showing its versatility.

Finally, by developing a new computer based control of the system's pulse shaper, we were able to increase the laser system's pulse shaping efficiency, as well as its versatility. Now, within minimal amount of time and with a fully customisable interface, optical pulses of the desired temporal profile can be obtained from the laser system.

8.2 Coherent Brillouin scattering

In this thesis we presented for the first time CBS spectra acquired in the gas phase, in the high $y \approx 27$ hydrodynamic regime. These spectra were formed by measuring the intensity of a Bragg scattered probe beam from lattices induced in the gas that the laser pulses produced by our laser system. We measured the evolution of these CBS spectra as a function of pump-probe delay and observed how, apart from the laser driven electrostrictive grating, we are also launching an acoustic grating due to thermalisation of the gas medium.

These two gratings are co-propagating within the gas and are interfering with each other. Constructive interference of these gratings gives rise to additional spectral sidebands, while their destructive interference results in spectral narrowing of the Brillouin peak which can lead to erroneous estimates with quantities relating to its width, such as the gas temperature. Our results indicate that the sidebands and the resulting spectral narrowing can be suppressed or enhanced by the temporal pump pulse profile.

8.3 Single shot coherent Rayleigh-Brillouin scattering

In this thesis we presented for the first time a method capable of obtaining CRBS spectra in a single laser shot of 140 ns duration, based on the chirped lattices produced by our laser system. Using this method, we are able to reduce the acquisition times by ten orders of magnitude. This technique renders CRBS an ideal candidate for diagnostics in combustion and transient flow environments.

We have also presented for the first time, 3D scans of the CRBS spectral profile for CO_2

and xenon. These allow for the evolution of these spectra to be studied with respect to the $y-parameter$, as well as provide with vast amounts of experimental data which could aid in the optimisation of theoretical models describing the CRBS process, such as the Tenti s6 and s7 models, as well as the development of new, more accurate theoretical models, such as the direct simulation Monte-Carlo (DSMC) method [50]. Finally, we note that since CRBS has been proposed for nanoparticle detection [48], the single shot CRBS method presented in this thesis would form an ideal experimental approach to these measurements.

8.4 Optical Stark deceleration

8.4.1 Summary of results

The experimental setup presented in this thesis has already been used successfully in chirped optical Stark acceleration of Ar* atoms [80]. Based on previous, successful implementations of optical Stark deceleration with constant velocity lattices, we tried to implement a method for decelerating H_2 molecules in the $X^1\Sigma_g^+$ v= 1, J= 1 state from a molecular jet, utilising chirped optical lattices.

In order to be able to distinguish the decelerated H_2 molecules from the molecular gas background, we implemented and demonstrated a stimulated Raman pumping method where, by introducing an additional dye laser, we promote to the $X^1\Sigma_g^+$ v= 1, J= 1 state only the H_2 molecules which have interacted with the decelerating lattice and further resonantly ionise and subsequently detect only the ones that have reached this upper state. This method then allows for background free measurements of the decelerating process.

8.4.2 Future experiments

The experiment as it stands now is ready for experimental demonstration of optical Stark deceleration of H_2 molecules. With linearly chirped lattices of up to 1.5 GHz, H_2 molecules in a gas mixture of 90% Ar-10% H_2 can be decelerated, while the whole deceleration process can be monitored to great accuracy without any background noise. This will allow for sufficiently decelerated H_2 molecules to be produced and further be co-trapped in an optical cavity with ultra-cold argon atoms, thus implementing the sympathetic cooling scheme which will allow for observation of H_2 molecules in temperatures less than 100 mK.

Appendix A: Microchannel plate (MCP) driving circuit

For the detection of the REMPI generated H_2^+ ions, an MCP detector[1] was used. MCP detectors consist of a 2-D array of ultra-small diameter ($4-25$ μm) glass capillaries. When electrons or ions, accelerated from an electric field applied across both end surfaces of the MCP, enter these channels, they generate secondary electrons from their interaction with the capillary walls. This process is repeated many times across the capillaries, resulting in an amplified electric signal at the end side of the detector. Thus, the principle of operation of an MCP is similar to that of a photo-multiplier tube, only for electric charges this time.

For positive ion detection, the MCP is driven by a negative voltage difference between its end surface and ground. This is divided internally on the MCP on $\approx 90\%$ being delivered between the front surface of the MCP and the ground, in order to provide for a sufficiently large electric field to attract the ions, while the remaining $\approx 10\%$ is applied between the two MCP surfaces to aid in the drift of the carriers through the capillaries. The gain of the MCP is delivered for voltages between -1.5 kV to -2.4 kV, with that gain increasing quadratically with respect to the applied voltage. The signal is collected is series to the two surfaces of the MCP and measured on an oscilloscope.

Considering a distance d between the MCP and the ground, the electric field between them would be given by $E = \frac{V}{d}$, where V is the applied voltage. A particle in this field would experience a force F equal to $F = qE$, where q is the particle's charge. From Newton's second law it follows that $m\alpha = qE$, where m is the particle's mass and α its acceleration. If we assume the particle to be at an initial distance s from the detector, then the time it will take it to be detected after it has got ionised is given by:

$$t = \sqrt{\frac{2smd}{qV}}. \tag{8.1}$$

For H_2^+, $V = 1800$ kV, $d = 5$ cm and $s = 3$ cm, equation 8.1 results that it would take a H_2^+ ion approximately ≈ 170 ns to be detected by the MCP after it has been ionised by the UV beam.

Although in principle an operating voltage of -1.8 kV should be enough to detect H_2^+ ions, our experience with our setup has showed us that for the wavelengths of ≈ 200 nm we are operating at, stray UV radiation also generates secondary electrons on the MCP, giving

[1] From Photonics USA

us erroneous signal while also depleting the effective gain of the detector. Considering that ≈ 200 ns are not enough for the gain to build up after the UV radiation has passed through the interaction region so that the H_2^+ ions are effectively detected, this can cause a serious drawback in the detection efficiency. In order to overcome this, based on a circuit proposed in [208], I developed an MCP gating circuit, shown in Fig. 8.1.

This circuit has got two power inputs, one typically at -1.6 kV and one at $+200$ V, as well as a TTL input which provides the gating signal. When the TTL is low, V_{in} goes to -1.6 kV and the transistor's drain (D) charges to $+200$ V. When the TTL goes to high, D is shorted to ground and V_{in} goes to $-1.6 - 0.2 = -1.8$ kV. This persists until the capacitor discharges on the 500 kΩ resistor. By gating the circuit right after the UV beam has passed through the interaction region, allows us to go from a voltage region of low gain to one of high gain, only for the time that is of interest to us. The MCP was mount through a custom made bracket and was standing 4 cm on top of the interaction region, in the centre of the molecular chamber.

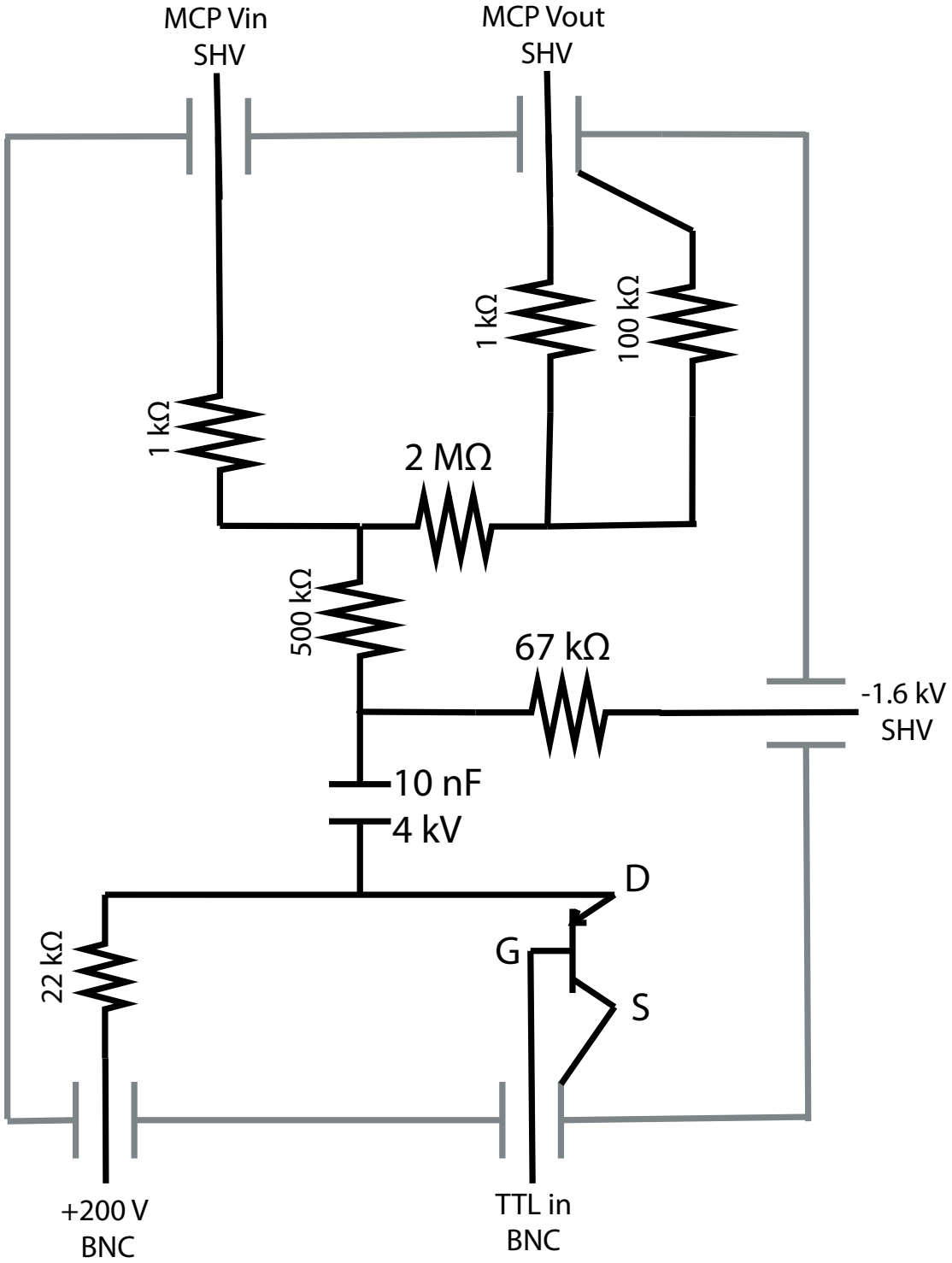

Figure 8.1: Schematic of the MCP gating circuit. In grey is shown the box housing the circuit, which was kept at the same ground as all the interconnected power supplies and the molecular chamber.

Appendix B: CARS efficiency considerations

Through the amplitude of the signal obtained on the photodiode, we can make a rough estimate of the efficiency of the CARS process. The responsivity $R(\lambda_{\mathrm{p}}$ of the photodiode as a function of the incident wavelength is defined as[2]

$$R(\lambda_{\mathrm{p}}) = \frac{I_{\mathrm{out}}}{P} = \frac{V_{\mathrm{out}}}{R_{\mathrm{load}} P} \tag{8.2}$$

where V_{out} is the output voltage, R_{load} is the resistance and P is the optical power incident on the photodiode. If we define P as

$$P = \frac{E_{\mathrm{photons}}}{t} = \frac{N_{\mathrm{ph}} h f}{t} = \frac{N h c}{\lambda t} \tag{8.3}$$

where N_{ph} is the number of photons incident on the photodiode, λ is their wavelength and t is the pulse duration, then equation 8.2 becomes

$$R(\lambda_{\mathrm{p}}) = \frac{V_{\mathrm{out}} \lambda t}{R_{\mathrm{load}} N_{\mathrm{ph}} h c} \Leftrightarrow N_{\mathrm{ph}} = \frac{V_{\mathrm{out}} \lambda t}{R_{\mathrm{load}} R(\lambda_{\mathrm{p}}) h c} \tag{8.4}$$

Solving equation 8.4 for a detectable signal of 1.2 V (since we are using an ND= 1 filter in front of the photodiode), $R(\lambda_{\mathrm{p}}) = 0.4$ A/W (from the photodiode's manufacturer), $R_{\mathrm{load}} = 50\ \Omega$ and $\lambda = 564.68$ nm, we find $N_{\mathrm{ph}} \approx 1.7 \times 10^9$ photons which should equate to roughly, without considering any losses in the detection, the number of molecules that have undergone the $X^1\Sigma_g^+$ v= 1, J= 1$\longleftarrow$ $X^1\Sigma_g^+$ v= 0, J= 1 transition. This result also assumes that *all* of the molecules in the $X^1\Sigma_g^+$ v= 1, J= 1 level absorbed a pump photon which excited them to a virtual level from which they decayed emitting a 564.68 nm photon.

Assuming that the interaction takes place only on the focus of the beam of radius $R = 100\ \mu$m, which equates to a volume of $V = 1.4 \times 10^{-9}\ l$, for a pressure of an atmosphere and at a temperature $T = 293$ K, we obtain through the ideal gas formula $PV = \frac{N_{\mathrm{m}}}{N_{\mathrm{A}}} RT$, where $R = 0.08206\ \mathrm{LatmK^{-1}mol^{-1}}$ is the gas constant and $N_{\mathrm{A}} = 6.022 \times 10^{23}$ is Avogadro's number, that the number of molecules within that volume is $N_{\mathrm{m}} \approx 1.05 \times 10^{14}$. Reminding that we are using a 90% Ne - 10% H_2 gas mixture, this means that within that volume the number of H_2 molecules is $N_{H_2} \approx 1.05 \times 10^{13}$, of which $\sim 2/3$ would be found initially in the $X^1\Sigma_g^+$ v= 0, J= 1 state. These considerations and assumptions then impose a lower

[2]Thorlabs DET36A Manual

bound for the efficiency of the CARS process, which would be $E =$

Bibliography

[1] Y. B. Band, *Light and Matter: Electromagnetism, Optics, Spectroscopy and Lasers* (John Wiley and Sons Ltd., London, 2006), first edn.

[2] J. Weiner, F. Nunes, *Light-Matter Interaction Physics and Engineering at the Nanoscale* (Oxford University Press, Oxford, 2012), first edn.

[3] T. H. Maiman, *Nature* **187**, 493 (1960).

[4] T. H. Maiman, *Phys. Rev. Lett.* **4**, 564 (1960).

[5] C. by A. D. McNaught, A. Wilkinson., *IUPAC. Compendium of Chemical Terminology (the "Gold Book")* (Blackwell Scientific Publications, Oxford, 1997), second edn.

[6] K. D. Bodin, V. V. Kresin, *Electric-Dipole Polarizabilities of Atoms, Molecules, and Clusters* (World Scientific Publishing Co., London, 1997), first edn.

[7] C. N. Cohen-Tannoudji, W. D. Phillips, *Physics Today* **43**, 33 (1990).

[8] S. Chu, L. Hollberg, J. E. Bjorkholm, A. Cable, A. Ashkin, *Phys. Rev. Lett.* **55**, 48 (1985).

[9] W. D. Phillips, H. J. Metcalf **256**, 36 (1987).

[10] A. Ashkin, *et al.*, *Applied Physics Letters* **9**, 72 (1966).

[11] R. Fulton, A. I. Bishop, M. N. Shneider, P. F. Barker, *Nat Phys* **2**, 465 (2006).

[12] P. F. Barker, M. N. Shneider, *Phys. Rev. A* **66**, 065402 (2002).

[13] C. J. Myatt, E. A. Burt, R. W. Ghrist, E. A. Cornell, C. E. Wieman, *Phys. Rev. Lett.* **78**, 586 (1997).

[14] F. Schreck, *et al.*, *Phys. Rev. A* **64**, 011402 (2001).

[15] G. Modugno, *et al.*, *Science* **294**, 1320 (2001).

[16] P. Barletta, J. Tennyson, P. F. Barker, *Phys. Rev. A* **78**, 052707 (2008).

[17] P. F. Barker, *et al.*, *Faraday Discuss.* **142**, 175 (2009).

[18] P. Barletta, J. Tennyson, P. F. Barker, *New Journal of Physics* **11**, 055029 (2009).

[19] K. M. Jones, E. Tiesinga, P. D. Lett, P. S. Julienne, *Rev. Mod. Phys.* **78**, 483 (2006).

[20] T. Köhler, K. Góral, P. S. Julienne, *Rev. Mod. Phys.* **78**, 1311 (2006).

[21] P. D. Lett, *et al.*, *Phys. Rev. Lett.* **71**, 2200 (1993).

[22] A. N. Nikolov, *et al.*, *Phys. Rev. Lett.* **84**, 246 (2000).

[23] J. M. Sage, S. Sainis, T. Bergeman, D. DeMille, *Phys. Rev. Lett.* **94**, 203001 (2005).

[24] J. G. Danzl, *et al.*, *Science* **321**, 1062 (2008).

[25] K.-K. Ni, *et al.*, *Science* **322**, 231 (2008).

[26] J. Deiglmayr, *et al.*, *Phys. Rev. Lett.* **101**, 133004 (2008).

[27] S. Jochim, *et al.*, *Science* **302**, 2101 (2003).

[28] E. Samuel, *Trans. Camb. Phil. Soc* **7**, 97 (1842).

[29] H. L. Bethlem, G. Berden, G. Meijer, *Phys. Rev. Lett.* **83**, 1558 (1999).

[30] H. L. Bethlem, F. M. H. Crompvoets, R. T. Jongma, S. Y. T. van de Meerakker, G. Meijer, *Phys. Rev. A* **65**, 053416 (2002).

[31] S. Y. T. van de Meerakker, P. H. M. Smeets, N. Vanhaecke, R. T. Jongma, G. Meijer, *Phys. Rev. Lett.* **94**, 023004 (2005).

[32] J. R. Bochinski, E. R. Hudson, H. J. Lewandowski, G. Meijer, J. Ye, *Phys. Rev. Lett.* **91**, 243001 (2003).

[33] E. R. Hudson, *et al.*, *Phys. Rev. A* **73**, 063404 (2006).

[34] S. Jung, E. Tiemann, C. Lisdat, *Phys. Rev. A* **74**, 040701 (2006).

[35] N. Vanhaecke, U. Meier, M. Andrist, B. H. Meier, F. Merkt, *Phys. Rev. A* **75**, 031402 (2007).

[36] E. Narevicius, *et al.*, *Phys. Rev. Lett.* **100**, 093003 (2008).

[37] E. Narevicius, *et al.*, *Phys. Rev. A* **77**, 051401 (2008).

[38] J. M. Doyle, B. Friedrich, J. Kim, D. Patterson, *Phys. Rev. A* **52**, R2515 (1995).

[39] J. D. Weinstein, R. deCarvalho, T. Guillet, B. Friedrich, J. M. Doyle, *Nature* **395**, 148 (1998).

[40] W. C. Campbell, E. Tsikata, H.-I. Lu, L. D. van Buuren, J. M. Doyle, *Phys. Rev. Lett.* **98**, 213001 (2007).

[41] W. Lu, Y. Zhao, P. F. Barker, *Phys. Rev. A* **76**, 013417 (2007).

[42] P. Maunz, *et al.*, *Nature* **428**, 50 (2004).

[43] H. W. Chan, A. T. Black, V. Vuletić, *Phys. Rev. Lett.* **90**, 063003 (2003).

[44] A. Trottier, D. Carty, E. Wrede, *Molecular Physics* **109**, 725 (2011).

[45] W. G. Doherty, *et al.*, *Phys. Chem. Chem. Phys.* **13**, 8441 (2011).

[46] E. S. Stockman, S. H. Zaidi, R. B. Miles, C. D. Carter, M. D. Ryan, *Combustion and Flame* **156**, 1453 (2009).

[47] H. T. Bookey, A. I. Bishop, P. F. Barker, *Opt. Express* **14**, 3461 (2006).

[48] M. N. Shneider, S. F. Gimelshein, *Applied Physics Letters* **102**, (2013).

[49] X. Pan, M. N. Shneider, R. B. Miles, *Phys. Rev. Lett.* **89**, 183001 (2002).

[50] B. M. Cornella, S. F. Gimelshein, M. N. Shneider, T. C. Lilly, A. D. Ketsdever, *Opt. Express* **20**, 12975 (2012).

[51] M. N. Shneider, P. Barker, *Optics Communications* **284**, 1238 (2011).

[52] A. S. Meijer, A. S. de Wijn, M. F. E. Peters, N. J. Dam, W. van de Water, *J. Chem. Phys.* **133**, 164315 (2010).

[53] D. Bruno, M. Capitelli, S. Longo, P. Minelli, *Chemical Physics Letters* **422**, 571 (2006).

[54] G. Dong, W. Lu, P. F. Barker, *Phys. Rev. E* **68**, 016607 (2003).

[55] A. A. Maznev, *et al.*, *Opt. Lett.* **36**, 2925 (2011).

[56] L. J. Shelton, F. Yang, W. K. Ford, H. J. Maris, *physica status solidi (b)* **242**, 1379 (2005).

[57] T. Pezeril, C. Klieber, S. Andrieu, K. A. Nelson, *Phys. Rev. Lett.* **102**, 107402 (2009).

[58] C. Thomsen, *et al.*, *Phys. Rev. Lett.* **53**, 989 (1984).

[59] C. Thomsen, H. T. Grahn, H. J. Maris, J. Tauc, *Phys. Rev. B* **34**, 4129 (1986).

[60] A. V. Scherbakov, *et al.*, *Opt. Express* **21**, 16473 (2013).

[61] C. Maher-McWilliams, *Ph.D. Thesis, University College London* (2012).

[62] N. P. Coppendale, *Ph.D. Thesis, University College London* (2011).

[63] T. Sean Kaoru, *Ph.D. Thesis, Imperial College London* (2009).

[64] J. M. Hutson, *Science* **327**, 788 (2010).

[65] R. V. Krems, *Phys. Chem. Chem. Phys.* **10**, 4079 (2008).

[66] S. Ospelkaus, *et al.*, *Science* **327**, 853 (2010).

[67] N. Balakrishnan, A. Alekseyev, R. Buenker, *Chemical Physics Letters* **341**, 594 (2001).

[68] J. J. Gilijamse, S. Hoekstra, S. Y. T. van de Meerakker, G. C. Groenenboom, G. Meijer, *Science* **313**, 1617 (2006).

[69] B. C. Sawyer, B. K. Stuhl, D. Wang, M. Yeo, J. Ye, *Phys. Rev. Lett.* **101**, 203203 (2008).

[70] A. von Zastrow, *et al.*, *Nat. Chem.* **6**, 216 (2013).

[71] B. Odom, D. Hanneke, B. D'Urso, G. Gabrielse, *Phys. Rev. Lett.* **97**, 030801 (2006).

[72] G. Gabrielse, D. Hanneke, T. Kinoshita, M. Nio, B. Odom, *Phys. Rev. Lett.* **97**, 030802 (2006).

[73] K. Szymaniec, W. Chalupczak, P. B. Whibberley, S. N. Lea, D. Henderson, *Metrologia* **42**, 49 (2005).

[74] J. van Veldhoven, *et al.*, *Eur. Phys. J. D* **31**, 337 (2004).

[75] M. R. Tarbutt, J. J. Hudson, B. E. Sauer, E. A. Hinds, *Faraday Discuss.* **142**, 37 (2009).

[76] B. C. Regan, E. D. Commins, C. J. Schmidt, D. DeMille, *Phys. Rev. Lett.* **88**, 071805 (2002).

[77] D. M. Kara, *et al.*, *New Journal of Physics* **14**, 103051 (2012).

[78] J. J. Hudson, *et al.*, *Nature* **473**, 493 (2011).

[79] T. A. Collaboration, *et al.*, *Science* **343**, 269 (2014).

[80] C. Maher-McWilliams, P. Douglas, P. F. Barker, *Nat Photon* **6**, 386 (2012).

[81] A. Gerakis, M. N. Shneider, P. F. Barker, *Opt. Express* **19**, 24046 (2011).

[82] A. Gerakis, M. N. Shneider, P. F. Barker, *Opt. Lett.* **38**, 4449 (2013).

[83] A. F. El-Sherif, K. Hussein, M. F. Hassan, M. M. Talat, *Proc. SPIE* **8235**, 82351P (2012).

[84] W. Koechner, *Solid state laser engineering* (Springer-Verlag, New York, 2006), sixth edn.

[85] K. S. Repasky, G. W. Switzer, J. L. Carlsten, *Review of Scientific Instruments* **73**, 3154 (2002).

[86] K. Mobarhan, *Newport Corporation* .

[87] R. A. Fields, M. Birnbaum, C. L. Fincher, *Applied Physics Letters* **51**, 1885 (1987).

[88] Y. Ma, *et al.*, *Opt. Express* **16**, 18702 (2008).

[89] T. Taira, A. Mukai, Y. Nozawa, T. Kobayashi, *Opt. Lett.* **16**, 1955 (1991).

[90] A. Sennaroglu, *Optics Communications* **164**, 191 (1999).

[91] P. L. Hansen, C. Pedersen, P. Buchhave, T. Skettrup, *Optics Communications* **127**, 353 (1996).

[92] N. Pavel, T. Taira, M. Furuhata, *Optics and Laser Technology* **30**, 275 (1998).

[93] A. Kemp, G. Friel, T. Lake, R. Conroy, B. Sinclair, *Quantum Electronics, IEEE Journal of* **36**, 228 (2000).

[94] J. Troger, L. Thévenaz, P. Robert, *Opt. Lett.* **24**, 1493 (1999).

[95] N. Coppendale, L. Wang, P. Douglas, P. Barker, *Applied Physics B: Lasers and Optics* **104**, 569 (2011).

[96] A. E. Siegman, *Lasers* (University Science Books, 1986).

[97] R. Fulton, *Ph.D. Thesis, Heriot-Watt University* (2006).

[98] E. Hecht, *Optics (4th Edition)* (Addison Wesley, 2001), fourth edn.

[99] M. S. Fee, K. Danzmann, S. Chu, *Phys. Rev. A* **45**, 4911 (1992).

[100] Leonardo, J. P. Richter, *The literary works of Leonardo Da Vinci. Compiled and edited from the original manuscripts by Jean Paul Richter* (Phaidon London], 1970), [3d ed. edn.

[101] A. T. Young, *Physics Today* **35**, 42 (1982).

[102] J. Tyndall, *Fragments of science: A Series of Detached Essays, Addresses and Reviews*, vol. 1 (London :Longmans, Green, and Co.,). Http://www.biodiversitylibrary.org/bibliography/18245.

[103] J. Strutt, *Third Baron Rayleigh, Phil. Mag.* **41**, 107 (1871).

[104] J. Strutt, *Third Baron Rayleigh, Phil. Mag.* **41**, 447 (1871).

[105] J. Strutt, *Third Baron Rayleigh, Phil. Mag.* **12**, 81 (1881).

[106] J. Strutt, *Third Baron Rayleigh, Phil. Mag.* **47**, 375 (1899).

[107] X. Pan, *Ph.D. Thesis, Princeton University* (2003).

[108] A. Einstein, *Annalen der Physik* **338**, 1275 (1910).

[109] M. v. Smoluchowski, *Annalen der Physik* **330**, 205 (1908).

[110] S. Kielich, *Acta Physica Polonica* **19**, 149 (1960).

[111] R. B. Miles, W. R. Lempert, J. N. Forkey, *Measurement Science and Technology* **12**, R33 (2001).

[112] L. Brillouin, *Annales de Physique (Paris)* **17** (1922).

[113] L. Mandelstam, *Zhurnal Russii Fizicheskoi Khimii Ova.* **58** (1926).

[114] W. Bragg **17**, 43 (1913).

[115] E. Gross, *Nature* **126**, 201 (1930).

[116] E. I. GORDON, *Appl. Opt.* **5**, 1629 (1966).

[117] A. Kersey, *et al.*, *Lightwave Technology, Journal of* **15**, 1442 (1997).

[118] L. Landau, G. Placzek, *Z. Phys. Sowjetunion* **5**, 172 (1934).

[119] R. W. Boyd, *Nonlinear Optics* (Elsevier, London, 2008), third edn.

[120] S. Yip, M. Nelkin, *Phys. Rev.* **135**, A1241 (1964).

[121] L. P. Kadanoff, P. C. Martin, *Annals of Physics* **24**, 419 (1963).

[122] M. Nelkin, S. Yip, *Physics of Fluids* **9**, 380 (1966).

[123] P. L. Bhatnagar, E. P. Gross, M. Krook, *Phys. Rev.* **94**, 511 (1954).

[124] T. J. Greytak, G. B. Benedek, *Phys. Rev. Lett.* **17**, 179 (1966).

[125] A. Sugawara, S. Yip, L. Sirovich, *Phys. Rev.* **168**, 121 (1968).

[126] A. Sugawara, S. Yip, L. Sirovich, *Physics of Fluids* **11**, 925 (1968).

[127] N. A. Clark, *Phys. Rev. A* **12**, 232 (1975).

[128] C. D. Boley, R. C. Desai, G. Tenti, *Canadian Journal of Physics* **50**, 2158 (1972).

[129] G. Tenti, C. D. Boley, R. C. Desai, *Canadian Journal of Physics* **52**, 285 (1974).

[130] U. G. E. Wang-Chang C. S., de Boer J., *Studies in Statistical Mechanics, edited by J. de Boer and G. E. Uhlenbeck* (North-Holland Publishing Co., Amsterdam), vol. ii, pp. 241268, part C. The heat conductivity and viscosity of polyatomic gases., year=1964 edn.

[131] E. E. Hagenlocker, W. G. Rado, *Applied Physics Letters* **7**, 236 (1965).

[132] D. H. Rank, T. A. Wiggins, R. V. Wick, D. P. Eastman, A. H. Guenther, *J. Opt. Soc. Am.* **56**, 174 (1966).

[133] R. P. Sandoval, R. L. Armstrong, *Phys. Rev. A* **13**, 752 (1976).

[134] Q. H. Lao, P. E. Schoen, B. Chu, *The Journal of Chemical Physics* **64**, 3547 (1976).

[135] P. Lilienfeld, *Opt. Photon. News* **15**, 32 (2004).

[136] I. N. Fabilinskii, *Molecular scattering of light* (Plenum, New York, 1968), first edn.

[137] R. Fulton, A. I. Bishop, M. N. Shneider, P. F. Barker, *Journal of Physics B: Atomic, Molecular and Optical Physics* **39**, S1097 (2006).

[138] P. B. Corkum, *et al.*, *Faraday Discuss.* **113**, 47 (1999).

[139] M. N. Shneider, P. Barker, *Optics Communications* **284**, 1238 (2011).

[140] M. R. Tarbutt, *et al.*, *Phys. Rev. Lett.* **92**, 173002 (2004).

[141] R. Fulton, A. I. Bishop, P. F. Barker, *Phys. Rev. A* **71**, 043404 (2005).

[142] M. N. Shneider, P. Barker, *Optics Communications* **284**, 1238 (2011).

[143] C. Y. She, G. C. Herring, H. Moosmüller, S. A. Lee, *Phys. Rev. Lett.* **51**, 1648 (1983).

[144] C. Y. She, G. C. Herring, H. Moosmüller, S. A. Lee, *Phys. Rev. A* **31**, 3733 (1985).

[145] J. H. Grinstead, P. F. Barker, *Phys. Rev. Lett.* **85**, 1222 (2000).

[146] X. Pan, M. N. Shneider, R. B. Miles, *Phys. Rev. A* **69**, 033814 (2004).

[147] M. N. Shneider, P. Barker, X. Pan, R. B. Miles, *Optics Communications* **239**, 205 (2004).

[148] X. Pan, M. N. Shneider, R. B. Miles, *Phys. Rev. A* **71**, 045801 (2005).

[149] W. M. Jr, *Journal of Statistical Mechanics: Theory and Experiment* **2007**, P03013 (2007).

[150] H. T. Bookey, M. N. Shneider, P. F. Barker, *Phys. Rev. Lett.* **99**, 133001 (2007).

[151] H. T. Bookey, A. I. Bishop, M. N. Shneider, P. F. Barker, *Journal of Raman Spectroscopy* **37**, 655 (2006).

[152] H. T. Bookey, A. I. Bishop, P. F. Barker, *Opt. Express* **14**, 3461 (2006).

[153] B. M. Cornella, S. F. Gimelshein, T. C. Lilly, A. D. Ketsdever, *Phys. Rev. A* **87**, 033825 (2013).

[154] M. Motsch, M. Zeppenfeld, P. W. H. Pinkse, G. Rempe, *New Journal of Physics* **12**, 063022 (2010).

[155] B. M. Cornella, S. F. Gimelshein, M. N. Shneider, T. C. Lilly, A. D. Ketsdever, *Opt. Express* **20**, 12975 (2012).

[156] M. O. Vieitez, *et al.*, *Phys. Rev. A* **82**, 043836 (2010).

[157] A. Manteghi, N. J. Dam, A. S. Meijer, A. S. de Wijn, W. van de Water, *Phys. Rev. Lett.* **107**, 173903 (2011).

[158] A. S. Meijer, A. S. de Wijn, M. F. E. Peters, N. J. Dam, W. van de Water, *The Journal of Chemical Physics* **133**, (2010).

[159] C. Rossignol, *et al.*, *Applied Physics Letters* **93**, (2008).

[160] M. Ducousso, *et al.*, *The European Physical Journal Applied Physics* **61** (2013).

[161] M. Fujita, O. Kotyaev, Y. Shimada, *Conference on Lasers and Electro-Optics 2012* (Optical Society of America, 2012), p. ATu2G.3.

[162] M. N. Shneider, S. F. Gimelshein, *Applied Physics Letters* **102**, (2013).

[163] E. B. Cummings, *Opt. Lett.* **19**, 1361 (1994).

[164] E. B. Cummings, I. A. Leyva, H. G. Hornung, *Appl. Opt.* **34**, 3290 (1995).

[165] R. C. Hart, R. J. Balla, G. C. Herring, *Appl. Opt.* **38**, 577 (1999).

[166] S. Schlamp, E. B. Cummings, T. H. Sobota, *Opt. Lett.* **25**, 224 (2000).

[167] R. C. Hart, G. C. Herring, R. J. Balla, *Opt. Lett.* **32**, 1689 (2007).

[168] W. Hubschmid, B. Hemmerling, A. Stampanoni-Panariello, *J. Opt. Soc. Am. B* **12**, 1850 (1995).

[169] A. Stampanoni-Panariello, B. Hemmerling, W. Hubschmid, *Phys. Rev. A* **51**, 655 (1995).

[170] A. Stampanoni-Panariello, D. Kozlov, P. Radi, B. Hemmerling, *Applied Physics B* **81**, 101 (2005).

[171] A. Stampanoni-Panariello, D. Kozlov, P. Radi, B. Hemmerling, *Applied Physics B* **81**, 113 (2005).

[172] A. Stampanoni-Panariello, B. Hemmerling, W. Hubschmid, *Applied Physics B* **67**, 125 (1998).

[173] B. Hemmerling, D. N. Kozlov, A. Stampanoni-Panariello, *Opt. Lett.* **25**, 1340 (2000).

[174] A. B. Gojani, P. M. Danehy, D. W. Alderfer, T. Saito, K. Takayama, *Proc. SPIE* **5251**, 313 (2004).

[175] E. B. Cummings, *Opt. Lett.* **19**, 1361 (1994).

[176] D. C. Auth, *Applied Physics Letters* **16**, 521 (1970).

[177] J. D. J. Anderson, *Computational Fluid Mechanics* (McGraw-Hill, New York, 1995).

[178] M. N. Shneider, P. Barker, *Opt. Comms.* **284**, 1238 (2011).

[179] F. E. Faber, *Fluid dynamics for physicists* (Cambridge University Press, Cambridge, 1995), fourth edn.

[180] A. Gerakis, M. N. Shneider, P. F. Barker, *Opt. Express* **19**, 24046 (2011).

[181] A. Manteghi, N. J. Dam, A. S. Meijer, A. S. de Wijn, W. van de Water, *Phys. Rev. Lett.* **107**, 173903 (2011).

[182] B. M. Cornella, S. F. Gimelshein, M. N. Shneider, T. C. Lilly, A. D. Ketsdever, *Opt. Express* **20**, 12975 (2012).

[183] P. F. Barker, *et al.*, *Faraday Discuss.* **142**, 175 (2009).

[184] P. Barletta, J. Tennyson, P. F. Barker, *Phys. Rev. A* **78**, 052707 (2008).

[185] A. I. Bishop, L. Wang, P. F. Barker, *New Journal of Physics* **12**, 073028 (2010).

[186] P. F. Barker, M. N. Shneider, *Phys. Rev. A* **64**, 033408 (2001).

[187] P. F. Barker, M. N. Shneider, *Phys. Rev. A* **66**, 065402 (2002).

[188] R. L. Farrow, D. W. Chandler, *The Journal of Chemical Physics* **89** (1988).

[189] S. Cureton-Chinn, P. B. Kelly, M. P. Augustine, *The Journal of Chemical Physics* **116** (2002).

[190] N. C. M. Bartlett, *et al.*, *The Journal of Chemical Physics* **129**, (2008).

[191] C.-S. Wang, *Phys. Rev.* **182**, 482 (1969).

[192] M. Maier, *Applied physics* **11**, 209 (1976).

[193] M. A. Linne, *Spectroscopic measurement: an introduction to the fundamentals* (Academic Press, 2002).

[194] B. Mate, F. Thibault, G. Tejeda, J. M. Fernández, S. Montero, *The Journal of Chemical Physics* **122**, (2005).

[195] G. Pozgainer, L. Windholz, A. Winkler, *Measurement Science and Technology* **5**, 947 (1994).

[196] M. N. R. Ashfold, J. D. Howe, *Annual Review of Physical Chemistry* **45**, 57 (1994).

[197] P. M. Johnson, M. R. Berman, D. Zakheim, *The Journal of Chemical Physics* **62** (1975).

[198] G. Petty, C. Tai, F. W. Dalby, *Phys. Rev. Lett.* **34**, 1207 (1975).

[199] J. W. Hudgens, *PROGRESS IN RESONANCE ENHANCED MULTIPHOTON IONIZATION SPECTROSCOPY of TRANSIENT FREE RADICALS*, chap. 3, pp. 171–296.

[200] J. S. A. Perry, *et al.*, *Measurement Science and Technology* **13**, 1414 (2002).

[201] H. Mori, C. Dankert, *Rarefied Gas Dynamics*, A. D. Ketsdever, E. P. Muntz, eds. (2003), vol. 663 of *American Institute of Physics Conference Series*, pp. 170–177.

[202] G. E. Schmauch, A. H. Singleton, *Industrial & Engineering Chemistry* **56**, 20 (1964).

[203] G. Buntkowsky, *et al.*, *Phys. Chem. Chem. Phys.* **8**, 1929 (2006).

[204] D. M. Mosbacher, *Ph.D. Thesis, Vanderbilt University* (2004).

[205] D. Staack, B. Farouk, A. Gutsol, A. Fridman, *Plasma Sources Science and Technology* **14**, 700 (2005).

[206] R. Sigmond, *Le Journal de Physique IV* **7**, C4 (1997).

[207] S. Nae Cho, *Physics of Plasmas (1994-present)* **19**, (2012).

[208] M. Gostein, G. O. Sitz, *Review of Scientific Instruments* **66** (1995).